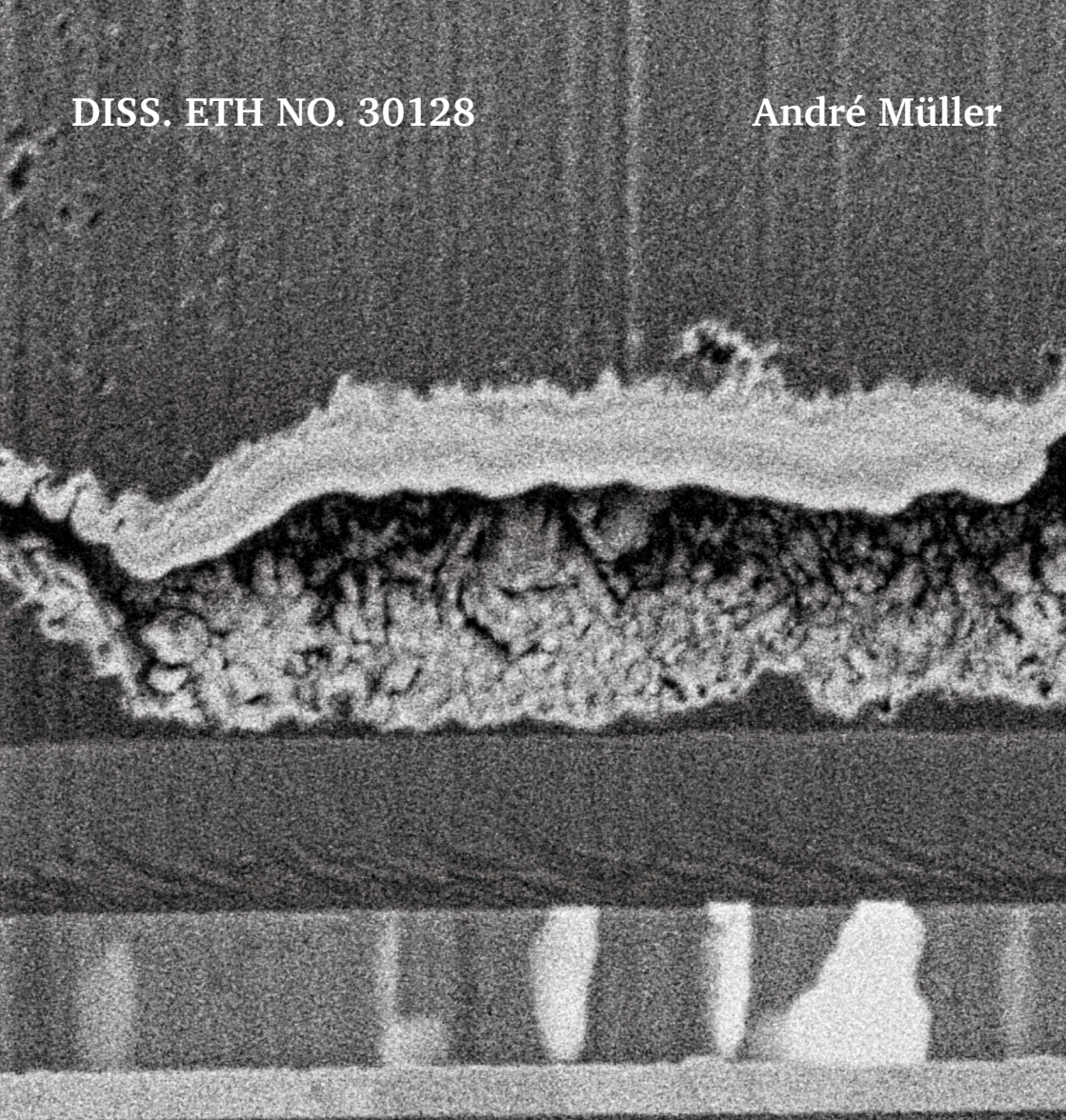DISS. ETH NO. 30128

André Müller

Enhancing Interfacial Stability in Oxide Solid-State Batteries:

Diffusion Barriers and Seed Layers

Enhancing Interfacial Stability

in Oxide Solid-State Batteries:

Diffusion Barriers and Seed Layers

A thesis submitted to attain the degree of

DOCTOR OF SCIENCES

(Dr. sc. ETH Zürich)

Presented by

André Müller

M.Sc. in Mechanical Engineering,

Technische Universität Carolo-Wilhelmina zu Braunschweig

Born on 09.05.1996

Accepted on the recommendation of

Prof. Dr. Maksym V. Kovalenko, examiner

Prof. Dr. Corsin Battaglia, co-examiner

Dr. Martin Finsterbusch, co-examiner

Dr. Yaroslav E. Romanyuk, co-examiner

2024

"Try not to become a man of success, but rather try to become a man of value."

– *Albert Einstein*

iv

CONTENTS

viii

LIST OF TABLES

x

LIST OF FIGURES

ABSTRACT

Solid-state batteries (SSBs) are a crucial area of research in the quest for safe and efficient energy storage systems. These batteries, which use solid electrolytes instead of liquid electrolytes, offer improvements in safety and energy density over traditional lithium-ion batteries due to the potential use of metallic lithium anodes. However, the stability of solid electrolyte/electrode interfaces in SSBs is a substantial challenge that affects their performance and lifetime. This Thesis addresses this challenge by investigating lithiated metal oxide interlayers and seed layers in oxide SSBs to enhance interfacial stability.

For the cathode|solid-state electrolyte interface, high-energy $LiCoO_2$ cathodes are fabricated with $Li_7La_3Zr_2O_{12}$ (LLZO) solid-electrolytes by co-sintering at high temperatures using lithiated metal oxide interlayers (Li-Me-O where Me = Al, Nb, or Ti) deposited by sputtering techniques. These interlayers are effective in reducing Co/La cation mixing at the cathode-electrolyte interface. It is shown that the introduction of interlayers results in more defined interfaces compared to unmodified battery stacks. Using electrochemical impedance spectroscopy, the Li-Nb-O interlayer was shown

to reduce the interfacial impedance from 8 kΩ cm^2 to 1 kΩ cm^2. Finally, the Li-Nb-O interlayer proved to be the most efficient, with a discharge capacity of 125 mAh g^{-1}. The phenomenon of asymmetric voltage drop during discharge and the charge-discharge transition is observed in these batteries. A sharp impedance drop was observed during this transition. This voltage drop phenomenon has been discussed and contextualized in the battery research community, but it is not yet fully understood. The most plausible hypothesis seems to revolve around delamination at the cathode|SSE interface.

For the anode|solid-state electrolyte interface, the influence of seed layers (gold, platinum, and amorphous carbon) in anode-free configurations is investigated. Thin film stacks have been fabricated by PVD techniques in the following architecture: Cu/seed layer/LiPON/Li/Cu. Lithium deposition at the interface between the copper current collector and the LiPON electrolyte was investigated. It was found that the bare current collector in a thin-film anode-free architecture without a seed layer is prone to cracking. The integration of seed layers suppressed current collector cracking and resulted in a more homogeneous lithium layer. The amorphous carbon maintained its integrity during cycling and significantly influenced the lithium plating and stripping dynamics. The amorphous carbon seed layer reduced the plating potential from 300 mV for a bare copper current collector to less than 100 mV at a current density of 8 mA cm^{-2}. Moreover, an optical microscopy setup was developed to visualize Li nucleation between the solid electrolyte and the current collector during operation. It is shown that a thin carbon seed layer on non-ideal surfaces such as LLZO improves the homogeneous plating of lithium and thus increases the plating capacity by up to 0.1mAh cm^{-2}.

The results of this work contribute to the understanding of interfacial phenomena in solid-state batteries and provide practical approaches to improve their performance and durability. Of particular note is the effectiveness of Li-Nb-O interlayers in mitigating cation diffusion and the potential of carbon seed layers in reducing overpotential during lithium plating and stripping.

KURZFASSUNG

Festkörperbatterien (engl. solid-state batteries, SSB) sind ein zentrales Forschungsgebiet auf der Suche nach sicheren und effizienten Energiespeichersystemen. Diese Batterien, die feste statt flüssige Elektrolyte verwenden, bieten durch den möglichen Einsatz von metallischen Lithiumanoden Verbesserungen hinsichtlich Sicherheit und Energiedichte gegenüber herkömmlichen Lithium-Ionen-Batterien. Allerdings stellt die Stabilität der Festelektrolyt/Elektroden-Grenzfläche in SSBs eine große Herausforderung dar, die sich auf ihre Leistung und Lebensdauer auswirkt. Diese Arbeit befasst sich mit dieser Herausforderung, indem lithiumhaltige Metalloxid-Zwischenschichten und Keimschichten (engl. seed layer) in oxidischen SSBs untersucht werden, um die Grenzflächenstabilität zu verbessern.

Für die Kathode-Festkörperelektrolyt-Grenzfläche werden hochenergetische $LiCoO_2$-Kathoden mit $Li_7La_3Zr_2O_{12}$-Festkörperelektrolyten (LLZO) durch Co-Sintern bei hohen Temperaturen unter Verwendung lithiumhaltiger Metalloxid-Zwischenschichten (Li-Me-O, wobei Me = Al, Nb oder Ti) hergestellt, die durch Sputtertechniken abgeschieden werden. Diese Zwischenschichten verringern wirksam die Vermischung von Co/La-Kationen an der Kathoden-

Elektrolyt-Grenzfläche. Es wird gezeigt, dass die Einführung von Zwischenschichten im Vergleich zu unmodifizierten Batterie-Stacks zu besser definierten Grenzflächen führt. Mit Hilfe der elektrochemischen Impedanzspektroskopie konnte gezeigt werden, dass die Li-Nb-O-Zwischenschicht die Grenzflächenimpedanz von 8 kΩ cm^2 auf 1 kΩ cm^2 reduziert. Schließlich erwies sich die Li-Nb-O-Zwischenschicht mit einer Entladekapazität von 125 mAh g^{-1} als die leistungsfähigste. Bei diesen Batterien wurde das Phänomen des asymmetrischen Spannungsabfalls während der Entladung und des Lade-Entlade-Übergangs beobachtet. Während dieses Übergangs wurde ein starker Impedanzabfall beobachtet. Dieses Phänomen des Spannungsabfalls wurde in der Batterie-Fachwelt diskutiert und in Zusammenhang gebracht, ist aber noch nicht vollständig verstanden. Die plausibelste Hypothese dreht sich um Delaminationen an der Kathoden-SSE-Grenzfläche.

Für die Anoden-Festkörperelektrolyt-Grenzfläche wird der Einfluss von Keimschichten (Gold, Platin und amorpher Kohlenstoff) in anodenfreien Konfigurationen untersucht. Dünnschicht-Stacks werden mittels PVD-Techniken in der folgenden Architektur hergestellt: Cu/Keimschicht/LiPON/Li/Cu. Die Lithiumabscheidung an der Grenzfläche zwischen dem Kupferstromkollektor und dem LiPON-Elektrolyten wurde untersucht. Es wurde festgestellt, dass der unbeschichtete Stromkollektor in einer anodenfreien Dünnschichtarchitektur ohne Keimschicht anfällig für Brüche ist. Die Integration von Keimschichten unterdrückte die Rissbildung im Stromkollektor und führte zu einer homogeneren Lithiumschicht. Der amorphe Kohlenstoff behielt seine Integrität während der Zyklen und beeinflusste die Dynamik der Lithiumabscheidung und des Strippings. Die amorphe Kohlenstoffkeimschicht

reduzierte das Abscheidungspotenzial von 300 mV für einen blanken Kupferstromabnehmer auf weniger als 100 mV bei einer Stromdichte von 8 mA cm^{-2}. Zusätzlich wurde ein optisches Mikroskop entwickelt, um die Li-Nukleation zwischen dem Festelektrolyten und dem Stromkollektor während des Betriebs zu visualisieren. Es konnte gezeigt werden, dass eine dünne Kohlenstoff-Keimschicht auf nicht-idealen Oberflächen wie LLZO die homogene Lithiumabscheidung verbessert und somit die Abscheidekapazität um bis zu 0.1 mAh cm^{-2} erhöht.

Die Ergebnisse dieser Arbeit tragen zum Verständnis von Grenzflächenphänomenen in Festkörperbatterien bei und bieten praktische Ansätze zur Verbesserung ihrer Leistungsfähigkeit und Lebensdauer. Besonders hervorzuheben ist die Wirksamkeit von Li-Nb-O Zwischenschichten zur Abschwächung der Kationendiffusion und das Potential von Kohlenstoff-Keimschichten zur Reduzierung von Überspannungen während der Lithiumbeschichtung und des Strippings.

1 INTRODUCTION AND OBJECTIVES

Addressing the Dual Challenge of the global energy crisis and climate change is one of the crucial challenges for humanity in the 21st century [1]. Fossil fuels, particularly coal, natural gas, and oil have been central to global economic growth since the Industrial Revolution. However, their widespread use has led to significant environmental challenges, with global warming being the most pressing [2]. The global average temperature in 2022 is almost 1°C higher than in the middle of the 20th century (see Figure 1.1a). Moreover, as the world's population grows, the demand for energy is expected to outstrip the availability of fossil fuels [3]. Addressing this emerging energy gap and mitigating climate change are major challenges for today's society. These goals require the development of sustainable energy technologies and a collective effort to reduce greenhouse gas emissions.

Figure 1.1b shows the trajectory and future projections of global electricity generation for various energy sources through 2050 [7]. While the overall demand for electricity increases, the share of sustainable energy sources is projected to increase substantially, accounting for about 55 % of the electricity mix by 2050. This upward trend in renewable energy underscores the
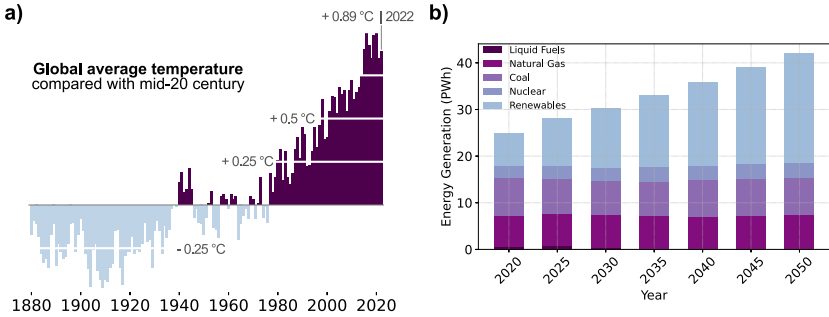
Figure 1.1. Climate change and global electricity generation. (a) Global average temperature compared with the mid-20th century, and (b) projected global electricity generation in 2020 with forecast to 2050, by energy source. Adapted from The Learning Network [4–7].

collective effort to solve the energy crisis. However, an emerging challenge is how to effectively store this rapidly growing share of renewable energy, especially given the intermittent and unpredictable nature of its generation [8].

Lithium-ion batteries will play a central role in bridging this gap and storing energy. Recognized with the 2019 Nobel Prize in Chemistry, these batteries have a notable history that began with the introduction of the first cell in 1962 and led to Sony's groundbreaking rechargeable model in 1991 [9, 10]. Due to their superior voltage, energy density, and flexibility, lithium-ion batteries have outperformed traditional batteries such as lead-acid or Ni-Cd. In this context, rechargeable battery technologies are emerging as a key enabler in addressing the energy storage challenges associated with the intermittent and stochastic nature of renewable energy sources [11]. Moreover, they will play a critical role in addressing the world's future energy

challenges, particularly in reducing dependence on fossil fuels in areas such as transportation. Electric vehicles powered by these batteries are expected to be market leaders by 2040 (see Figure 1.2).
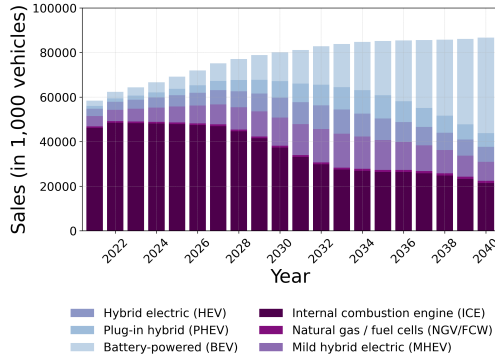
Figure 1.2. Forcast global passenger car sales by powertrain from 2021 to 2040. Adapted from ABB Group [12].

As technology evolves, the differences between lithium-ion and lithium-metal batteries and between liquid and solid-state batteries are becoming more apparent, affecting their use and potential. Among the various battery chemistries, lithium batteries have gained acceptance due to their superior energy density and minimal toxicity [13]. Despite remarkable advances in lithium battery technology over the past five decades, today's lithium-ion batteries remain limited in their energy density and safety profile [14]. The complex nature of battery systems, especially with the push to utilize lithium metal anodes and integrate safer solid-state electrolytes, underscores the need for continued scientific research, especially with respect to the puzzling interfacial phenomena [15].

1.1   Lithium-ion battery

Rechargeable batteries have evolved continuously since their introduction in 1859, from lead-acid batteries to the more advanced lithium-ion batteries. In particular, the 1970s and 1980s saw groundbreaking advances in lithium-ion technology. Dr. Whittingham of Exxon Mobil began this development in the late 1970s by exploring a rechargeable battery concept using titanium disulfide and lithium metal electrodes [16]. In the following decade, Professor Goodenough introduced a lithium cobalt oxide ($LiCoO_2$) cathode [17], while Professor Yazami demonstrated the potential of a graphite anode to electrochemically incorporate lithium [18]. Based on these fundamental findings, Professor Yoshino developed the first prototype lithium-ion battery. By the early 1990s, Sony had refined this technology to market readiness and in 1991 introduced the first commercially viable lithium-ion battery that combined a coke (amorphous carbon) anode with a layered $LiCoO_2$ cathode. Since then, both gravimetric and volumetric energy densities have steadily increased, nearly doubling to 240 Wh kg^{-1} and 700 Wh l^{-1}, respectively, indicating a trend toward the theoretical performance limits of conventional liquid lithium-ion batteries (Figure 1.3). At the same time, the cost of battery packs has dropped by more than 80 % in the last decade, from 780 USD kWh^{-1} to just 139 USD kWh^{-1} [19].
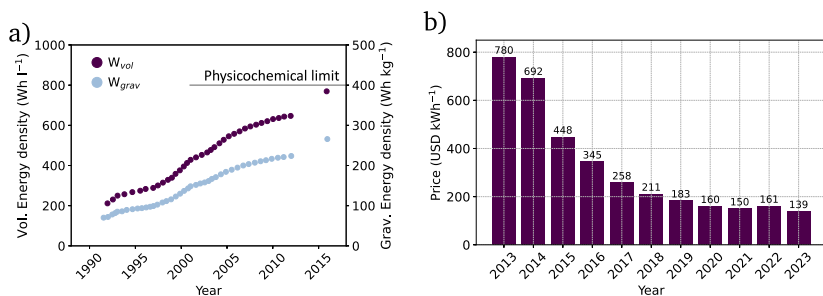
Figure 1.3. Development of energy densities and prices of lithium-ion batteries. a) Gravimetric and volumetric energy densities of lithium-ion batteries from 1990 until 2015. Adapted from Janek & Zeier [20]. b) Lithium-ion battery prices worldwide from 2013 to 2023 (in U.S. dollars per kilowatt-hour). Adapted from BloombergNEF [19].

Working principle

Lithium-ion secondary batteries consist primarily of an electrochemical cell that converts chemical energy into electrical energy when discharged. The main components of this cell are a negative electrode (anode) and a positive electrode (cathode), an electrolyte that facilitates the movement of Li^+-ions between the electrodes and electronically insulates the electrodes, and current collectors, as shown in Figure 1.4. Each electrode consists of an active material, such as $LiCoO_2$ for the cathode or graphite for the anode, in which Li^+-ions are stored. Different redox potentials indicate their different tendencies to accept or release electrons. These materials undergo redox reactions and generate an electromotive force. When the cell is in an open circuit, the voltage generated can be determined by the difference in chemical potential between the anode and cathode:

$$OCV = (\mu_A - \mu_C)/F \tag{1.1}$$
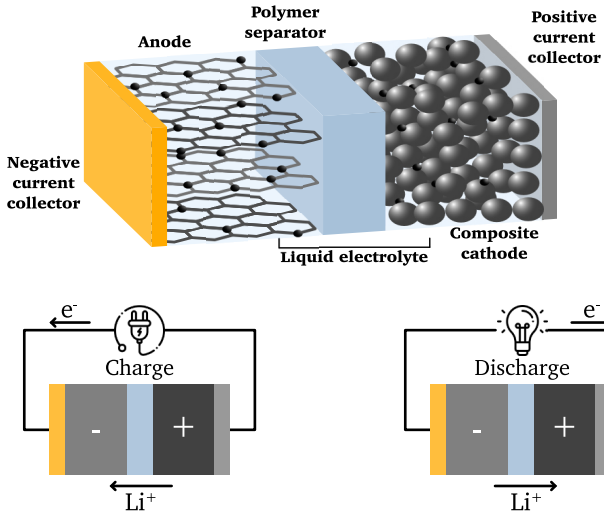
Figure 1.4. Schematic representation of the components of a Li-ion battery and the movement (of electrons and Li$^+$ ions) during charging and discharging.

During the charging phase of a Li-ion battery, an external electrical potential is applied to the cathode and anode. This causes the migration of electrons from the cathode to the anode through the external circuit, resulting in oxidation of the cathode and reduction of the anode. This electron flow is counterbalanced by the simultaneous movement of Li$^+$ ions within the cathode, which migrate through the electrolyte in the opposite direction of the electrons to be intercalated into the anode. During discharging, the redox reactions occur spontaneously and the process described is reversed.

Active materials in batteries

Each component of a battery plays an important role in ensuring optimal performance and durability. In a Li-ion battery, the electrodes - cathode and anode - are particularly important as they are the active materials in the battery. They determine both the battery's operating voltage and its maximum capacity, and advances over the years have led to improvements in these parameters. Cathodes, which typically operate on the basis of an intercalation mechanism, are generally divided into three primary classes based on their crystalline structure:

1. Layered structures

2. Olivine structures

3. Spinel Materials

These categories include a number of cathode materials that have been developed and commercialized over time. The most famous structure is the layered oxide $LiCoO_2$ mentioned earlier (see Figure 1.5). It was used in the first commercial Li-ion batteries by Sony in 1991. Since then, it has become one of the dominant cathode materials due to its specific capacity of about 140 mAh g^{-1} (at a cutoff potential of 4.2 V vs. Li/Li$^+$), long cycle life, and ease of preparation [21]. Similar to other $LiMO_2$-type cathodes (M = V, Cr, Co, Ni), LCO has a layered structure in which Li$^+$ and Co^{3+} ions occupy the octahedral interstitials of the cubic close-packed (ccp) oxygen framework in alternating planes [22]. The structure, characterized by covalently bonded CoO_2 layers, allows reversible insertion and extraction into

the layers. In addition, the movement of lithium ions between these layers allows for efficient two-dimensional lithium diffusion. In theory, all of the Li in $LiCoO_2$ can be removed electrochemically. However, reversible extraction is only possible between $LiCoO_2$ and $Li_{0.5}CoO_2$, a property shared with other lithium transition metal oxides [21]. In addition, Li_xCoO_2 was shown to exhibit high electronic conductivity, transitioning from semiconducting at x = 1 to metallic at lower lithium concentrations, which aids in lithium-ion deintercalation/intercalation and fast charge capabilities [23].
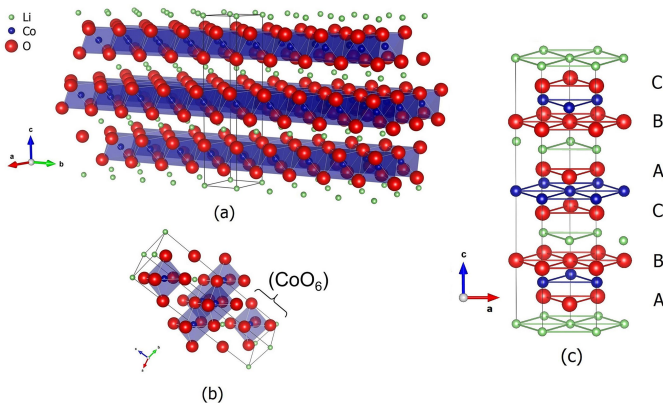
Figure 1.5. a) Layered crystalline structure of the rhombohedral $LiCoO_2$, b) Representation of the octahedral CoO_6 structure, and c) stacking arrangement of the layers (ABCABC). [24]

To further improve the energy density and reduce the cost of Li-ion batteries, researchers have introduced alternative layered cathode materials. Among them, $LiNi_xMn_yCo_zO_2$ (NMC class) has not only been developed but also integrated into commercial applications with capacities exceeding 250 mAh g^{-1} [25]. The olivine structure, represented by $LiFePO_4$ (LFP), has

CHAPTER 1

gained acceptance in battery research and industry. This is due to its consistent voltage profile at 3.2 V vs. Li/Li$^+$, affordability, wide availability of raw materials, inherent stability, theoretical capacity of 170 mAh g^{-1}, and safety characteristics [26]. The category of spinel oxides includes materials such as LiMn$_2$O$_4$ (LMO) and LiMn$_{0.5}$Ni$_{0.5}$O$_4$ (LMNO). These spinel compounds are known for their remarkable properties, such as high potentials of up to 5 V, good cycle life, high energy density, and high rate capability [27].

While the composition of intercalation cathodes is continuously being tuned to improve their rate capability and cycle life, the specific capacities of such intercalation compounds are approaching their theoretical values, thus limiting the energy densities and specific energies of practical cells [28]. On the other hand, conversion-type cathode materials are considered to be some of the key candidates for the next generation of rechargeable lithium-ion batteries. Instead of simply intercalating lithium ions, they engage in redox reactions that break and create new chemical bonds during the processes of lithiation and delithiation [29].

To highlight the potential of conversion cathodes, sulfur stands out. When lithiated, sulfur is converted to Li$_2$S. These conversion cathodes can achieve impressive capacities, with a theoretical capacity of 1670 mAh g^{-1} [29]. However, conversion cathodes are not without their drawbacks. Their insulating nature during delithiation can reduce rate performance and limit capacity. In addition, the interaction of sulfur with the electrolyte can produce polysulfide ions, which can lead to capacity degradation [30]. Other conversion cathodes that are being investigated include iron fluoride (FeF$_3$) and copper fluoride (CuF$_2$). Their theoretical energy densities are equal to

or greater than sulfur. However, they have a set set of challenges, such as poor conductivity and limited cycle life [29].

For anode materials, graphite and hard carbon are the predominant options in the field, primarily due to their favorable properties, such as low working potential at approx. 0.1 V vs. Li/Li$^+$, affordability, and good cycle life [31]. However, graphite's specific capacity is limited to 372 mAh g^{-1} [32], and it is prone to Li plating during rapid charging. This has led researchers to explore alternative anode materials. Intercalation oxides, such as $Li_4Ti_5O_{12}$ (LTO), have attracted interest for high-power applications [33]. At the same time, alloyed materials such as silicon have gained attention because of their low cost, exceptional gravimetric and volumetric capacity (3590 mAh g^{-1} and 8365 mAh cm^{-3} for silicon), and abundance. Despite silicon's impressive capacity, which is ten times that of graphite, its sizeable volumetric expansion (approx. 300 %) that occurs during lithiation/delithiation is a challenge that limits its lifetime [34, 35]. As a result, only C/Si composite anodes have gained commercial acceptance.

To overcome these challenges, there has been a revival of interest in pure lithium metal as the negative electrode. Lithium metal was already subject to intensive research in the 1960s–1970s as it has an impressive theoretical capacity of 3860 mAh g^{-1}, a low redox potential (-3.04 V vs. SHE), and a light density (0.534 g cm^{-3}) [36]. Lithium metal is fundamental to the solid-state battery concept and is considered the best anode material. The integration of a solid-state electrolyte stands out as a key strategy to improve safety, limit side reactions, and eliminate the flammability risk posed by organic solvents [37]. An added benefit is the possible in-situ formation of

the Li metal anode using the lithium present in a lithiated cathode, which can streamline manufacturing and provide cost savings [38].

Figure 1.6 provides an overview of the cathode and anode materials discussed, illustrating an aggregated view of the average discharge potentials and specific capacities across all electrode categories, providing a clear perspective on the performance metrics of the different materials.
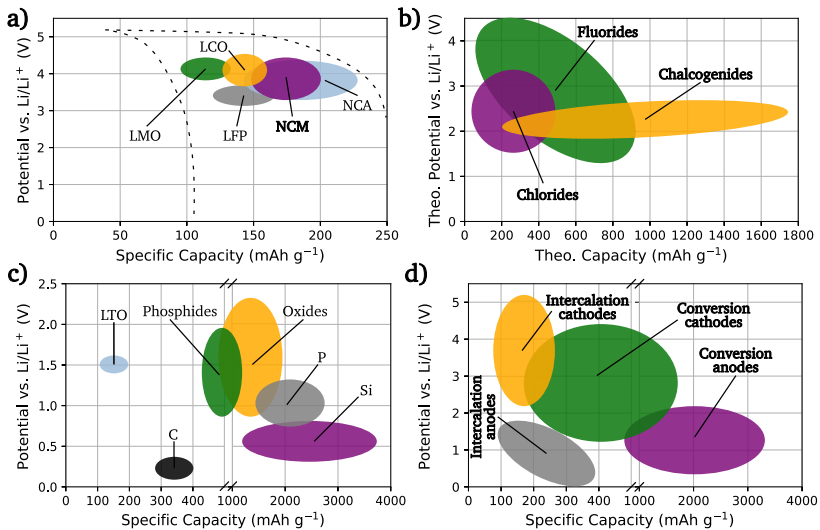
Figure 1.6. Comparative overview of average discharge potentials and specific capacities for various electrode types. (a) Intercalation-type cathodes (experimental), (b) Conversion-type cathodes (theoretical), (c) Conversion-type anodes (experimental), and (d) Aggregated average discharge potentials and specific capacities across all electrode categories. Adapted from Nitta et al. [31]

In terms of broader battery technology advancements, several key performance metrics and challenges remain: (i) achieving high energy density, (ii) enabling fast charging capabilities, (iii) implementing a solid-state electrolyte,

and (iv) accelerating battery development from a cost perspective. Each of these aspects is closely related to the design complexities and chemical compositions of the electrode materials.

1.2 All-solid-state battery

The potential for further optimization of liquid electrolyte-based lithium-ion batteries is shrinking and is expected to reach its theoretical performance limits [20, 39]. Therefore, it is necessary to explore alternative, more advanced battery designs. A new generation of solid-state batteries is being developed and could become commercially available in the next few years. Figure 1.7 shows the schematic structure of an all-solid-state lithium-ion battery. They follow the general electrochemical structure of a traditional lithium-ion battery, as described earlier. The difference is the (at least partial) replacement of the liquid ion-conducting electrolyte with a solid electrolyte.

An important measure of battery performance is energy density, which can be evaluated gravimetrically (in terms of mass) or volumetrically (in terms of volume). For electric vehicles, increasing the energy storage capacity of the battery and, thus, the range is an important goal. The introduction of a solid-state electrolyte can increase the energy density by 70 % volumetrically and 40 % gravimetrically [20]. This is mainly due to the introduction of lithium metal anodes with their superior energy density and is, therefore, a key part of the strategy, especially in terms of safety.

Safety has always been paramount in battery technology. Solid-state batteries inherently offer an improved safety profile. The transition from
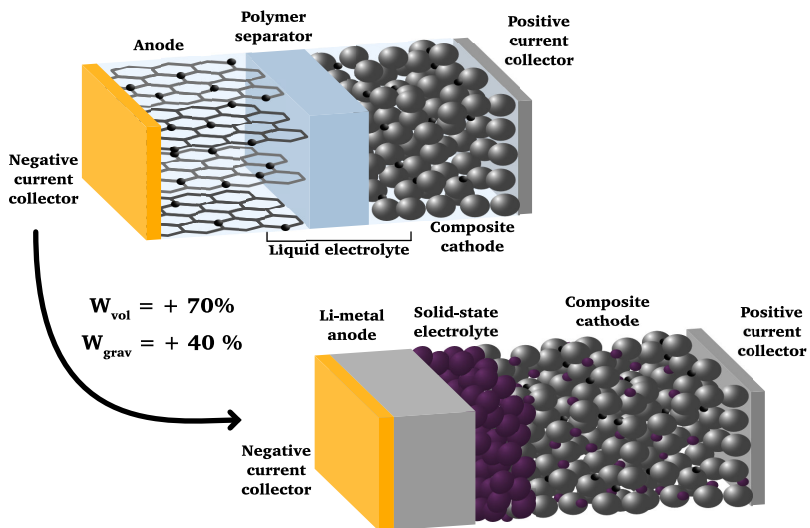
Figure 1.7. Schematic of the architecture of a conventional lithium-ion battery and a lithium-metal solid-state battery.

a flammable liquid electrolyte to a non-flammable solid variant not only reduces the risk of leakage and, thus, contamination and environmental hazards but also significantly reduces the likelihood of short circuits. This safety improvement is further enhanced by the fact that solid-state batteries completely eliminate the potentially hazardous liquid electrolyte [40]. Some early solid-state battery designs are pursuing the idea of retaining minimal amounts of liquid electrolyte, particularly at the interface between the electrolyte and the active materials [41]. Yet these hybrid designs should be viewed more as a transition to true all-solid-state batteries. However, the transition to solid-state batteries comes with its own challenges. Choosing the right solid-state electrolyte material plays an important role in selecting

the perfect solid-state setup.

Solid-electrolytes

A key innovation in solid-state batteries is the solid electrolyte, which is responsible for transporting lithium ions between electrodes while acting as an insulator against electronic charges. The key properties of a solid electrolyte can be grouped into three categories (i) electrochemical and ion transport properties, (ii) material and mechanical characteristics, and (iii) manufacturing and economic aspects [42].

Electrochemical and ion transport properties The ion transport characteristics of a solid electrolyte are critical. As a rule, it must allow rapid ion movement with an ionic conductivity close to or better than liquid electrolytes, about 10^{-3} to 10^{-2} S cm^{-1} at room temperature [43]. A wide electrochemical stability window of 0 - 5 V is desirable to ensure safe operation with different electrode materials and over a wide potential range (Figure 1.8) [44, 45]. The electrolyte should also provide low ion flow resistances close to those of liquid while preventing electron movement that would otherwise result in energy loss.

Material and mechanical characteristics Materials must be chemically compatible with other battery components to prevent undesired reactions that can degrade battery performance. They should also have sufficient thermal stability to 1000 °C, such as oxide-electrolytes, to withstand temperature changes without degradation and ensure safe operation [47]. In addition,
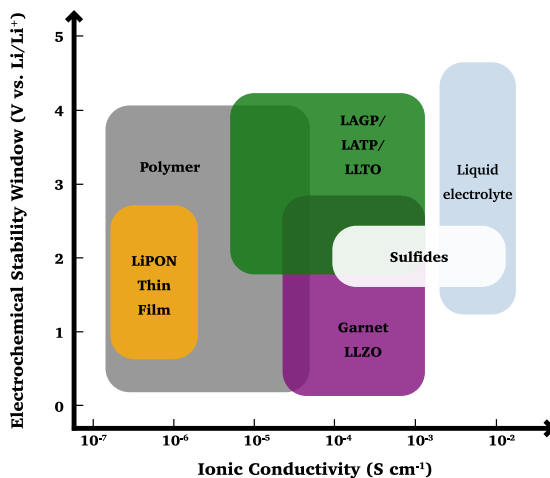
Figure 1.8. Electrochemical window and ionic conductivity of selected solid electrolytes and a typical liquid electrolyte. A visible gap in ionic conductivity appears between solid and liquid electrolytes. Adapted from Chen et al. [46]

the materials should be environmentally friendly, taking into account the environmental impact of batteries from raw material extraction to production and recycling. They must support the general trend toward sustainability [48].

Manufacturing and economical aspects For solid-state batteries to be economically viable, their manufacturing processes must be simple and inexpensive. Simplifying these processes is key to reducing costs and ensuring that batteries are competitively priced in the marketplace. The projected price in 2030 is 80 USD kWh^{-1}, so new materials and batteries should be designed for easy integration into devices without the need for complex

modifications [49]. Such manufacturing and economic considerations are critical to the adoption and success of solid-state batteries as they move from innovative concepts to mainstream energy storage solutions [39].

Numerous materials have shown potential, yet often one must balance between their ionic conductivity, their ability to remain stable across different electric potentials, and their ease of production and integration. Achieving all of these properties simultaneously is challenging, which has led to the emergence of different classes of electrolytes, each with its own set of strengths and weaknesses. Figure 1.9 summarizes these properties for different solid-state electrolyte classes. This Thesis focuses on the first two classes of electrolytes: the oxide-based electrolytes and those used in thin-film battery technology.
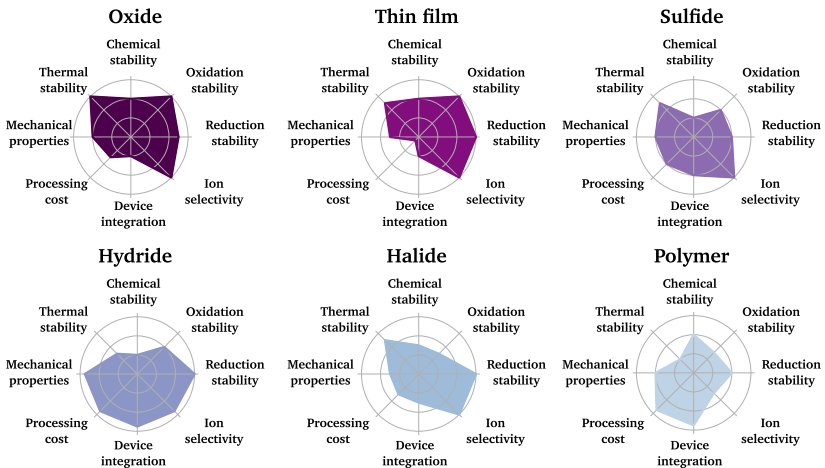
Figure 1.9. Radar plots of the performance characteristics of various solid-state electrolytes. Adapted from Manthiram et al. [42]

Garnet-type electrolytes

The advancement of solid-state batteries has included important research into inorganic oxide electrolytes. Materials such as NASICON ($Li_{1+x}Al_xGe_{2-x}(PO_4)_3$), perovskite-type ($Li_{3x}La_{2/3x}TiO_3$), LISICON-like ($Li_{10}GeP_2S_{12}$), and garnet types ($Li_7La_3Zr_2O_{12}$ also known as LLZO) are at the forefront of current research [50]. Figure 1.10 compares the normalized ionic conductivity, the activation energy of lithium-ion conduction between selected families of structures, and corresponding structures. Bachman et al. [51] show that LISICON-like electrolytes, especially with sulfur anions, exhibit the highest conductivities, but are water-sensitive and less stable, requiring handling under inert conditions. Perovskites and NASICON-like compounds, although lower in conductivity, face challenges in high-temperature sintering and lithium metal stability. Garnet electrolytes, on the other hand, are relatively stable and present fewer synthesis challenges, although they require precise sintering for optimal performance.

Due to its promising properties for solid-state batteries, the garnet-type solid electrolyte LLZO has been the focus of intense research. This material, discovered in 2007 by Ramakumar et al. [52], has an ionic conductivity between 10^{-4} and 10^{-3} S cm^{-1} at room temperature, making it an ideal conductor of lithium ions [53]. Of particular note is its stability in contact with metallic lithium anodes and its ability to operate over a wide range of voltages without degrading [54]. This compatibility can lead to solid-state batteries with higher energy densities, making them safer and more efficient than those with liquid electrolytes, which are prone to flammability and
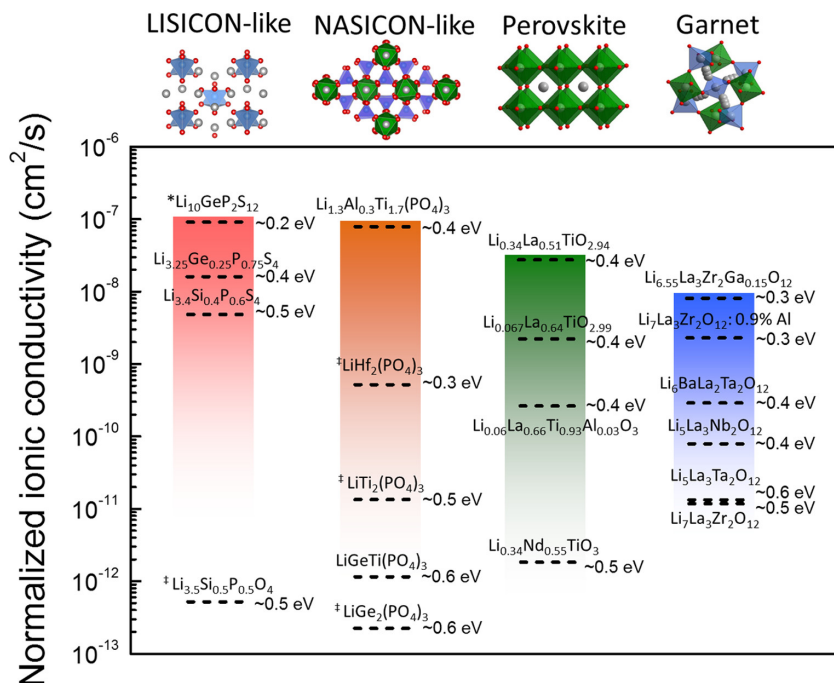
Figure 1.10. Ionic conductivities for selected lithium-ion electrolytes at room temperature. In the structure diagrams, gray spheres represent lithium ions and red spheres represent oxygen ions. [51]

stability issues. Researchers have made significant progress in understanding LLZO, focusing on how it can be synthesized, how it interacts with electrodes and the processes that can cause it to degrade over time.

LLZO manifests itself in different crystal structures that directly influence its ionic conductivity. Of particular importance are the less conductive but more thermodynamically stable tetragonal phase and the more conductive cubic phase [55]. The cubic phase is characterized by a specific arrangement of atoms that allows lithium ions to move efficiently through the material - a

necessary property for batteries that charge quickly [56].

To further improve the properties of LLZO, researchers have developed methods to stabilize the cubic phase at room temperature. This is achieved by replacing lithium with trivalent metal ions such as aluminum, gallium, iron and others [57, 58]. This substitution not only stabilizes the cubic phase, but also improves other material properties such as density and critical current density, which are important for fast charging and long-term battery performance. Figure 1.11 summarizes the different chemical compositions possible in garnet-type electrolytes. Classification of LLZO into different subtypes based on lithium content shows a clear trend: ionic conductivity increases with lithium content [54, 59, 60]. However, not all lithium positions in LLZO contribute to this mobility.

The most advanced form of LLZO is the cubic Li_7 phase (so-called "Li-stuffed" garnet compositions), which achieves high ionic conductivity by incorporating zirconium into its structure and balancing the charge with additional lithium ions [54]. This version of LLZO has the lowest activation energy for lithium-ion movement, making it the most efficient in the garnet class and a key material in the evolution of solid-state batteries. For a more detailed review of LLZO, its crystallological properties, and recent advances, see Wang et al. [56].

LiPON thin-film electrolyte

Some solid electrolytes can be manufactured as thin films by vapor deposition processes such as radio frequency sputtering. These thin-film solid electrolytes have been available since the 1980s, starting with materials
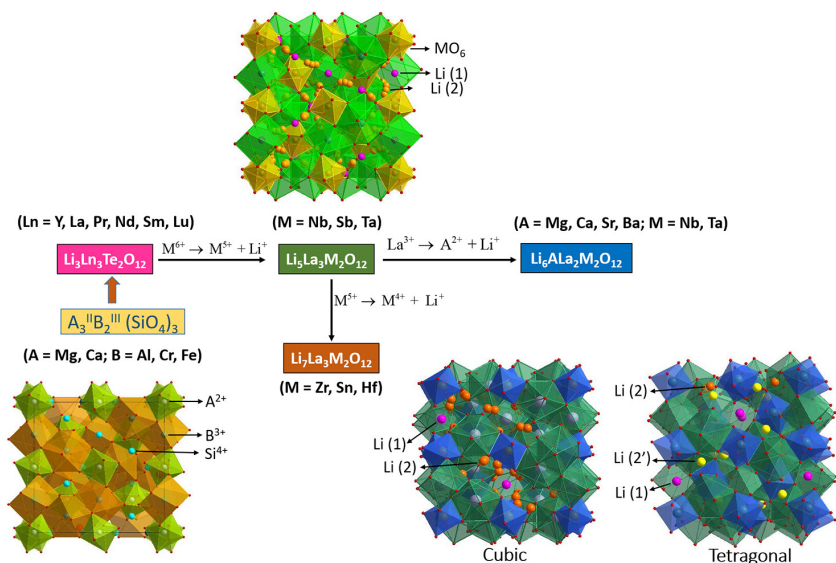
Figure 1.11. Different chemical compositions possible in garnet-type Li-ion conductors. [56]

such as $Li_{12}Si_3P_2O_{20}$ or Li_3PO_4-P_2S_5 [61, 62]. Among these materials, lithium phosphorus oxynitride (LiPON) stands out as a key material for solid-state batteries. LiPON was developed at Oak Ridge National Laboratories in the early 1990s and tailored specifically for thin film battery applications [63, 64]. The addition of nitrogen to the $Li_2O-P_2O_5$ glass system increases the cross-linking between the phosphate chains due to the substitution of non-bridging oxygen ions in the glass network (see Figure 1.12) [65]. This results in double and triple-coordinated nitrogen and an ionic conductivity of about 10^{-6} S cm^{-1}. Although its ionic conductivity is at the lower end of conventional liquid electrolytes - between 10^{-8} and 10^{-6} S cm^{-1} - LiPON's performance is well suited to the requirements of solid-state batteries [66].

This suitability stems from its shorter lithium-ion transport and thus fast charging capability.
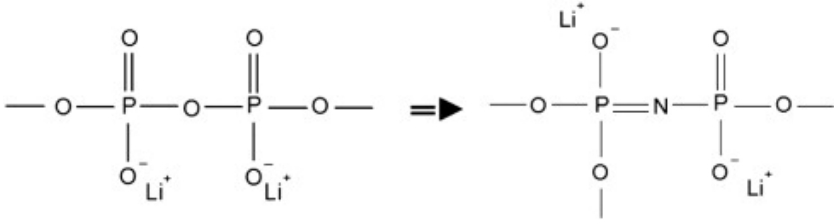
Figure 1.12. Partial structure of the nitride Li3PO4 thin film glass with the incorporation of $= $ N-. Adapted from Fleutot et al. [65]

There are several methods for synthesizing LiPON, including sputtering [67], chemical vapor deposition [68], atomic layer deposition [69], and solid state reactions. Each technique has its own advantages and influences the final properties of the LiPON layer. Typically, LiPON is deposited by RF magnetron sputtering from a Li_2PO_3 ceramic target using a nitrogen process gas for reactive sputtering. The resulting films are amorphous, with no columnar microstructure or boundaries. The stoichiometry of LiPON can be varied by co-sputtering with Li_2O, allowing its properties to be precisely tuned to the requirements of each application. This tunability is important to ensure that the electrolyte exactly matches the requirements of different devices [67, 70].

In solid-state batteries, LiPON serves a dual function as an electrolyte and a protective layer. As an electrolyte, it facilitates the movement of lithium ions between the electrodes; as a protective layer, it prevents the formation and penetration of dendrites, thereby increasing the safety and longevity of the battery. LiPON's chemical resistance is also remarkable.

When LiPON comes into contact with lithium metal, it decomposes into a layer of Li_3PO_4, Li_3P, Li_3N, and Li_2O, which prevents further degradation such as a SEI in conventional liquid batteries. It also withstands a wide range of environments, which is why it is used not only for energy storage but also for a range of other applications such as MEMS [71].

In addition, other electrolyte types such as LATP, LLZO, or LAGP have been developed as thin-film systems in recent years [72–74]. However, they have never been able to match the robustness, performance and market penetration of LiPON.

1.3 Thin-film batteries

Thin-film batteries are a potentially transformative technology for miniaturizing electronic devices and powering microscale computers, sensors, and robots [75]. An advantage of thin-film batteries is that they can be integrated directly into devices without the need for packaging. This integration not only simplifies the design of the device but also improves the user experience by providing seamless power without the interruption of maintenance [76].

In terms of safety, solid-state micro-batteries offer similar improvements over traditional batteries, such as bulk solid-state batteries. They do not contain flammable liquids or environmentally harmful substances, making them a safer choice for consumers and the environment. Another important aspect of these batteries is their ability to withstand high temperatures. Unlike lithium metal batteries, which cannot withstand the high temperatures of soldering processes commonly used in microelectronics due to lithium's

low melting point of 180.5 °C, the anode-free technology in thin-film batteries can withstand temperatures up to 260°C [77, 78].

The architecture of these batteries includes a solid electrolyte that separates the anode from the cathode, with the electrolyte layer often only a few hundred nanometers thick. This compact separation is significantly thinner than the separators found in conventional batteries and thus allows high C rates due to a shorter diffusion length [79].

The first commercial thin-film batteries – EnFilm™micro-battery EFL700A39 – appeared around 2014, with capacities in the tens of microamphours (µAh) range by STMicroelectronics. These batteries typically use Li-CoO$_2$ as the cathode and metallic lithium as the anode, with LiPON as the electrolyte. The overall capacity of the battery is primarily determined by the capacity of the cathode, which is only <1 mAh. To increase the capacity without increasing the size of the battery, a 3D structure can be used to increase the active area within the same footprint [80]. Another innovative approach is monolithically bipolar stacking yielding in the BTRY AG venture [81]. However, thin-film battery manufacturing is complex and involves vacuum deposition techniques such as sputtering, pulsed laser deposition, and atomic layer deposition. These processes are particularly costly, highlighting the economic considerations in thin-film battery manufacturing, and remain one of the biggest obstacles.

In addition to industrial considerations, the layered structure of thin-film batteries provides well-defined interfaces with a total thickness often less than 5 µm (see Figure 1.13a). The key advantage of thin-film batteries is their precise interfacial cell geometry, which makes them an excellent model
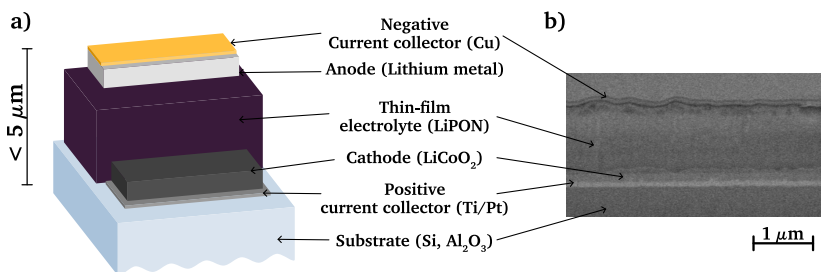
Figure 1.13. (a) Schematic of a thin film battery consisting of Li metal anode, LiPON electrolyte, and LCO cathode on an alumina substrate. (b) A cross-sectional view showing the well-defined interfaces in TFB

for in-depth studies of interfaces and electrochemical processes in solid-state battery systems. It also eliminates the need for additional components such as binders or carbon black. It allows the properties of a battery to be studied in a simplified environment, which is useful for understanding the materials and behavior of batteries in a controlled environment, as shown in Figure 1.13b. Throughout the course of the work, thin-film batteries were primarily employed as a model system to explore and validate various theoretical and practical concepts.

1.4   Interfaces and their challenges

One of the major engineering challenges in solid-state battery research is the creation of stable interfaces between the different components of the battery. Computational models are instrumental in predicting the stability of these solid electrolytes, and experimental investigations provide insight into the nature of different interfaces within solid-state batteries [82]. Figure 1.14

summarizes the challenges associated with the electrode interfaces.
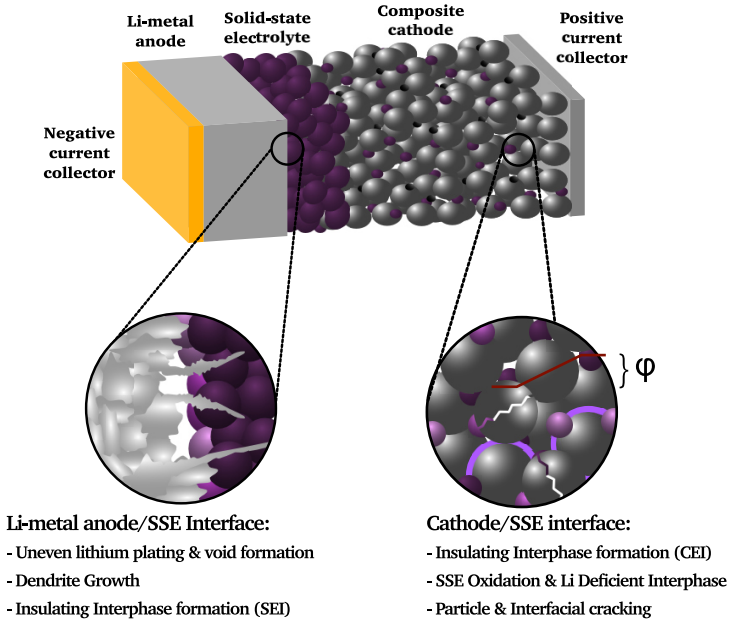
Figure 1.14. Schematic of an all-solid-state lithium metal battery with challenges highlighted. At the anode/SSE interface, challenges include uneven lithium plating, void formation, and dendrite growth. At the cathode/SSE interface, challenges include interfacial impedance, oxidation, and cracking.

Of particular interest is the interface between the cathode and the solid electrolyte. This interface is critical for ion transport - a key determinant of battery efficiency - and for maintaining the thermodynamic stability required for long-term operation. Another concern is the integration of metallic lithium and the potential reduction of the solid electrolyte, which can result in the formation of conductive by-products that degrade battery performance.

Cathode related challenges

The interface between the cathode and the solid electrolyte emerges as a critical factor affecting the rate performance and lifetime of the battery. This is in stark contrast to liquid electrolyte batteries, which do not require the same degree of rigid integration. All-solid-state batteries, especially those composed entirely of oxide components, require a high-temperature co-sintering process to achieve intimate bonding [83]. However, the formation of an insulating cathode-electrolyte interphase (CEI) is a common consequence of high-temperature processing [84, 85]. This CEI layer, while sometimes beneficial as a protective barrier, can impede ion transport if it becomes too resistive. The goal is to control the formation of this layer to ensure that it provides protection without significantly reducing ionic conductivity.

To counteract interface degradation, efforts on interface engineering and cathode coatings are crucial [86]. In particular, metal oxide barriers can be deposited to act as a protective barrier at the cathode-electrolyte interface. They prevent transition metal dissolution and side reactions and limit cathode degradation and electrolyte decomposition [87, 88]. The most stable interlayer materials were predicted to have compositions along the interface between Li_2O and a metal oxide [86]. These coatings are designed to be chemically and electrochemically compatible with both the cathode and the solid electrolyte. Their roles include:

- Blocking chemical interdiffusion to prevent unwanted reactions that can degrade the battery's performance.

- Accommodating the physical volume changes of the cathode material to maintain integrity and contact throughout the battery's operation.

- Efficiently conducting lithium ions and electrons, ensuring the battery can charge and discharge at the desired rates.

Secondly, the solid-state electrolyte is susceptible to oxidation and the creation of a lithium-deficient interphase, particularly in the presence of high voltages or incompatible cathode materials [89–91]. This degradation can lead to a decrease in the battery's overall ionic conductivity and an increase in resistance, ultimately reducing the battery's efficiency and life span.

Lastly, particle and interfacial cracking present significant concerns. The brittle nature of ceramic solid electrolytes means they cannot easily accommodate the stress caused by the repeated volume changes of the cathode during battery cycling [92]. This can result in the loss of physical contact at the interface, leading to increased resistance and, in some cases, complete failure of the battery cell.

Anode related challenges

There are also several challenges to consider on the anode side of solid-state batteries, especially when lithium metal is used. Incorporating lithium metal into batteries is challenging due to its high reactivity, making anode-free configurations an attractive choice. It increases energy density by up to 30 % over lithium metal batteries and simplifies handling and manufacturing processes by using a bare current collector [93]. The lithium metal

anode is then formed electrochemically during the first charge cycle by electrodeposition of lithium from the cathode, known as plating [94].

The primary hurdle for anode-free batteries is the uneven lithium plating and stripping process, which often leads to rapid capacity degradation. The intrinsic reactivity of lithium metal, coupled with its substantial volume changes during plating and stripping, promotes the formation of "dead" lithium. In addition, there is no excess lithium inventory in anode-free configurations to compensate for the active material loss due to side reactions or dendrite formation, exacerbating these problems.

An additional challenge is to achieve homogeneous plating and stripping of the lithium, as irregularities lead to dendrite formation. Dendrites, if allowed to grow uncontrolled, will extend through the electrolyte, causing short circuits and safety concerns [95]. Uneven stripping can lead to the formation of voids, degrading contact quality, and increasing resistance.

These difficulties are compounded by the reactivity of lithium with the electrolyte, the need for a stable solid electrolyte interphase (SEI), and physical changes to the cell architecture due to repeated plating and stripping cycles [96, 97].

Seed or protective interfacial layers are being explored as a promising strategy to address these challenges [98, 99]. These layers aim to stabilize the electrochemical interface, facilitate uniform lithium-ion flow, and inhibit dendrite growth. They can consist of a variety of materials, including carbon-based materials or specific metals capable of forming stable alloys with lithium [100]. The aim is to provide a uniform and stable interface capable of withstanding the stresses and strains associated with lithium plating and

stripping while maintaining ionic conductivity and mechanical integrity [97, 101, 102].

1.5   Aim and structure of the Thesis

The first objective is to address the interfacial challenges in all-solid-state batteries by focusing on the integration of $Li_7La_3Zr_2O_{12}$ (LLZO) solid electrolytes with $LiCoO_2$ high-energy cathodes. The combination of ceramic solid electrolytes and high-energy cathodes often requires co-sintering at high temperatures for effective bonding. However, this process faces hurdles due to diffusion processes andsolid-statee reactions that increase the interfacial impedance. This work investigates various lithiated metal oxide interlayers as potential diffusion barriers to counteract Co/La interdiffusion and improve overall battery performance. **Specifically, different lithiated metal oxide interlayers deposited by physical vapor deposition (PVD) sputtering are compared, and their effectiveness as diffusion barriers and in improving battery performance is evaluated.**

The second objective of this Thesis is to advance the integration of a lithium metal anode in all-solid-state batteries, addressing the hurdles of inhomogeneous plating and delamination. This issue, characterized by uneven lithium distribution and current concentration after lithium plating, often leads to dendrite growth or void formation, resulting in battery failure. The potential solution lies in anode-free solid-state batteries that use seed layers to direct lithium nucleation and enhance nucleation dynamics. This study investigates the role of different seed layers (gold, platinum, and

amorphous carbon) placed between the LiPON solid-state electrolyte and the copper current collector. **Specifically, the focus is on evaluating how these layers influence lithium nucleation dynamics and affect the overall performance of an anode-free thin-film battery.**

Chapter 1 provides historical and theoretical background on lithium-ion batteries and the challenges they face. Chapter 2 describes the fabrication and characterization methods used for thin film batteries. The first part of Chapter 3 presents the study of various lithiated metal oxide interlayers at the cathode interface. The second part of Chapter 3 deals with an investigation of the anomalous voltage drop observed in the first part of Chapter 3 and possible hypotheses. The first part of Chapter 4 deals with the influence of different seed layers and their impact on battery performance. The second part discusses the development of an optical 3D microscopy setup for the investigation of lithium nucleation dynamics at non-ideal interfaces. Finally, Chapter 5 gathers the conclusions and outlook of the Thesis.

2 FABRICATION AND CHARACTERIZATION

2.1 Fabrication techniques

Vapor deposition techniques are widely used for thin film synthesis, where the deposition material is vaporized and condensed on a substrate to form the film. The methods used in this Thesis involve physical vapor deposition (PVD) processes, such as high-temperature evaporation or sputtering.

2.1.1 Substrate preparation

LLZO pellet preparation (Chapters 3 and 4) Commercially available LLZO powder (AmpceraTM, Al-doped LLZO, 500 nm nanopowder) was uniaxially compacted in 80 mm^2 compression molds at a pressure of approximately 15 kN. The pellets were then isostatically densified at 1000 kN. All sides of the pellets were polished with sandpaper for initial removal of surface contaminants. The pre-polished pellets were then covered with pure LLZO

powder and embedded between two Al_2O_3 crucible lids before being placed in a tube furnace (Gero Carbolite). The mixture was sintered at 1140 °C for 10 min (heating and cooling rate of 450 °C h^{-1}) under a constant nitrogen gas flow. Subsequently, the sintered pellets were first polished to a thickness of about 1 mm with rough SiC 320 grit polishing paper and later further polished with 800 grit paper. The resulting pellets were then heat treated in an Ar-filled glove box at 900 °C for 10 min to clean the LLZO surface from high resistance Li_2CO_3/LiOH impurities. The pellet diameters were 7.5 mm with a thickness of 700 µm.

Glass preparation (Chapters 3 and 4)   For all glass substrate experiments, the soda-lime glass substrates were thoroughly cleaned with 2-propanol prior to deposition. Subsequently, they were dried with N_2 gun and used directly.

2.1.2   RF magnetron sputter deposition

Sputtering involves the knock-out of atoms from a target material to create a coating on a substrate. Figure 2.1 shows a schematic of the deposition chamber and the system used in this Thesis. The sputtering process takes place under vacuum, which is essential to reduce impurities in the resulting film. Inside this chamber, an inert gas, typically argon, is ionized by an electric current. The positively charged ions produced by this ionization then bombard the target material. This bombardment causes atoms to be ejected from the target and deposited as a thin film on the substrate [103]. Radio-frequency (RF) sputtering enhances the sputtering process by using an alternating current to generate radio waves that ionize the gas. While

RF sputtering is slower than direct current (DC) sputtering, more commonly used in industry, it is necessary to deposit insulating ceramics such as $LiCoO_2$, NMC, or dielectric materials such as LiPON or LLZO. These materials are crucial in thin film battery technology [104–106].
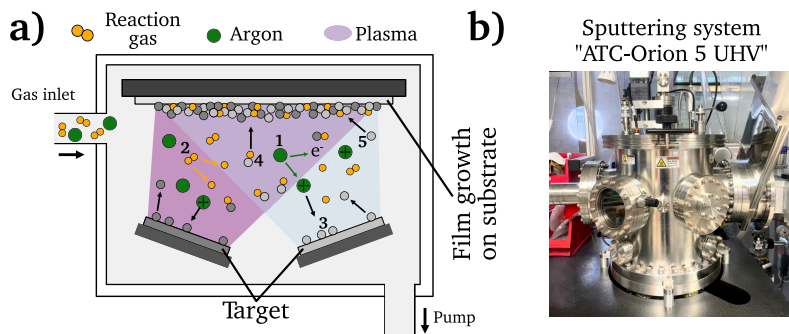
Figure 2.1. a) Schematic of a sputtering machine and b) photo of "ATC-Orion 5 UHV" sputtering system used in this Thesis

The experimental conditions are tailored to the specific materials under investigation. RF magnetron sputtering was used as the primary thin film deposition technique. An ATC-Orion 5 UHV sputtering system (AJA International Inc.) with 2-inch targets was used for all sputtered depositions.

Li-Me-O interlayers (Chapter 3) A 10 nm thick amorphous lithiated metal oxide (Li-Me-O) film was deposited by RF sputtering. For this purpose, pure metals (99.9 9% Al, 99.995 % Ti, and Nb) were sputtered together with a Li_2O target (Toshima Manufacturing Co., 99.9 %). The distance between the pellets and the sputtering targets was set to 25 cm, and the sample stage was rotated during deposition. The deposition conditions were 6.1 W cm^{-2} for Li_2O at a pressure of 3 Pa and a gas flow of 24 sccm Ar + 1 sccm

Ar/O_2 at room temperature. The power density for the metals was 1 W cm^{-2} (Nb), 1.5 W cm^{-2} (Al), and 0.8 W cm^{-2} (Ti). For XPS analysis, the films were deposited on a glass substrate and analyzed as-deposited. The thin film interlayers at the solid electrolyte-cathode interfaces may not retain their precise stoichiometric compositions as originally deposited. These compounds may transition to amorphous states, deviate from stoichiometry, or become mixed compositions due to processes such as interdiffusion, co-sintering, or the effects of electrochemical cycling.

LCO cathode deposition and heat treatment (Chapter 3) A $LiCoO_2$ (Toshiba Manufacturing Co., 99.9 %) target was used to prepare films with a thickness of 300 nm and a diameter of 6 mm for the first part of Chapter 3 and 600 nm for the second part. The sputtering conditions were 5.9 W cm^{-2} at a pressure of 3 Pa and a gas flow of 24 sccm Ar + 1 sccm O_2 and at room temperature. The battery stacks (LCO/interlayer/LLZO) were sintered at elevated temperatures (heating to 500 °C for XAS, FIB-SEM, and cycling; 700 °C for EIS, heating rate of 5 °C min^{-1}, cooling naturally) for two hours in a tube furnace (Carbolite Gero GmbH & Co.) at atmospheric pressure with a O_2 gas flow. Further details of the deposition conditions and film properties can be found in the publication by Filippin et al. [107]

LiPON deposition (Chapter 4) Lithium phosphorus oxynitride (LiPON) solid electrolyte was sputtered onto the current collector/seed layer stack. This deposition was performed unheated and resulted in a 1 µm thick LiPON layer using the co-sputtering technique with of Li_3PO_4 (99.95 %, Kurt J Lesker Co., rate about 0.7 nm s^{-1}) and Li_2O (99.9 %, Toshima Manufacturing, rate

about 0.6 nm s^{-1}) in a N$_2$ atmosphere (flow set to 50 SCCM) at powers of 100 W and 120 W, respectively, and a working pressure of 4*10^{-3} mbar. The distance from the target to the substrate was set to 25 cm.

Pt and amorphous C seed layer (Chapter 4)   Platinum (99.99 % Pt, Plasmaterials) and amorphous carbon (99.9 % pure graphite, Mo-bonded, Plansee SE) were deposited using the Orion sputtering system (AJA International Inc.) at thicknesses of 10 nm and 50 nm, respectively. The deposition rate was 2.5 nm min^{-1} for platinum and 0.8 nm min^{-1} for carbon.

Cu current collector on LLZO (Chapter 4)   Copper (99.995 % Cu, AJA) was deposited to a thickness of 5000 nm. The deposition rate was approximately 30 nm min^{-1} at 175 W with a 30 sccm Ar flow at 3 mTorr.

2.1.3   Thermal evaporation

Thermal evaporation involves heating materials to their vaporization point in a high vacuum, typically using resistance heating [108]. The materials then travel from the source to the substrate, forming a thin film coating. A schematic of a thermal evaporation chamber and the system used in this Thesis is shown in Figure 2.2. A Nexdep thermal evaporator (Angstrom Engineering Inc.) was used for all thermal depositions.

Current collectors (Chapters 3 and 4)   As current collectors, 60 nm thick Au contacts with a diameter of 6 mm were deposited on LLLZO stacks from Au (ingots, 4N) at a rate of 0.5 Ås^{-1} at a pressure of 1×10^{-4} Pa. For EIS

a) Vapor flux

Film growth on substrate

Crucible

Pump

b) Thermal evaporator "Angstrom"
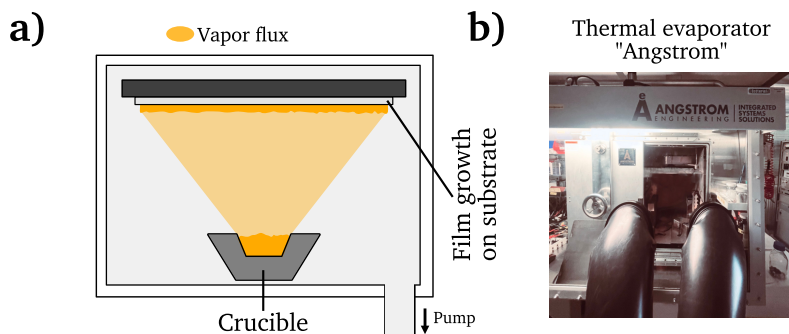
Figure 2.2. a) Schematic of a thermal evaporator and b) photo of Nexdep thermal evaporator used in this Thesis

characterization, we fabricated symmetric cells by depositing Au on the LCO film and the polished back side of the LLZO pellet. Since these symmetric cells have no anode-electrolyte interface, the change in EIS was only the result of changes at the cathode-electrolyte interfaces **(Chapter 3)**.

A 250 nm copper layer (Cu 99.999 %, Thermo Fisher Scientific) was thermally deposited on the glass substrates using a Nexdep evaporator (Angstrom Engineering Inc.) at a rate of 1 Ås^{-1}. A 100 nm layer of copper was thermally deposited on top of the lithium as the final step of the protocol. Throughout the deposition process, a quartz microbalance was used to ensure precise control of the film thickness **(Chapter 4)**.

Lithium deposition (Chapters 3 and 4) For electrochemical cycling of LLZO stacks, Li metal foil anode was isostatically pressed onto the polished pellet at 1000 kN inside a vacuum-sealed airtight latex cover. Full cells were cycled at 80 °C **(Chapter 3)** and at room temperature **(Chapter 4)**.

After LiPON solid electrolyte deposition, a layer of lithium (99+ %,

Thermo Fisher Scientific) was added by thermal evaporation at a rate of 25 Ås^{-1}, forming a 6 µm thick layer with 0.1 cm diameter shadow masks to evaporate individual lithium reservoirs as separate cells **(Chapter 4)**.

Au seed layer (Chapter 4) A 10 nm thick layer of gold (Au 99.99 %, Heimerle + Meule GmbH Scheideanstalt) was thermally deposited on the copper current collector using the Angstrom Engineering Inc. system at a rate of 0.2 Ås^{-1}.

2.2 Characterization

2.2.1 Electrochemical characterization

Cyclic voltammetry (Chapter 3)   Cyclic voltammetry scans were measured at a sampling rate of 0.1 mV s^{-1} between 3 and 4.25 V vs. Li/Li$^+$ and were repeated three times prior to galvanostatic cycling at 80 °C.

Galvanostatic cycling (Chapters 3 and 4)   Galvanostatic measurements of LLZO stacks were performed in a split coin cell on a hot plate in an Ar-filled glove box at 80 °C using a Squidstat potentiostat (Admiral Instruments) with a prior OCV step for 3 h at a current density of 1.75 μA cm^{-2} (C/10 for 300 nm and C/20 for 600 nm cathode layers) between 3 V and 4.2 V **(Chapter 3)**.

The investigation of seed layers included galvanostatic experiments involving the deposition and stripping of a dense lithium metal layer. The constant current conditions were set for a certain duration to obtain a lithium layer of 250 nm or 1 μm, depending on the experiment. A 1 μm layer was cycled at 0.2 mA cm^{-2}. Varying current densities for lithium plating and stripping were tested at current densities ranging from 0.2 to 8 mA cm^{-2} in increments of 0.2 mA cm^{-2}. Each current density increment was repeated five times and maintained for a time corresponding to an offset capacity of 0.05 mAh cm^{-2}. A detailed protocol can be found in Appendix A.3.

The study of plating between LLZO and copper was performed under an Ar atmosphere at room temperature using a Squidstat potentiostat (Admiral

Instruments) **(Chapter 4 – Part 2)**.

Electrochemical impedance spectroscopy   In the context of lithium-ion battery research, electrochemical impedance spectroscopy (EIS) is an advanced non-destructive analytical method. Ohm's law defines how a circuit element resists the flow of current and relates voltage to current by a linear relationship:

$$R = \frac{E}{I} \tag{2.1}$$

However, this concept applies mainly to ideal resistors, which have a constant resistance regardless of frequency. Electrical circuit elements (e.g. capacitors, inductors, etc.) often exhibit more complex behavior, requiring the use of impedance (Z). Impedance extends the idea of resistance with a complex representation and provides a more comprehensive measure of a component's ability to resist electrical current. In this technique, a small sinusoidal perturbation voltage ($E(t)$) (or current) is applied to the system, and the resulting current ($I(t)$) (or voltage) response is measured. The impedance, $Z(t)$, is calculated using the equation:

$$Z(t) = \frac{E(t)}{I(t)} \tag{2.2}$$

EIS can be performed in two primary modes: Potentiostatic EIS (PEIS) and Galvanostatic EIS (GEIS). PEIS applies an AC voltage, while GEIS applies an AC current. By altering the frequency of the input signal in EIS, it is possible to study processes over different time scales, making it a versatile

tool for investigating different dynamic behaviors in batteries. In the context of this Thesis, only the potentiostatic EIS mode was used, which uses a small excitation signal ($| \Delta E | < 50$ mV). The current response to a sinusoidal potential input is also sinusoidal but with a phase shift (see Figure 2.3b). The sinusoidal voltage excitation, $E(t)$, is expressed as

$$E(t) = | \Delta E | \sin(\omega t) \tag{2.3}$$

Where $| \Delta E |$ is the peak voltage amplitude, ω is the angular frequency, and t is the time. The small amplitude of the perturbation allows two critical assumptions: first, that the input and output have identical functional forms, and second, that they have a pseudo-linear relationship. In such a linear or pseudo-linear system, data analysis is facilitated and helps to avoid irreversible changes in the electrochemical system under study. In a pseudo-linear system, the response signal, $I(t)$, has an amplitude $| \Delta I |$ and is phase-shifted φ:

$$I(t) = | \Delta I | \sin(\omega t + \varphi) \tag{2.4}$$

An expression equivalent to Ohm's law is used to calculate the impedance of the system, which is expressed by the magnitude $| \Delta Z |$ and the phase shift φ (see Equation (2.2)).

$$Z(t) = \frac{E(t)}{I(t)} = \frac{| \Delta E | \sin(\omega t)}{| \Delta I | \sin(\omega t + \varphi)} = | \Delta Z | \frac{\sin(\omega t)}{\sin(\omega t + \varphi)} \tag{2.5}$$

Plotting the sinusoidal response signal $I(t)$ on the Y-axis and the applied sinusoidal signal $E(t)$ on the X-axis of a diagram yields an oval called a

"Lissajous figure" (Figure 2.3c). Using Euler's relation ($e^{j\Theta} = \cos(\Theta) + j\sin(\Theta)$), it is possible to represent the impedance as a complex function, with the potential (Equation (2.6)) and current response (Equation (2.7)) derived accordingly:

$$E(t) = |\Delta E| \, e^{(j\omega t)} \tag{2.6}$$

$$I(t) = |\Delta I| \, e^{(j\omega t - \varphi)} \tag{2.7}$$

The impedance is finally obtained as a complex number - composed of a real and an imaginary part - and is usually plotted on a "Nyquist plot" (Figure 2.3d).

$$Z(\omega) = |\Delta Z| \, (\cos(\varphi) + j\sin(\varphi)) \tag{2.8}$$

A Nyquist plot is an important tool for visualizing the frequency response of a system. This plot represents the impedance as a vector of length $|Z|$ at different frequencies (Figure 2.3d). In a Nyquist plot, lower frequencies appear on the right, while higher frequencies appear on the left. However, Nyquist plots have one notable limitation: they do not directly indicate the frequency corresponding to each data point. This can make interpretation difficult, especially when correlating impedance behavior with specific frequencies. To overcome this, Bode plots are often used as a complementary visualization method. In a Bode plot, the logarithm of frequency is plotted on the X-axis, while the Y-axis displays two parameters: the log of the absolute value of the impedance ($|Z| = Z_0$) and the phase shift (Figure 2.3d).
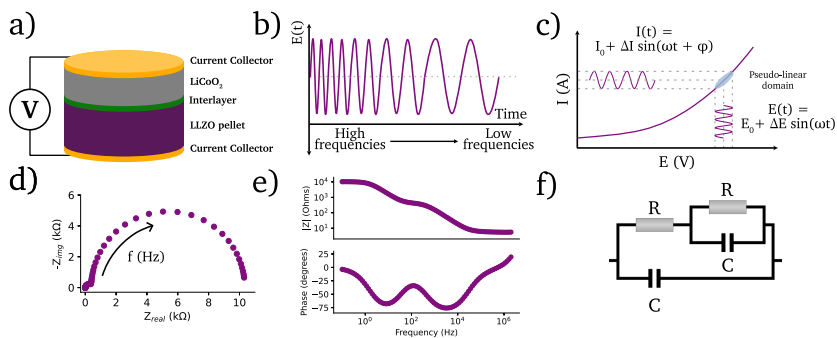
Figure 2.3. A sinusodial potential perturbation is applied from high to low frequencies (b), and the electrochemical response to this perturbation is measured in the pseudo-linear domain (c). The impedance data are presented in Nyquist (d) or Bode plots (e). Fitting the spectra using an equivalent circuit model to interpret the system under investigation (f). Adapted from Wang et al. [109]

Analysis of impedance data often involves fitting it to an equivalent circuit model, where each component has a distinct frequency response and physical meaning. The fundamental properties of the system elements can be determined by examining these responses. Such analysis is integral to the development of equivalent circuit models. Electrochemical impedance spectroscopy models typically include a network of elements arranged in serial or parallel configurations. Table 2.1 lists common equivalent circuit elements along with their physical interpretations in solid-state battery research [110]. The methodical arrangement of elements in a model facilitates a deeper understanding of how each component contributes to the overall behavior of the system (Figure 2.3e). A more detailed overview of the subject is given in the book "Electrochemical Impedance Spectroscopy" by Mark E. Orazem and Bernard Tribollet [111], while this chapter is based mainly on chapters

1 and 4 [112, 113].

Table 2.1. Common equivalent circuit elements, formulas, and physical interpretations in solid-state batteries [110].

Element	Symbol	Formula	Physical Meaning in Solid-state Batteries
Resistor (R)	R	R	Represents the bulk ionic and grain boundary resistances of the solid electrolyte and the charge transfer resistances between the electrolyte and the electrodes.
Capacitor (C)	C	$\frac{1}{j\omega C}$	Represents the charge accumulation or depletion that occurs across the phase boundaries and at the electrolyte/electrode interface.
Constant Phase Element (CPE)	Q	$\frac{1}{Y_0(j\omega)^a}$	Similar to the capacitor, but used for non-ideal capacitances that may be caused by inhomogeneity and porosity of the electrochemical materials and interfaces.
Warburg (W)	W	$\frac{1}{Y_0\sqrt{j\omega}}$	Represents resistance due to mass transfer (diffusion), which is most evident at low frequencies.
Inductor (L)	L	$j\omega L$	Represents high-frequency impedance contributions associated with wound wires/connections and low-frequency degradation.

EIS measurements of symmetric cells **(Chapter 3 - Part 1)** were performed between 5 MHz and 1 Hz with an AC amplitude of 50 mV using a Paios instrument (Fluxim AG) at room temperature. Impedance spectra were fitted using Zview4 software (Scribner Associates Inc.).

EIS measurements of whole cells **(Chapter 3 - Part 2)** were performed between 2 MHz and 100 mHz with an AC amplitude of 50 mV using a Squidstat Plus potentiostat (Admiral Instruments) at 80 °C. A detailed cycling protocoll can be found in Appendix A.2. Impedance spectra were fitted using RelaxIS 3 software (rhd instruments).

2.2.2   Material characterization

X-ray spectroscopy techniques (Chapter 3)   X-ray photoelectron spectroscopy (XPS) and X-ray absorption spectroscopy (XAS) are two important techniques in the field of surface analysis. XPS is known for its ability to probe the outermost layer of materials to depths of about 10 nanometers. Because of its surface sensitivity, XPS is primarily tailored for surface characterization rather than probing bulk material properties. Thus, it is not possible to probe buried interfaces in solid-state batteries [114]. The ability to detect buried layers in materials is one of the major advantages of XAS.

The surface composition of the lithiated metal oxide layers was analyzed by X-ray photoelectron spectroscopy (XPS, PHI Quantera SXM). The Al K_α X-ray source is monochromated at 1486.6 eV and equipped with an Ar^+ sputter source. The spectra were analyzed and processed using the CasaXPS software. The experimental data were analyzed by curve fitting. All XPS spectra were corrected for any charge effects by setting the C 1s binding energy to 285.0 eV and we used a Shirley background subtraction.

The X-ray absorption spectroscopy (XAS) spectra for the O K edge and the Co $L_{2,3}$ edge were recorded at the SIM beamline (Surface/Interface Microscopy) of the Swiss Light Source (SLS) in Switzerland. The total electron yield (TEY) signal is derived from photoelectrons from the top surface layer. In addition, to compare surface species with bulk components, the total fluorescence yield (TFY) signal was acquired with a depth analysis of several hundred nanometers. To reach the interface, the thickness of the top LCO layer was reduced to 50 nm. The data were analyzed using Athena

software and processed in Python.

FIB-scanning electron microscopy (SEM) & energy dispersive X-ray spectroscopy (EDX)   The structure of the battery stacks **(Chapter 3)** was studied using a multifunctional field emission scanning electron microscope (FEI Quanta 650) combined with a Thermo Fischer EDX system. In the preparation phase, cross sections were cut at 30 kV and 9.3 nA, followed by a polishing process at 0.23 nA. For imaging, the ICE mode was used at 5 kV and 0.1 nA. EDX imaging was performed using a 20 kV acceleration voltage with a current of 0.4 nA. This methodical approach provided comprehensive insight into the material composition and structural integrity of the battery stacks. A Gaussian filter was applied to the EDX mappings (standard deviation for the Gaussian kernel: $\Sigma_{Co} = 2$, $\Sigma_{La} = 3$) using Python.

Cryogenic FIB-SEM (cryo-FIB-SEM) is another advance in this field. It has been used in battery characterization of Li metal anodes to study beam sensitive materials and interfaces within the battery system, ranging from alkaline metal anodes [115, 116], alloy anodes [117] and associated interfaces [118, 119]. The plated lithium morphology in seed layer cells **(Chapter 4)** was investigated using a Helios 600i TFS FIB/SEM system with a cryogenic stage operated at -140 °C. A protective carbon layer was deposited prior to FIB milling. The micrographs shown were taken in backscattered electron mode (2 kV, 0.69 nA).

Other microscopy techniques (Chapter 4)   Atomic force microscopy was performed in air using the scanning mode of the ScanAnlyst (Bruker Icon 3). A 2.5 µm x 2.5 µm area was scanned at a resolution of 256x256 pixels. Data

analysis was performed using GWyddion 2.62. The top surface of battery stacks was studied using an optical microscopy setup (KEYENCE VHX-7000). Picture were taken in the RBG mode.

3 CATHODE | SOLID-STATE ELECTRO-LYTE INTERFACE

This chapter describes the integration of $Li_7La_3Zr_2O_{12}$ (LLZO) solid-state electrolytes with a high-energy $LiCoO_2$ cathode, focusing on the interfacial impedances due to diffusion processes and solid-state reactions during co-sintering at elevated temperatures. The study introduces lithiated Nb, Al, and Ti metal oxide interlayers and investigates their role as diffusion barriers to mitigate the formation of detrimental interphases at the cathode-electrolyte interface, thereby facilitating efficient Li-ion transfer between $LiCoO_2$ and LLZO.

It also evaluates how these modifications affect the electrochemical behavior of the battery stacks after high-temperature processing. The results indicate a significant decrease in Co/La cation mixing at the interface when metal oxide diffusion barriers are used. Electrochemical impedance analysis shows that the interfacial impedance decreases, and cells with interlayers have a higher discharge capacity.

In the second part of the chapter, the observed "kink", a voltage drop

during discharge, is further investigated. To better understand the phenomenon, the battery stack was tested at various C rates and with extensive electrochemical impedance spectroscopy. The subsequent evaluation leads to several hypotheses about the origin of the kink, including possible instabilities in the solid electrolyte interphase, mechanical stresses in the electrode materials, non-uniform lithium distribution, or subtle operational structural changes.

3.1 Introduction

The recent development of $Li_7La_3Zr_2O_{12}$ (LLZO) and its doped compositions are promising as they have comparable conductivities as liquid electrolytes ($\sigma > 1 \times 10^{-4}$ S cm^{-1}) [121], have high chemical stability [44, 122], are easy to handle in the environment, and therefore offer great opportunities for use in ASSBs. While the application of Li metal as anode has been extensively studied and a sound progress has been achieved for its implementation [101, 123], the integration of high energy cathodes remains a major challenge in ASSB development [124, 125]. The main obstacles include electrolyte oxidation and the formation of Li-deficient interphases, mechanical instability such as formation of microgaps due to volume changes of the active materials, and cation interdiffusion due to co-sintering for intimate bonding [89].

The most studied active cathode materials are layered cathodes such as $LiCoO_2$ (LCO) or the $LiNi_xMn_yCo_zO_2$ (NMC) classes. Co-sintering of the various transition metal oxides and ceramic electrolytes at temperatures > 500 °C is required to ensure uniform physical contact [89]. On the one hand, without such a high-temperature process, the interface would be severely limited to point contacts, complicating the transfer of Li$^+$ charge carriers involved in the redox reaction [126]. On the other hand, such high-temperature processes also lead to the interdiffusion of elements and the formation of phases from decomposition products [127–129] with high interfacial impedances [130]. In their recent work, Yildiz and her team have shown that the formation of secondary phases of decomposition products

such as $LaCoO_3$ and $La_2Zr_2O_7$ has a significant impact on the dynamics of the cathode-electrolyte interface [84, 131]. Furthermore, it is shown that such phases can form not only at sintering conditions (>700 °C), which are common for ceramics, but also at much lower temperatures (<500 °C) [132, 133].

To mitigate diffusion, so-called artificial solid electrolyte interlayers can be deposited to act as a protective barrier at the cathode-electrolyte interface [134]. Metal oxide barriers can improve the structural integrity of the interphase and prevent the dissolution of transition metals and side reactions, as well as limit cathode degradation and electrolyte decomposition [87, 88]. Understanding the oxidation kinetics of SEs and the suppression of interfacial degradation during high-temperature fabrication and cycling is one of the keys to determine the lifetime of an interlayer.

In their first-principles computational study, Nolan et al. [86] systematically investigate the thermodynamic stability of LLZO and high-energy cathodes to identify the most promising materials that can stabilize the interface. The most stable interlayer materials were predicted to have compositions along the interface between Li_2O and a metal oxide. In particular, ternary Li-Me-O compositions were found to be stable. However, experimental benchmarking and verification of these interlayers is needed to stabilize the cathode-electrolyte interfaces and make ASSBs with high-energy cathode materials feasible.

In the present study, the effects of interlayers predicted by Nolan et al. [86] at the cathode-electrolyte interface are investigated. Three different material Li-Me-O interlayers are benchmarked in terms of their compatibility

with high-temperature fabrication and the resulting electrochemical performance. By combining a thin film LCO cathode with a bulk LLZO electrolyte as a solid-state battery model, the effects of each interlayer on battery performance can be disentangled. In addition, the effects of interfacial modification become more prominent, as the effects on a thin cathode layer are much more pronounced than on a micrometer-thick bulk cathode. Reducing the thickness of the cathodic layer also improves access to the interfacial area. As a result, one has access to a wide range of characterization techniques for understanding the properties of the interface.

By combining a thin film LCO cathode with a bulk LLZO electrolyte as a solid-state battery model, the effects of each interlayer on battery performance can be disentangled. Intermediate Li-Me-O layers of 10 nm were deposited between the LCO and LLZO pellets by RF magnetron sputtering to serve as an interlayer. The thickness of the interlayers was chosen based on literature values showing that too-thin layers do not provide sufficient protection, while too thick layers lead to an increase in resistance due to low conductivity [101, 135–137].

3.2 Benchmarking lithiated metal oxide interlayers

3.2.1 Results and discussion

Cathode and interlayer characterization

To understand the chemical composition of all Li-Me-O interlayers, XPS was performed on films deposited on a Si reference substrate (Figure 3.1). For the Li-Nb-O film, the Nb 3d spectrum (Figure 3.1a) shows three distinct peaks at 208.9 eV, 206.1 eV, and 203.5 eV. The main contributions can be assigned to the +4 and +5 oxidation states of Nb, and a slight contribution from metallic Nb in the lower energy range [138, 139]. In contrast, the Al 2p spectrum for the Li-Al-O composition (Figure 3.1b) shows a single peak at 73.2 eV with a slight shoulder in the lower binding energy region. The higher intensity peak was assigned to the +3 oxidation state and the formation of Al-O bond, while the low-intensity peak is attributed to metallic Al [140, 141]. The binding energy of the latter intensity is about 0.4 eV higher than that of metallic Al. This is attributed to the fact that the binding energy of a small metal cluster, such as in thin films, shifts to a higher value compared to that of the bulk metal [142–144]. Figure 3.1c shows the spectrum of the Ti 2p signal for the Li-Ti-O thin film. The two peaks at 462.9 eV and 457.1 eV correspond to the characteristic peaks for Ti^{3+} [145]. While the contribution of the main peaks is assigned to Ti^{3+}, the small shoulder in the lower binding

energy regions at 454.5 eV and 461 eV and comes from Ti^{2+} and metallic Ti [146].

A well-controlled oxidation state enhances interlayer stability, making it resistant to atom diffusion and improving its function as a barrier during high-temperature co-sintering [86]. Depositing interlayers in a pure argon environment, free from reactive gases, reduces oxide formation, favoring lower oxidation states or metallic phases. This can lead to interlayers with increased density and modified electronic structures, enhancing their effectiveness as diffusion barriers. However, less oxidized compounds tend to be more reactive, potentially resulting in higher resistances [147].

Although the thin interlayers at the cathode-electrolyte interface do not have an exact stoichiometric composition, they still form a trend in the space of the ternary Li-Me-O composition. Subsequent co-sintering is apt to change the composition in either direction. However, the influence of the respective ternary Li-Me-O interlayers on cation mixing, especially of Co/La, and cell performance remains to be investigated.
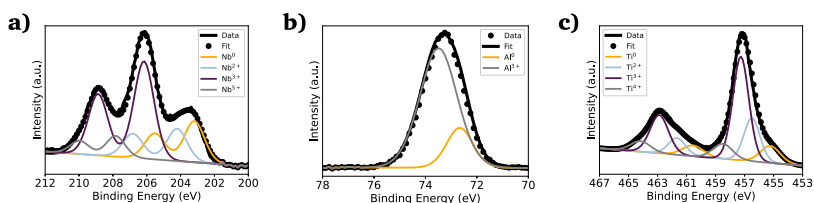
Figure 3.1. XPS spectra of the core-level metal spectra for a) Li-Nb-O, b) Li-Al-O, and c) Li-Ti-O

To not obscure the morphology of the LCO cathode layers, the upper 60 nm thick gold layer was omitted for the SEM studies (Figure 3.2a). An

apparent color change at the edge of individual cathode electrolyte layers after co-sintering can already be seen before the SEM examinations (Figure 3.2b).While the color change is noticeable for the samples without interlayer and Li-Ti-O interlayer, the color changes for the other two samples (Li-Nb-O and Li-Al-O) are only faintly visible. This already indicates a possible solid-state reaction at the interface. To examine whether the morphology of the cathode layer also undergoes changes during co-sintering, the stacks were examined in the as-deposited and sintered states. Figure 3.2c shows an SEM image of a stack as it was deposited. The image shows that the LCO cathode film covers the entire surface and has an amorphous, homogeneous structure, which is crucial for the electrochemical functionality of the battery. In contrast, Figure 3.2d shows the top view of a co-sintered stack with micrometer-sized LCO crystallites. Thus, not only an apparent color change at the edges of the cathode electrolyte layers but also a change in the morphological structure of the uppermost cathode layer can be seen.

To detect the electronic structure changes that occur during the co-sintering process, XAS measured in the fluorescence mode (TFY) was used (Figure 3.3a). To reach the interface, the thickness of the LCO layers was reduced to 50 nm. The XAS spectrum for the Co $L_{2,3}$-edge is shown in Figure 3.3b for an LCO|LLZO sample after co-sintering at 500 °C in oxygen compared to the deposited state. Looking at the XAS Co $L_{2,3}$-edge, one can see two absorption lines at 795.8 eV and 781.7 eV corresponding to the L_2 and L_3 edges, respectively [148]. In the spectra of cobalt oxide, a shoulder on the low energy side at 779.8 eV of the Co $L_{2,3}$-edge indicates reduced cobalt (Co^{2+}), while a shoulder at higher energies indicates more oxidized states of
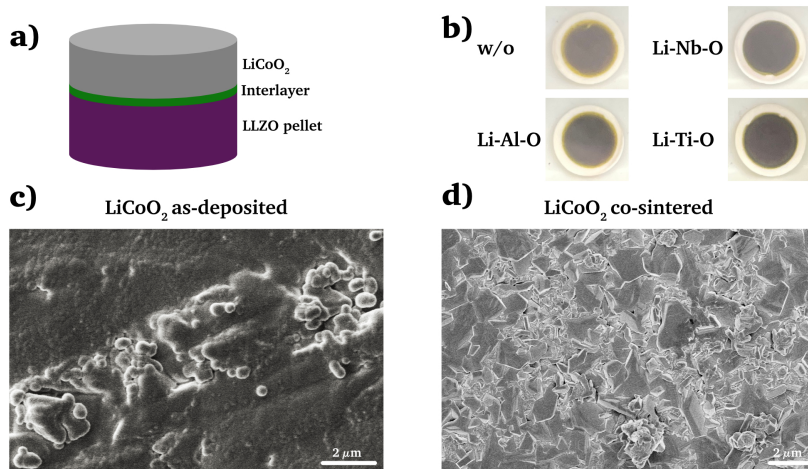
Figure 3.2. a) Schematic of an LCO|LLZO stack, b) image after co-sintering the pellets with LCO, (c) top view of an as-deposited LCO layer, and (d) top view of the LCO layer after co-sintering at 500 °C.

cobalt [148]. As shown in Figure 3.3b, the contribution of the low-energy shoulder decreases with annealing temperature in the co-sintered LCO|LLZO sample. This change in the peak shape of the L_3-edge indicates an increase in the Co oxidation state during co-sintering. In addition, there is a significant change in peak full width half maximum (FWHM) after co-sintering at 500 °C compared to the as-deposited state. Both edges - Co L_2 and L_3 - became significantly sharper when heated to 500 °C. This change is consistent with an increase in local order in the cobalt environment due to co-sintering, and supports the earlier hypothesis that micrometer-sized crystallites form [131].

Figure 3.3c shows the O K-edge spectra for the LCO|LLZO sample without interlayer, before and after thermal treatment, as well as reference measurements on LCO and LLZO. The feature typical of $LiCoO_2$ at about 530.8 eV can

be clearly identified for the as-deposited LCO|LLZO sample [149]. However, annealing at 500 °C leads to a significant decrease in this feature, which is most likely related to the sudden appearance of the large Li_2CO_3 feature (534.6 eV) [150]. Moreover, the peak associated with LLZO at 532.9 eV lost intensity compared to LCO, suggesting that LLZO may decompose to $La_2Zr_2O_7$ or $LaCoO_3/La_2CoO_4$ [146, 149].
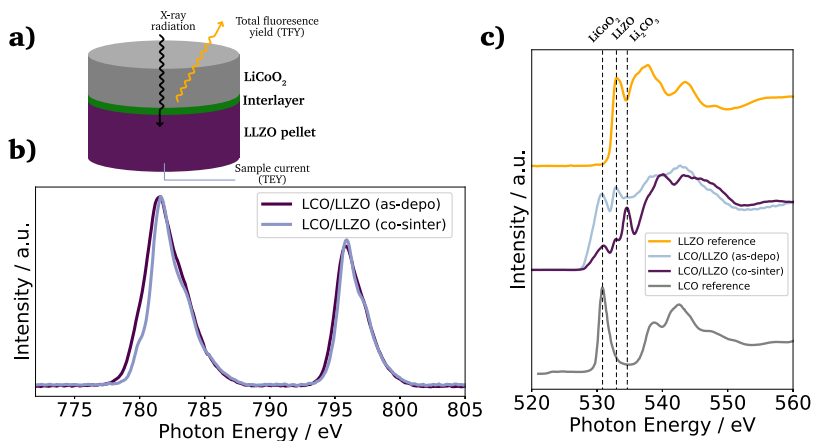
Figure 3.3. a) Schematic of the XAS measurement geometry, b) Co L$_{2,3}$-edge, and (c) O K-edge in fluorescence mode (TFY) for LLZO, LCO, and 50 nm LCO|LLZO as-deposited and annealed at 500 °C in oxygen.

Figure 3.4a shows the Co L$_{2,3}$ XAS spectra for all samples tested. The spectra show no noticeable variation between different interlayers, except for differences between as-deposited and co-sintered samples. This variation, characterized by a change in peak shape, suggests an increase in the local order of the cobalt environment.

In the O K edge spectra (Figure 3.4b), similar observations are made: no marked differences between interlayers at identical temperatures. The

as-deposited sample shows a barely perceptible carbonate feature, while the annealed samples show a distinct increase, overlapping the weaker signals of LCO and LLZO.

In view of the fact that all samples were always handled under an inert atmosphere or high vacuum and were not in contact with the environment, we attribute this increase to contamination during sputtering by carbon residues from other processes. This increase is attributed to carbon contamination during sputtering, despite the fact that the samples were handled in an inert atmosphere or vacuum. This contamination is thought to be due to carbon residues from previous processes. Subsequent annealing in a pure oxygen atmosphere eventually leads to oxidation of the carbonates. This is supported by the fact that the pristine LLZO sample, which was not in the sputtering chamber, has no Li_2CO_3 feature.
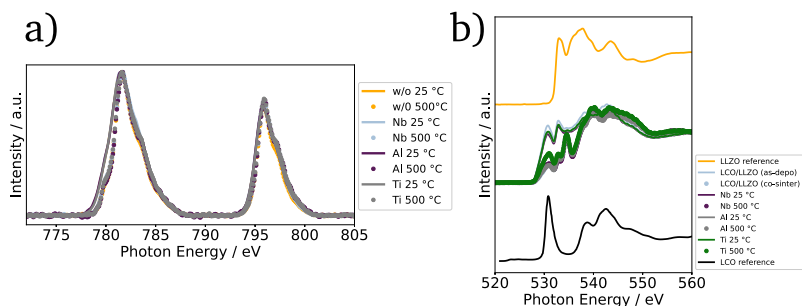
Figure 3.4. a) Co $L_{2,3}$ X-ray absorption spectroscopy data, and b) O K X-ray absorption spectra in fluorescence mode (TFY) for as-deposited and co-sintered samples at 500 °C in oxygen.

To confirm the crystallinity, GI-XRD analysis was performed at an angle of incidence of 1.5° in the range of 42° - 47° on a cell with Au/LCO/LLZO

structure. The X-ray diffraction patterns of LLZO and LCO have comparable peaks, making it difficult to distinguish between the two. The analysis showed that LCO does not have a clear peak in this region, but rather a shoulder around 45.3°. The analysis suggests that the Au top layer may be masking the XRD pattern, resulting in reduced intensity and limited visibility of the peaks. Specifically, it appears that the presence of the Au layer causes the XRD pattern of LCO to be attenuated, resulting in the observed shoulder-like feature at 45.3°.
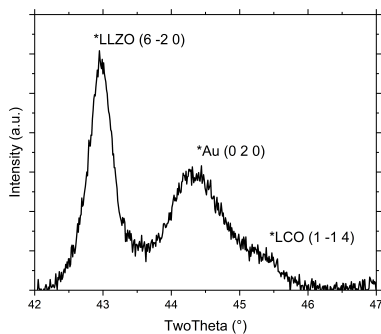
Figure 3.5. GI-XRD analysis of Au/LCO/LLZO stack

Elemental distribution at the interface

Figure 3.6 compares the elemental distribution at the interface between cathode and electrolyte in co-sintered stacks. By studying the interface with a combined FIB-SEM/EDX approach, it is possible to gain insight into the cation intermixing at the interface. To compare the different samples, cross-sectional SEM images are shown in conjunction with the EDX elemental

distribution maps for Co and La. Figure 3.6a shows the interface with no interlayer. As previously shown by Vardar et al. [131] and Park et al. [151], direct crystallization of LCO on garnet electrolytes such as LLZO is detrimental to a chemically stable interface.

The high-temperature co-sintering at 500 °C leads to uniform physical contact between the electrolyte and the cathode but results in cross-diffusion of the elements. As can be seen, the boundaries in the Co and La mappings at the cathode-electrolyte interface were diluted by co-sintering when no interlayer is present. This is indicative of partial diffusion of Co from the LCO into the electrolyte and likewise of La from the electrolyte into the cathode film [151].

In contrast, the interface maps for stacks with Li-Me-O interlayers show a clearer, sharper boundary (Figure 3.6b-d). In particular, the signal intensity of Co at the interface is found to be much more intense in the stacks with the interlayers. This confirms that the interlayers act as an effective diffusion barrier against Co diffusion. These observations are supported by the intensity lines of all samples. A much steeper intensity drop in the Co signal is observed for the stacks with an interlayer compared to the stack without. In contrast, the intensity for the stack without an interlayer drops only gradually, consistent with Co diffusion into the LLZO electrolyte. The high La signals in the LCO layers (for all stacks) are attributed to the fact that the interaction volume for EDX measurements is much larger than the 300 nm thick cathode. La is also detected through the thin LCO cathode film. However, besides the EDX measurements, all cross-sections show a structurally reliable interface. This is further proof of good conformal phys-

ical bonding between the different layers after co-sintering. The question arises about what influence the deposited Li-Me-O interlayers have on Li^+ diffusion and whether this is also influenced.
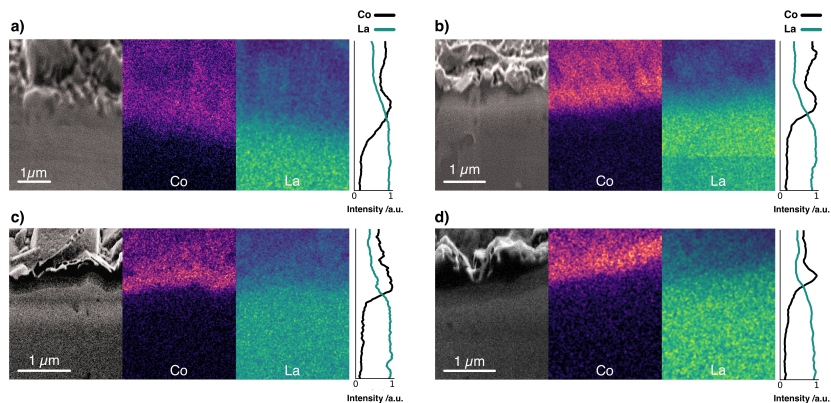
Figure 3.6. FIB-SEM image and elemental mapping of Co K series and La L series of a stack a) without interlayer, and with b) Li-Nb-O, c) Li-Al-O, and d) Li-Ti-O interlayer.

Interfacial impedance at the cathode|electrolyte interface

Electrochemical impedance spectroscopy was used to quantify the charge transfer resistance at the cathode-electrolyte interface [110, 152]. This study involved half-cells (Figure 3.7a), both with and without interlayers, to assess the impact of various Li-Me-O interlayers on charge transport. The impedance spectra were analyzed using an equivalent circuit model (Figure 3.7b), previously applied for the LCO|LGPS solid-electrolyte interface [153]. The terms interface$_1$ and interface$_2$ denote the cathode-electrolyte and current collector (CC)-electrolyte interfaces, respectively.

A detailed deconvolution of the different semicircles is explained in more detail using the Li-Nb-O sample (Figure 3.7c). To display the deconvolution of the impedance spectra in a more convenient way, the EIS data are shown at various magnifications. The high-frequency region's semicircle, observed at room temperature, corresponds to the LLZO pellet, where grain and grain boundary contributions to LLZO conductivity overlap. Another semicircle in the middle-frequency region relates to the cathode-electrolyte interface (int_1), indicating charge transfer resistance. This semicircle is smaller and less visible compared to the CC-electrolyte interface (int_2) semicircle. Resistance and capacitance variations at int_2 are linked to surface characteristics such as roughness. Additionally, the low-frequency tail signifies the blocking effect of the Au electrodes [154, 155].
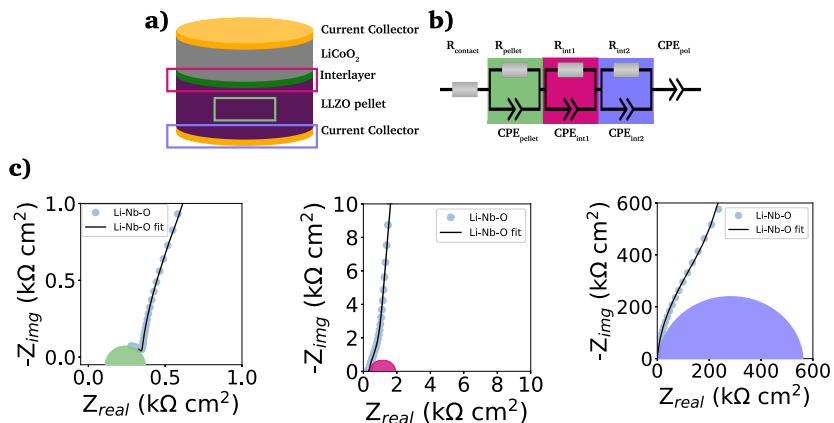
Figure 3.7. a) Schematic of the half-cell structure for room temperature electrochemical impedance spectroscopy for symmetric cells, b) equivalent circuit for fitting the impedance spectra, and c) deconvolution of the Nyquist plot using Li-Nb-O as an example with different magnifications.

The Nyquist plots for the samples, as illustrated in Figure 3.8c-f, display the impedance spectra of half-cells, both with and without interlayers. These plots specifically focus on the mid-frequency impedance region, highlighting the impedance contributions attributable to the cathode-electrolyte interface.

The typical semicircle contribution of bulk LLZO electrolytes appears at frequencies above 1 MHz, and the intrinsic impedance and capacitance components for the LLZO pellets can be extracted from the equivalent circuit. The resulting refined capacitance values for the total resistance of LLZO average 90 nF cm^{-2} and range between 10^{-12} and 10^{-9} F cm^{-2}, thus are consistent with the expected capacitance values of the respective charge transport phenomena [156–159]. The ionic conductivity was extracted from the EIS data and is within the expected range at 5 mS cm^{-1} [56].

The semicircle for the electrolyte is followed by a second semicircle in the mid-frequency range (from 500 kHz to 1 kHz), which is characteristic for the cathode-electrolyte interface (interface$_1$) [153]. Due to the large influence of interface$_2$ and the resulting large semicircle in the low-frequency range (from 1 kHz to 1 Hz), the semicircle for interface$_1$ is strongly shaded in the middle-frequency range. The semicircles plotted in the figures correspond to the calculated semicircles from the values of the fits.

The charge transfer resistance at the interface between cathode and electrolyte is about 8 kΩ cm^2 for the unmodified stack due to the degraded solid cathode-electrolyte interface [160]. This value is in the same order of magnitude as that reported by Sastre et al. [161] in their thin-film system and Vardar et al. [131]. The slightly higher value compared to Sastre et al. [161] can be explained by the extended co-sintering time at 700 °C leading to
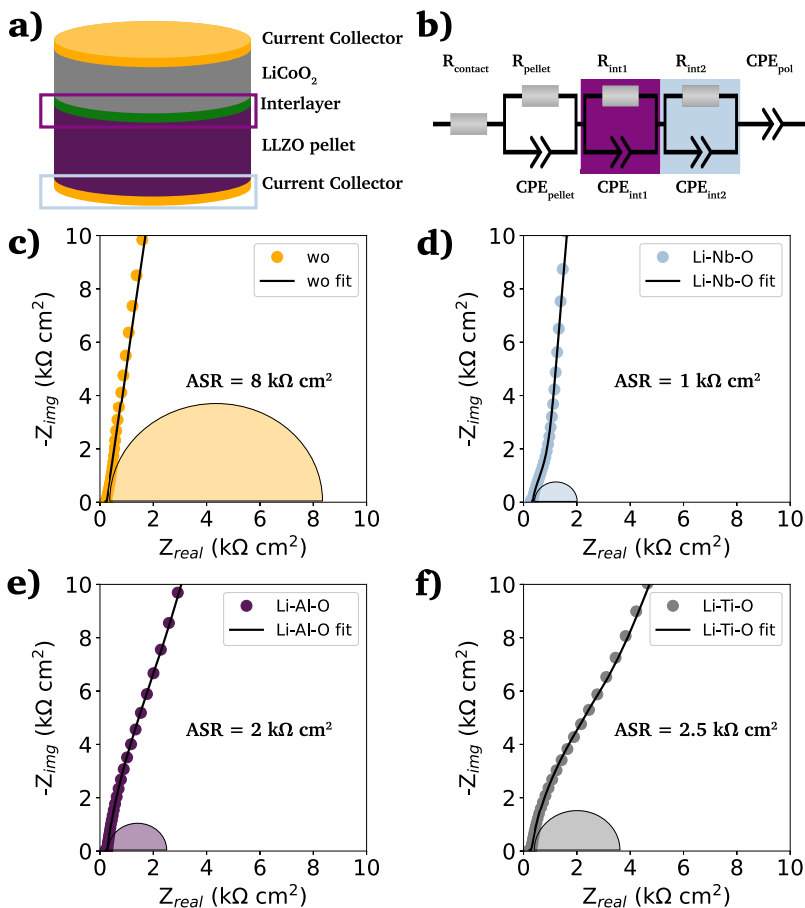
Figure 3.8. a) Schematic of half-cells structure for electrochemical impedance spectroscopy at room temperature for symmetrical cells, b) equivalent circuit model used to fit the impedance spectra by Zhang et al. [153], EIS spectra of c) Au|LCO|LLZO|Au (w/o), d) Au|LCO|Li-Nb-O|LLZO|Au (Li-Nb-O), e) Au|LCO|Li-Al-O|LLZO|Au (Li-Al-O), and f) Au|LCO|Li-Ti-O|LLZO|Au (Li-Ti-O). The measured data are shown together with the fits from the equivalent circuit.

a higher degree of interface degradation. In addition, the value is consistent with the observation by Vardar et al. [131] that the area resistivity (ASR) increases upon annealing.

It has been shown that the Li-Nb-O interlayer reduces the charge transfer resistance at the cathode-electrolyte interface by an order of magnitude. With a value of 1 kΩ cm^2, it is significantly lower than the stack with no interlayer, again demonstrating the positive effect of a Li-Nb-O interface [136, 161–164]. The impedance spectra show no clear difference in electrolyte resistance between the stacks without and with the Nb-oxide interlayer, while the charge transfer resistances differ significantly [136]. The other lithium-containing metal oxide layers (Li-Al-O or Li-Ti-O) have a similar effect on the interface. The Nyquist diagrams of these interface-modified half-cells (Figure 3.8e-f) show three semicircles as before. It can also be seen that each modification leads to a decrease in ASR compared to samples with no interlayer, namely, 2 kΩ cm^2 and 2.5 kΩ cm^2 for Li-Al-O and Li-Ti-O, respectively.

Electrochemical characteristics of full cells

Cyclic voltammetry (CV) and galvanostatic charge/discharge experiments on a full cell configuration with Li metal foil as an anode (Figure 3.9a) have been used to investigate the charge transport dynamics at the cathode-electrolyte interface. Figure 3.9b shows the CVs of the full cells with and without interlayers. The scans for Li-Al-O, Li-Ti-O, and with no interlayer are characterized by two corresponding reversible redox peaks with similar shapes, matching the main lithiation/delithiation processes in LCO at

approximately 3.9 V vs. Li/Li$^+$ [165, 166]. However, one can notice an increased split between the peak positions of the modified full cells compared with the stack with no interlayer. The higher peak split is attributed to the increase in electrode thickness as an additional interphase is added between the electrolyte, and the cathode [167, 168]. Additionally, it is observed that the cells with interlayer have higher peak cathodic and anodic currents. This indicates a higher electrochemical activity of the full cells - an indication of faster and unhindered ion transport across the interface. Furthermore, no additional redox peaks are observed in any of the cyclic voltammograms, indicating that no secondary phases are involved in the redox process.

Surprisingly, the CV scan of the Li-Nb-O interlayer shows a different pattern. While the cathodic peak is still at about 3.9 V vs Li/Li$^+$, the anodic peak shifts to about 4 V vs Li/Li$^+$. Both peaks have a much steeper slope in the scan compared to other samples. Nevertheless, it can be seen that the electrochemical activity is still present and outperforms that of the reference cell with no interlayer in the cathodic peak.

To better understand and account for the anomalous behavior of the Li-Nb-O interlayer, as well as to evaluate the performance of the Li-Me-O modifications compared to the reference with no interlayer, galvanostatic cycling was performed in the next step. Figure 3.9c summarizes the charge-discharge characteristics of the full battery stacks. The stacks have been cycled with a current of 1.75 µA cm^{-2} (C/10) for ten cycles. The lower and upper cutoff potentials were chosen to be 3 V and 4.2 V, respectively, as they cause the smallest degree of damage to the positive electrode [169]. For all cells, a voltage "plateau" at 3.9 V vs. Li/Li$^+$ in the charging step can be
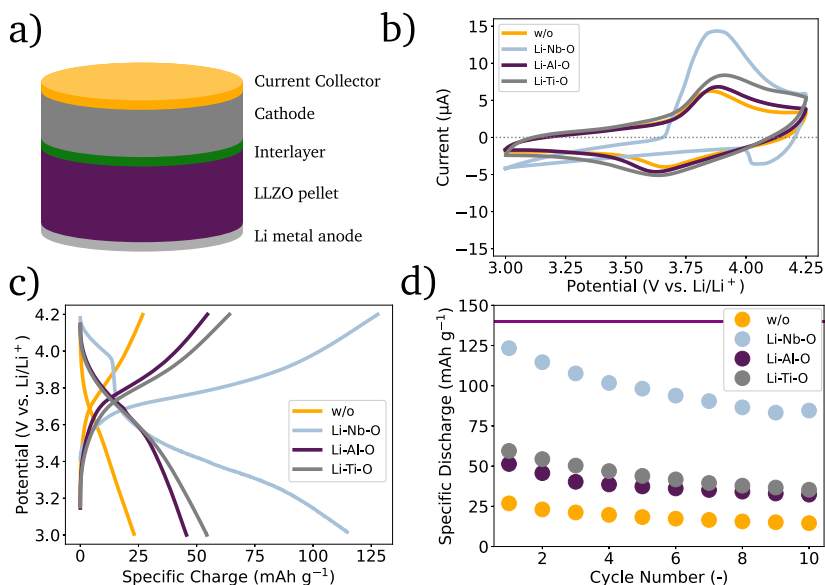
Figure 3.9. a) Schematic of full cells for electrochemical measurements, b) cyclic voltammetry scans measured with a sampling rate of 0.1 mV s^{-1} between 3 and 4.25 V vs. Li/Li^{+}, c) charge–discharge curves with 1.75 µA cm^{-2} between 3 V and 4.2 V at 80 °C, and d) specific discharge capacities for full cells with and without interface modification.

observed. As with CVs, the profile is characteristic of the lithiation/delithiation processes in LCO. However, the discharge profiles vary greatly among cells. While it remains at 3.9 V vs. Li/Li^{+} for Li-Al-O and Li-Ti-O, it drops to 3.6 V Li/Li^{+} for cells with no interlayer and to 3.4 V vs. Li/Li^{+} for Li-Nb-O. This is consistent with previous findings of high impedance at the cathode-electrolyte interface [147].

In general, all cells with lithiated metal oxide interlayers exhibit higher specific discharge capacities (Figure 3.9d). The specific discharge capacity

for the first cycle of the unmodified cell only exhibits 26 mAh g^{-1}, steadily decreasing to approximately 15 mAh g^{-1} over ten cycles. As expected, the presence of the interlayers improves the performance of the cells. While the Li-Al-O interlayer has an initial specific discharge capacity of 50 mAh g^{-1}, the capacity more than doubles to 60 mAh g^{-1} with the Li-Ti-O interlayer compared to the unmodified cell. In contrast, the cell with Li-Nb-O interface modification achieves a specific discharge of 125 mAh g^{-1} in the first cycle. The observed overpotential due to charge transfer resistance at the cathode interlayer is minimal given the nA range of applied current, resulting in an overpotential loss of approximately 10 mV in cells without an interlayer. It is suggested that the observed overpotentials are likely due to uneven morphology or suboptimal contact with the lithium metal anode.

However, there is a distinct voltage drop at about 4 V vs. Li/Li^{+} in the discharge curve, consistent with the kink in the CV scan. Similar kinks were also seen in several other samples, e.g., without interlayer. Liu et al. [170] and Luo et al. [171] report similar voltage drops in the discharge process between 3.9 and 3.8 V. However, the feature remains elusive and is not further explained. Yet, it is surprising that the electrochemical activity is only observed during the discharge cycle and not during the charge cycle. Notwithstanding, the reported values are in line with earlier reports of the achieved capacities for similar material structures [147, 172]. Figure 3.10 shows the coulomb efficiency of the different cells and shows that it does not approach the desired values of >99.5 % achieved in liquid electrolytes. Moreover, there is degradation in each cycle, and none of the coatings significantly improves the efficiency. The gradual decrease in capacities

is attributed to both degradations of the Li|LLZO and of the LCO|LLZO interface.
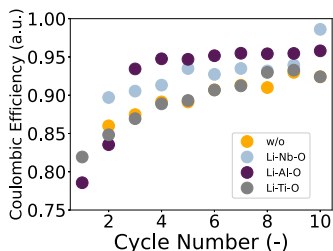
Figure 3.10. Coulombic efficiency of the different cells.

It is speculated that the effect just described may be due to electrochemical and/or mechanical instability at the LCO|LLZO or LLZO|Li interface. For instance, the loss of contact between LCO and LLZO caused by cracking and delamination at the LCO|LLZO interface may have reduced the capacity. Wang et al. [173] suggested that the main reason is microcracks caused by the volumetric changes of the cathode during the electrochemical process. The mechanical degradation at the interfaces accumulates over several cycles and occurs despite the coatings. In addition, it is possible that electrochemically induced cation diffusion during cycling can affect the battery performance. It is worth noting that the capacities achieved still fall short of those reported in liquid LIB systems and other solid-state studies [169]. However, the very thin cathode films used in this study compared to normal bulk cathodes (single cathode particle >3 µm) [174], imply that small changes in the cathode-electrolyte interphase are markedly noticeable.

Nolan et al. [86] describe large stability phases for Li-Nb-O and Li-Ti-O compositions compared to the Li-Al-O system, which are chemically and

electrochemically stable against the garnet LLZO, and are expected to be well suited to stabilize the interface. In the case of the Li-Al-O system, Al-rich compositions near the Al corner have poor stability with LLZO due to the high decomposition energy of the Al-LLZO pseudo-binary. The systems tend to form deleterious products such as $LaAlO_3$, $La_2Zr_2O_7$, etc., due to the tendency of LLZO to lose Li and the corresponding lithiation of the TM oxides. Therefore, the unoxidized Al metal contribution, evident in the XPS studies, can react with the garnet. Moreover, the electrochemical induced diffusion of Al and Co during cycling was observed in other studies, contributing to an increased interfacial impedance [175]. Yet, the reason behind the lower discharge capacities of Li-Ti-O compared to Li-Nb-O is not well understood, but we speculate that Li-Ti-O might be in or near the reactive zone, whereas Li-Nb-O is in the stable region.

3.2.2   Conclusions

In summary, it is found that battery performance is improved after co-sintering when thin interlayers of Li-Me-O are present at the LLZO|LCO interface. It has been shown that the interlayers prevent the undesirable diffusion of Co/La cations intermixing at the interface, confirming previous theoretical predictions. As an outcome, all interlayers exhibit higher specific discharge capacities - especially in the first cycles. Despite the initial improvement, the achieved first discharge capacities are still below the expected discharge capacity of 140 mAh g^{-1} for LCO. It can be concluded that there is still a resistive interphase between LCO and LLZO, which restricts the movement of Li^+ charge carriers at the interface.

The presence of an interlayer, however, does not prevent degradation during cycling, as there is still a significant decrease in capacity. This effect is ascribed to the volume expansion and contraction of the cathode active materials. Due to the compositional change during charge/discharge, which continuously induces stress at the interface between LLZO and LCO, micro-gaps are formed at the interface, leading to contact loss. Electrochemically induced cation diffusion and the resulting electrolytic oxidation can also lead to cell degradation. These effects are particularly evident in thin cathode films, where the influence of deleterious intermediate phases is more pronounced than in bulk cathodes.

An interlayer is essential for cathode co-sintering on LLZO electrolytes and highlights that the choice of interlayer significantly affects cell performance. Li-Nb-O is the most suitable and can substantially impact the fabrication of future ASSBs. To further isolate the underlying reaction mechanisms, additional studies are needed. These may include *operando* or *post-mortem* analysis.

3.3 Voltage drop phenomenon upon discharge: An electrochemical study

In the previous section, an unusual drop called a "kink" was observed in CV scans and during galvanostatic charging, specifically in the Li-Nb-O system. Similar voltage drops, e.g. "kinks", during discharge have been reported in the literature, but none of them have gone into a detailed explanation of the problem. Figure 3.11 gives an overview of published voltage drops found in the literature.
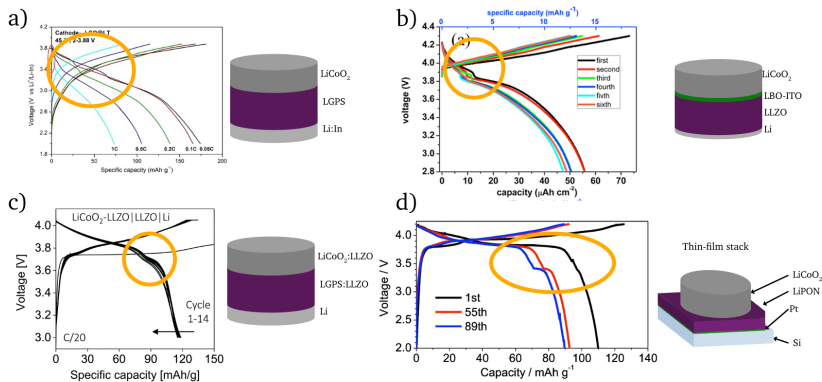
Figure 3.11. Overview of similar voltage drops reported in literature and the tested structures by a) Wang et al. [176], b) Liu et al. [170], c) Kim & Rupp [177], and d) Yamamoto et al. [178]. Voltage drops are highlighted by the yellow spot.

Wang et al. [176] observed asymmetric cycling behavior for modified LCO, as shown in Figure 3.11a. They did not provide a detailed description of the sudden drop in potential. They hinted at it in their differential capacity

analysis, suggesting that it corresponds to a phase transition between ordered and disordered lithium ion arrangements within the CoO_2 framework, specifically denoted as "*peak pairs at higher voltages (peak 2 and 2', peak 3 and 3') corresponding to the phase transition between ordered and disordered lithium ion arrangements in the CoO_2 framework*".

Liu et al. [170] studied interfacial resistances in LLZO electrolytes and also found a sudden drop in potential. Figure 3.11b of their study shows the charge-discharge curves of their LCO-based cells, which show a similar asymmetric cycling behavior. They mentioned "*a voltage plummeting was observed in the discharge process between 3.9 and 3.8 V, leading to a very small charge/discharge capacity*"

Kim & Rupp [177] focus on the development of an all-ceramic cathode composite aimed at achieving low interfacial resistance. Figure 3.11c details their investigation and fabrication of $LiCoO_2$-based composite cathodes designed for all-oxide Li-garnet solid-state batteries. One observed feature in their work is the presence of asymmetric cycling behavior. During the discharge process, there is a drop in potential.

Yamamoto et al. [178] explored anode-free thin film ASSB. Figure 3.11d of their study shows the charge-discharge curves of their LCO-based cells, which exhibit similar asymmetric cycling behavior. They attribute the observed voltage drop and plateau to the lithiation of their Pt current collector. However, they do not explain why it is not visible in the first discharge cycle, nor why it is not a symmetric behavior as observed in Chapter 4 of this Thesis.

3.3.1 Results and discussion

In an attempt to further investigate and isolate the possible causes, additional cells were fabricated with no interlayer, and the LCO cathode thickness was increased to 600 nm.

Electrochemical characteristics of full cells

Figure 3.12 shows the cyclic voltammetry scans of full cells in the following architecture: Au/LCO/LLZO/Li metal. The scan rate was set to 0.1 mV s^{-1}. A prominent cathodic peak occurs at approximately 3.9 V vs. Li/Li$^+$, consistent with the primary delithiation plateau of LiCoO$_2$ [165, 166]. The anodic peak appears at a lower potential of about 3.7 V vs. Li/Li$^+$, close to the lithiation plateau of LiCoO$_2$. The lithiation response is much broader than the delithiation response. After the 3.7 V peak, there is a sharp decrease in current towards reduced anodic currents.
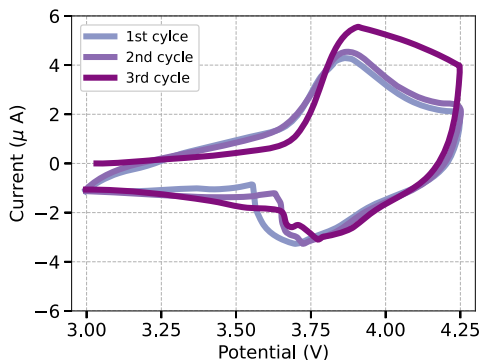
Figure 3.12. Cyclic voltammetry scans measured with a sampling rate of 0.1 mV s^{-1} between 3 and 4.25 V vs. Li/Li$^+$ without interlayer

Figure 3.13 shows the charge and discharge profiles of a battery stack cycled 11 times at a current density of 1.75 µA cm^{-2} (C/20) after cyclic voltammetry scans. Similar to these results, Figure 3.14 presents the galvanostatic charge-discharge curves for the kinked cell at various C-rates. As seen at C/20, a notable voltage drop is observed at both C/10 and C/5 rates. The charging phase shows a voltage "plateau" around 3.9 V vs. Li/Li$^+$, marking the delithiation processes of LiCoO$_2$. The discharge phase shows notable voltage drops between 3.8 and 3.5 V. This behavior mirrors the results from the first part of the Chapter. Starting with a discharge capacity of about 70 mAh g^{-1} in the first cycle, there is a gradual decrease in subsequent cycles, probably due to interphase formation and degradation. What differentiates this cell from the first part is its improved discharge capacity. This improvement may be due to the increased cathode thickness in this experiment. With a more substantial cathode layer of 600 nm, the influence of interfacial mixing may be reduced as its relative size to the thick film is reduced. This is in contrast to the previous experiments with thinner 300 nm LCO films. Of particular interest is again the asymmetric behavior observed between charge and discharge, with voltage drops occurring only during the discharge phase.

Differential capacity analysis is a widely used method to characterize batteries by identifying peaks corresponding to active material phase transformations during galvanostatic charge-discharge experiments. This allows phase transitions to be clearly visualized and degradation caused by a variety of mechanisms to be identified. In the differential capacity plot shown in Figure 3.15, a consistent redox peak is observed for both charging and
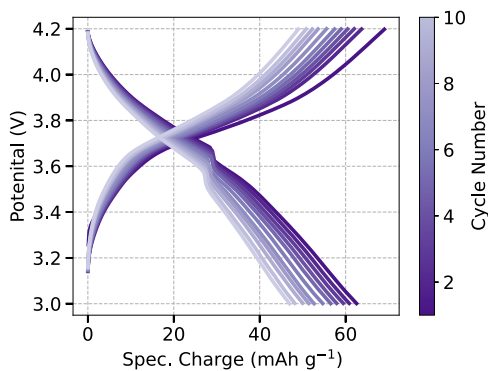
Figure 3.13. Galvanostatic charge and discharge profiles of a battery stack without interlayer at 1.75 μA cm^2 between 3 and 4.2 V at 80 °C
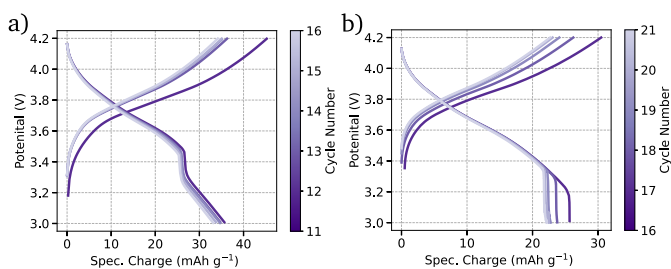
Figure 3.14. Different C-rates for galvanostatic charging. a) Cycled at 3.5 μA cm^{-2} (C/10) and b) at 7 μA cm^{-2} (C/5)

discharging at a potential of 3.85 V vs. Li/Li$^+$. During charging, while the position of the peak remains stable, its height shows a decreasing trend over cycles. This decrease in peak height at a relatively constant voltage may indicate a loss of active material, such as electrode decomposition, or factors such as crystal structure disorder [179]. This decline is also reflected in the gradual decrease in discharge capacity over cycles. On the discharge side, the primary peak not only decreases in height but also shifts to lower

voltages. Such a shift, coupled with the decrease in height, can be attributed to mechanisms such as lithium loss or electrolyte decomposition/oxidation [180]. During the charging phase, a shoulder is observed around the 3.3 V range, which is not visible in the galvanostatic charge-discharge experiments. In the first cycle, this shoulder is clearly defined, but its profile fades in subsequent cycles, indicating a different behavior that is not seen in the discharge phase. In addition, there is a distinct secondary peak around 3.6 V in the discharge, which probably reflects the voltage drop in the discharge curves. This peak undergoes a more pronounced shift to lower potentials as the cycles progress.
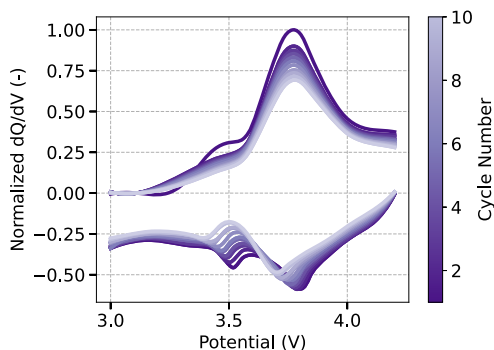
Figure 3.15. Differential capacity analysis (dQ/dV vs. V) for full cells between 3 and 4.2 V at 80 °C

Electrochemical impedance spectroscopy of full cells

Electrochemical impedance spectroscopy was performed to further investigate the sudden voltage drop and to understand whether electrode or electrolyte decomposition was causing this effect. The detailed test proce-

dure can be found in the Methods section. Figure 3.16 show electrochemical impedance spectroscopy plots of the tested battery stack during charge (a, c) and discharge (b, d) cycles. The top panels are Nyquist plots, and the bottom panels are Bode plots showing magnitude and phase angle. The color gradient indicates the change in battery potential from 3 to 4.2 V vs. Li/Li^+.

During the charging cycle, the impedance remains constant over the potential range of 3V to 4.2V vs. Li/Li^+, consistent with the behavior of stable electrode-electrolyte interfaces. A closer examination of the Bode plots reveals that the magnitude of the impedance increases at lower potentials. This change indicates increased resistance, possibly due to changes in the cathode active material. At these potentials, the behavior of the battery stack becomes more diffusive, manifesting itself at higher frequencies. This observation may be due to reduced lithium-ion diffusion through the bulk of the cathode or its surface film [181].

During discharge, the impedance spectra from 3.7 to 4.2 V vs. Li/Li^+ closely resemble those of the charge phase, indicating a stable system. However, there is a deviation between 3.6 and 3.7 V. This increase in impedance magnitude could be related to sudden changes in the tested cell, perhaps due to relocations in the cathode structure or degradation at the electrode-electrolyte interface. The phase shift to lower frequencies indicates a transition in the behavior of the cathode to become more capacitive and accumulates charge at the interface. This transition could indicate adjustments in its charge storage mechanisms or the onset of resistive barriers that impede ion flow.

The capacitive behavior shows slight changes at high frequencies during the charging phase. These changes become more pronounced during the discharge phase. There is a distinct impedance gap that appears between 3.6 and 3.8 V during discharge. Beyond 3.8 V, the impedance spectra closely resemble those observed during charging. On the other hand, below 3.6 V vs. Li/Li$^+$, the impedance spectra, while retaining a similar shape to those at higher potentials, show significantly increased impedance values. At the transition from discharge to charge, there is a sharp and abrupt decrease in impedance values. This rapid change suggests either a reversible system behavior or a transient impedance phenomenon during the discharge phase that is subsequently dissipated during the charge phase.

Figure 3.17 shows the electrochemical impedance spectra for all three repetitions at a constant potential of 3.8 V vs. Li/Li$^+$ during charging. A a gradual increase in impedance at constant potentials is observed over several cycle. With each repetition, a subtle increase in impedance can be observed, which can be attributed to degradation processes in the battery.This increase is a common sign of degradation and reflects an obstruction to the movement of the Li-ions, resulting in higher impedance values.

To quantify the individual resistive and capacitive contributions, the equivalent circuit previously used by Zhang et al. [153] was again used as a model (see Section 3.2.1). Since all EIS measurements were performed at elevated temperatures (80 °C), there was a characteristic overlap of the contributions from the (R-CPE) components. Despite careful efforts in modeling and fitting the data sets, the results, unfortunately, did not provide any new insights.
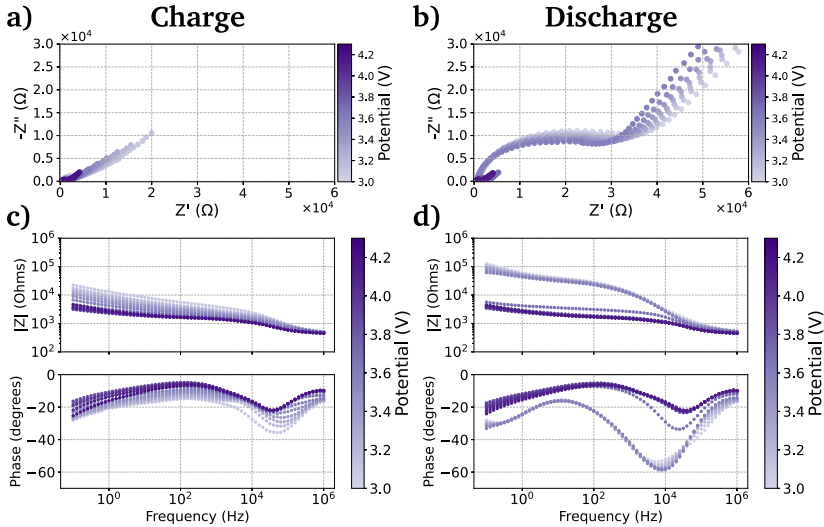
Figure 3.16. Electrochemical impedance spectroscopy plots of the tested battery stack during charge (a, c) and discharge (b, d) cycles. Top panels (a, b) display Nyquist plots where the real impedance (Z') is plotted against the imaginary impedance (-Z"). Bottom panels (c, d) represent Bode plots showcasing the magnitude of impedance (|Z|) and phase angle against frequency. The color gradient indicates the change in battery potential from 3 to 4.2 V.

This lack of clarity is primarily due to the lack of a recognizable pattern that would clearly attribute specific contributions to either the cathode, the interface, or other factors within the system. The fitting only confirms the finding that the impedance rises abruptly in the discharge cycle. Once the transition from discharge to charge begins, the impedance returns to its original values.
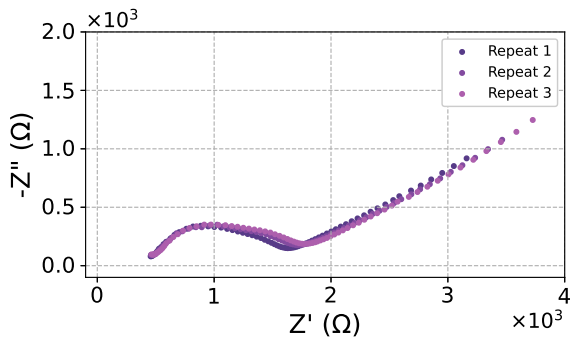
Figure 3.17. Electrochemical impedance spectra for various repeats at a constant potential at 3.8V during charge.

3.3.2   Hypotheses

In addition to a thorough literature review and extensive internal discussions, a valuable conversation within the battery community on LinkedIn (26,100 views, 116 reactions, 31 comments as of Dec. 20, 2023) was initiated as part of this research effort [182].

From this discussion, several hypotheses and insights emerged regarding the observed voltage drop during the discharge cycle of solid-state lithium batteries. Zhongchun Wang suggested that the voltage drop may be due to mass transport, specifically the movement of lithium metal atoms, rather than charge transport. This could be related to the formation of a porous lithium metal layer at the interface during discharge. On the other hand, Sai Siddhardha suggested that the problem may be related to the formation of the cathode-electrolyte interphase (CEI) and the subsequent development of voids within this interface.

Roy Marrache raised the possibility that the phenomenon could be related to the formation of the solid electrolyte interface and possible contact problems between the solid electrolyte and the electrodes. It was speculated that this effect may be more pronounced in the early cycles. Rodrigo Elizalde Segovia contributed to the discussion by suggesting that volume changes within the electrodes could cause inconsistent contact between the solid layers.

The discussion raised several hypotheses, including mass transport issues, interphase formation, volume changes, and contact issues as potential explanations for the observed voltage drop in the discharge cycle of solid-state lithium batteries. Despite the useful insights gained from external discussions, it remains challenging to reach a definitive conclusion. The following hypotheses are the most frequently considered, with an assessment of their likelihood based on the available data.

Void formation

In the context of lithium metal solid-state batteries, voids refer to the empty spaces that form at the interface between the lithium metal anode and the solid-state electrolyte [183]. These voids, similar to bubbles in a liquid, are generally created during the lithium stripping process [183]. They are the result of lithium vacancies accumulating at the interface that are not sufficiently refilled, causing the Li metal to separate from the solid-state electrolyte [184, 185]. The formation and growth of these voids are critical to battery performance and lifetime because they interfere with the efficient transfer of ions and electrons. This process can be influenced by factors

such as current density, capacity, and more. For example, at low current densities, larger critical void nuclei are formed that grow slowly, while at high current densities, numerous smaller nucleation sites are formed that accelerate contact loss [183]. As a result, the formation of voids leads to point contact, which increases the resistance in the system and causes a voltage drop according to the Ohm's law.

The observed voltage drop suggests an alternative mechanism rather than void formation. The observed potential profile differs from the expected pattern for void formation, which would typically show a sharp, continuous drop in potential followed by an exponential rise rather than being limited or quasi-stable. In addition, void formation typically leads to irreversible effects that become more prominent over time, which is not consistent with the findings. Our collaborators from Empa working with the same pellets and procedure of Li pressing on Li|LLZO interfaces operate at current densities about 50 times higher than those tested but do not report void formation [186–188]. Finally, the drops in the experiments occurred after a charge transfer of about 7.5 µAh cm^{-2}, which corresponds to the stripping of about 40 nm of dense Li, which is unlikely to lead to significant void formation. Furthermore, void formation is an irreversible process that does not correlate with the electrochemical data. Galvanostatic cycling and EIS spectra suggest reproducible behavior.

Participation of CEI/SEI/Interlayer in electrochemical reaction

Intermediate phases and their formation play a crucial role in electrochemical systems. Their primary function is to stabilize the system and

prevent further degradation. These interphases can either be introduced intentionally or form naturally during the initial battery cycles. One hypothesis is that one of these interphases - the cathode-electrolyte interphase (CEI), the solid electrolyte interphase (SEI), or the lithiated metal oxide interlayer - may actively participate in electrochemical reactions.

The experimental results question this hypothesis. First, if these components were truly electrochemically active species, one would expect to see a redox couple in the cyclic voltammetry (CV) scans but the absence of such a redox couple in the data is evident. The peak positions observed in the differential capacitance versus voltage (dQ/dV) analysis are also not consistent with the expected behavior of electrochemically active species.

Contaminated solid electrolyte surfaces are the result of a chemical reaction with H_2O and CO_2. This reaction leads to the development of a Li-ion resistive layer on the LLZO surface, consisting of compounds such as LiOH and Li_2CO_3. However, Li_2CO_3 is known to exhibit charge cycling activity at a higher potential than at the observed potential, suggesting its limited involvement in the system [189]. Furthermore, research has shown that Li_2CO_3 is primarily involved in the initial cycle [189].

In order to test the hypothesis that the Li-Nb-O compounds play a role in the electrochemical process, cells were intentionally fabricated without the interlayer. The results were consistently replicated, demonstrating that the presence of a lithium-containing metal oxide interlayer is not a prerequisite for the observed voltage drop. This supports the notion that the CEI, SEI, or another interlayer does not affect the electrochemical reactions in the specific battery configuration.

Cathode degradation

Side reactions between the cathode and electrolyte in batteries, such as electrolyte decomposition and solid electrode passivation, contribute to degradation and fatigue. This degradation includes changes within cathode materials and at their interfaces, caused by parasitic electronic and ionic defect formation [190]. Specifically, the dissolution of cobalt into the electrolyte results in elastic strains exceeding 0.1 % and micro-cracks in and among $LiCoO_2$ particles [191]. These micro-cracks increase internal resistance between the active material and the current collector, consequently diminishing the overall electrochemical performance of the cell.

While interfacial degradation contributes to the performance degradation of the system under study, it may not be the only factor at play. Evidence of degradation can be seen in the gradual decrease in specific charge capacity (Figure 3.13) over the life of the battery from 60 mAh g^{-1} to 45 mAh g^{-1} and the decreased peak intensity observed in the differential capacity analysis. These observations indicate a decreasing ability to efficiently store and discharge charge. At the same time, a gradual increase in impedance at constant potentials is observed over several cycles (see Figure 3.14). This increase is a common sign of degradation and reflects an obstruction to the movement of the Li-ions, resulting in higher impedance values.

The pattern revealed by the electrochemical impedance spectroscopy data challenges the assumption that degradation is the primary factor. If degradation were the sole factor, one would expect to see a continuous, incremental increase in EIS values over the life of the battery. Such a pattern would imply an ongoing deterioration of conditions within the battery, such

as the progressive formation of resistive layers or the gradual degradation of electrode materials.

Instead, an order of magnitude increase in impedance is observed as the battery transitions from the charge cycle to the discharge cycle. This impedance level experiences a significant drop, also by an order of magnitude, as the battery returns to the charge cycle. This fluctuation in impedance values - a significant increase followed by a corresponding decrease - contradicts the expected steady progression of degradation effects. The results suggest that while degradation certainly contributes to system performance, it is unlikely to be the sole or primary cause of the observed voltage drop.

Loss of contact LCO|LLZO interface

Active materials such as $LiCoO_2$ are prone to degradation over time [192]. This degradation is due not only to chemical instability, but also to volume changes in the active material, known as "breathing", that occur during the extraction and reinsertion of lithium ions [193]. Such unevenly distributed volume changes create stresses that can lead to mechanical failures such as intergranular cracking [194], separation of the active material (rendering it electrochemically inactive), and loss of contact at the interface. This loss of contact, similar to void formation, leads to point contact, increased resistance and a consequent voltage drop according to Ohm's law.

In their study, Barai et al. [126] used a mesoscale computational model to investigate delamination at the cathode|SSE interface. During the charging process, delithiation of the LCO results in volume expansion due to the negative molar partial volume of lithium. This volumetric expansion induces

compressive stresses at the cathode|SSE interface. The volumetric change does not lead to noticeable delamination, and only small microcracks are observed after charging. During discharge, some delamination occurs due to the negative size of the partial molar volume of lithium in LCO. This delamination affects the discharge capacity and increases the interfacial charge transfer resistance, especially during the first charge-discharge cycle.

In contrast, the empirical observations, which are still limited to a few micrometers, provide a different perspective. Figure 3.18 shows a *post-mortem* FIB-SEM micrograph of the kinked cell. The cross-sectional micrograph of the LCO|LLZO interface shows no significant delamination. The absence of strong delamination challenges the hypothesis that it is the primary cause of the voltage drop. This hypothesis also does not explain the observed variations in impedance magnitude between charge and discharge cycles. If contact loss due to delamination were a dominant factor, rapid and reversible changes in impedance would be unlikely. Taken together, these results suggest that while delamination may occur and affect battery performance, it is unlikely to be the primary cause of the observed voltage drop.

Phase transformation and surface reconstruction

Zhang & White [195] studied the formation of the monoclinic phase in LiCoO$_2$ during battery discharge, a key aspect of the intercalation process in this material. Initially, when lithium ions intercalate into LiCoO$_2$ (Li$_x$CoO$_2$), the reaction is primarily single phase for values of x ranging from 0.25 to 0.75. However, a shift occurs at approximately x $\approx$ 0.5, signaling the emergence of a monoclinic phase. This phase transition is a characteristic feature of LiCoO$_2$
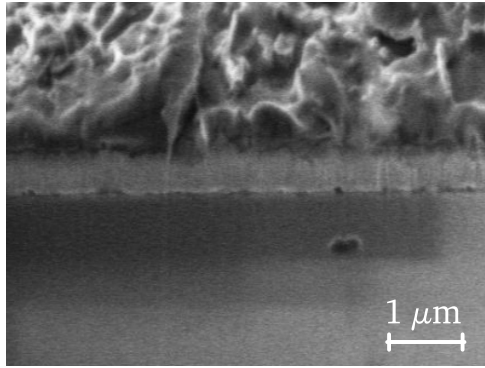
Figure 3.18. *Post-mortem* cross-sectional SEM micrograph of the cathode|solid-state electrolyte interface of a kinked cell

and is part of a stepwise phenomenon. As lithium intercalation progresses, a two-phase region appears around x = 0.75 and persists until x = 0.975 is reached, after which the electrode material reverts to a single phase.

The intercalation process within a $LiCoO_2$ particle during discharge involves several steps. Initially, there is diffusion within the α-phase, followed by a phase transition stage, culminating in a transition to a single β-phase. As lithium ions continue to intercalate, a β-phase shell begins to form around the Li-depleted α-phase core, resulting in the coexistence of two phases within the particle. The boundaries between these phases are dynamic and move toward the center of the particle as intercalation progresses. Translating this to the thin film LCO cathode, the cathode should first lithiate at the interface, forming a β-phase, while the top surface remains a Li-depleted α-phase. Thus, the movement of Li^+ ions in the immediate interface region is hindered, and a voltage drop could potentially occur. However, it is important to note that this process should exhibit symmetry and not asymmetry as

observed. An alternative explanation may lie in the concept of "slab gliding".

Li et al. [196] explore this concept in the context of $LiCoO_2$, providing insight into a structural transition mechanism that occurs during the charging and discharging processes. Understanding this mechanism is important to understand the phase transitions and electrochemical behavior of $LiCoO_2$.

To quantify the sliding motion of CoO_6 layers, a parameter known as the "gradual angle" (δ) was introduced. In the O3 phase of $LiCoO_2$, this angle is approximately 9.847°, corresponding to a specific stacking arrangement of Co ions (-$\alpha\beta\gamma\alpha\beta\gamma$-). During delithiation, the gradual angle decreases, indicating a structural transformation. The O3 phase transitions directly to the O1 phase during delithiation, although this transition is often obscured by the formation of Li-Co antisites and other intermediate phases, especially at high delithiation levels. The graduation angle varies during charge and discharge cycles.

For example, when $Li_{0.7}CoO_2$ is charged, the angle decreases to 9.572°, indicating distorted stacking of the Co columns. This change suggests that internal stresses are driving the sliding of the CoO_6 layers and the associated phase transitions. As the material is further charged, the angle continues to decrease, reaching 7.426° for $Li_{0.5}CoO_2$ and finally approaching zero for $Li_{0.3}CoO_2$, indicating a transition to the O1 phase. Upon lithiation to $Li_{0.65}CoO_2$, the angle increases again, suggesting a partially reversible phase transition. The sliding of CoO_6 layers, especially at high delithiation levels, induces structural changes that are not fully reversible. This phenomenon contributes significantly to the electrochemical degradation of the battery. The transition from the initial layered structure to the rock salt phase is

a major factor in the observed capacity degradation and voltage drop in $LiCoO_2$.

The studies discussed focus on the structural transitions in $LiCoO_2$ during charging and discharging of batteries. They show that the sliding motion of the CoO_6 layers and the associated phase changes are crucial for the electrochemical behavior of the material. In particular, the angular fluctuations during these processes indicate a possible influence on the charge accumulation at the interface, which can lead to a potential drop. However, these observations should be interpreted with caution. Although slab sliding can explain some characteristics of the voltage drop, it is unlikely to be the cause.

3.3.3 Conclusions

A comprehensive investigation of the observed voltage drop was conducted. Through a combination of empirical observations and theoretical analysis, several hypotheses were carefully evaluated. The investigation focused primarily on understanding the dynamics occurring at the anode|SSE interface, the potential role of intermediate phases such as CEI/SEI/interlayer in electrochemical processes, interfacial degradation mechanisms, the possibility of delamination occurring at the cathode|SSE interface, and the impact of phase transformation in $LiCoO_2$.

The void formation hypothesis was thoroughly reviewed. The experimental data suggested an alternative mechanism for void formation. Discrepancies in the potential profiles and the absence of the expected irreversible effects indicated that void formation might not be the primary factor contributing to the observed potential drop.

Regarding the involvement of CEI/SEI/interlayers in electrochemical reactions, the analysis performed suggested that these interlayers did not affect the electrochemical behavior. This conclusion was supported by the absence of electrochemically active species in cyclic voltammetry scans and differential capacitance analysis.

While interfacial degradation was identified as a contributor to system performance degradation, it was not found to be the sole determining factor. Electrochemical impedance spectroscopy data revealed a more complex interplay of factors beyond simple degradation effects.

Investigation of the delamination hypothesis at the cathode|SSE interface

contradicted the notion of a delamination-induced voltage drop. The absence of detectable delamination at the LCO|LLZO interface suggested that other factors played a more important role in the observed voltage drop.

Finally, the study of phase transformation and "slab gliding" in $LiCoO_2$ provided additional insight into the structural transition mechanisms occurring during charge and discharge cycles. The importance of slab gliding in these transitions stressed the importance of structural changes in battery degradation and performance.

A definitive conclusion remains elusive. The most plausible hypotheses seem to revolve around delamination at the cathode|SSE interface or phase transformation.

Advanced techniques such as operando X-ray diffraction (XRD) or tomography could be used to further investigate the delamination and phase transformation/slab gliding hypotheses. However, the latter approach may not be feasible at this time, given the limitations of existing tomography measurements in the sub-micrometer range.

Table 3.1. Hypotheses and arguments for/against voltage drop

Hypothesis	Arguments For	Arguments Against
Void Formation	• The formation of voids leads to point contact, increased resistance and causes a voltage drop according to Ohm's law.	• Observed voltage profile differs from expected for void formation, as not exponentially and limited to few tenth mV • Void formation typically leads to irreversible effects, not seen in findings. • Experiments at higher CDs by other groups do not report void formation. • Stripping of 40 nm dense Li unlikely to cause significant voids. • Cannot explain the sudden drop in impedance back to low values.
Participation of CEI/SEI/Interlayer	• Interlayer or formed interphases could actively take part in electrochemical reactions.	• No redox couple seen in CV scans, contrary to expected behavior. • Differential capacitance analysis does not align with active species behavior. • Li_2CO_3 active at higher potential than observed, suggesting limited involvement. • Replicated results without lithiated metal oxide interlayer, implying its non-essential role. • Cannot explain the sudden drop in impedance back to low values.

Table 3.1 continued from previous page

Hypothesis	Arguments For	Arguments Against
Interfacial Degradation	• Side reactions between the cathode and electrolyte are a major contributor to degradation. • Strain leads to the development of micro-cracks within and between the Li-CoO$_2$ particles.	• EIS data shows impedance fluctuation between charge and discharge cycles, contradicting steady progression of degradation. • Significant impedance increase and decrease challenge the assumption of degradation as the primary factor. • Degradation contributes to performance, but not the sole cause of voltage drop.
Loss of Contact LCO	• Charging process causes delithiation of the LCO, which leads to volume expansion and results in compressive stresses at the cathode|solid-state electrolyte (SSE) interface. • During the discharge process, delamination can occur at the cathode/SSE interface and can lead to an increase in resistance.	• Empirical post-mortem FIB-SEM investigation did not show significant contact loss at the cathode|electrolyte interface. • Fluctuation in EIS data does not align with theory of contact loss.

Table 3.1 continued from previous page

Hypothesis	Arguments For	Arguments Against
Phase Transformation and Surface Reconstruction	• Formation of monoclinic phase, phase transition, and slab gliding in Li-CoO$_2$ show structural transitions during charge/discharge which lead to internal stress and impact the charge transfer kinetics.	• The transition to rock salt phase is a major factor in capacity degradation, but not conclusively the cause of voltage drop. • Slab sliding might explain some voltage drop characteristics, but it does not explain why we have the impedance variation.

4   ANODE | SOLID-STATE ELECTROLYTE INTERFACE

This chapter aims to compare the impact of different seed layers – gold, platinum, and amorphous carbon – on lithium plating and stripping in an anode-free thin-film configuration[1]. The seed layers are placed between the bare copper CC – since the early day being used as conventional current collectors on the anode side [198] – and the LiPON solid electrolyte. The resulting configurations were tested in half-cell structures, and the evolution of the overpotential and the relationship between lithium plating/stripping, nucleation kinetics, and alloying properties of each seed layer were analyzed.

The second part of this chapter aims to visualize lithium plating in anode-free batteries using optical microscopy techniques. The main goal is to develop cell configurations that allow direct visual observation of lithium deposition behavior. Such visual insights are critical for understanding

---

[1]There is an ongoing discussion in the academic community regarding the appropriate terminology for batteries designed without a traditional anode and initially fabricated in a discharged state. Terms such as 'anode-free,' 'anode-less,' 'Li-free,' and 'zero-excess lithium' have been used interchangeably. However, this Thesis will consistently use the term 'anode-free' for clarity and consistency, acknowledging the debate surrounding this nomenclature [197].

nucleation kinetics and alloy properties influenced by different nucleation layers.

*Parts of the content of this chapter were published in Müller et al. [199]: Müller, A.; Paravicini, L.; Morzy, J.; Krause, M.; Casella, J.; Osenciat, N.; Futscher, M. H.; Romanyuk, Y. E. Influence of Au, Pt, and C Seed Layers on Lithium Nucleation Dynamics for Anode-Free Solid-State Batteries. ACS Appl. Mater. Interfaces **16**, 695–703 (2024).*

Specific personal contributions to this Thesis chapter include conceptualization, methodology, formal analysis, investigation, data curation, writing - original draft, and visualization. Contributions were made in performing electrochemical tests, conceptualization, and revision.

4.1 Introduction

The introduction of a solid-state electrolyte also paves the way for replacing traditional graphite anodes with metallic lithium, resulting in 40 to 50 % higher energy density [13, 20, 200–202]. However, it presents challenges such as high reactivity, unstable interfaces, and lithium dendrite growth due to uneven plating and stripping [203]. These complications can lead to current focusing, dendrite formation during battery cycling, and potentially dangerous short circuits. Furthermore, lithium metal is highly reactive, and integration into a battery is only possible under an inert atmosphere, suggesting that the use of metallic lithium films in solid-state batteries may not be practical [204].

One potential strategy to overcome manufacturing issues and further increase energy density is to move away from lithium foils to anode-free solid-state batteries (AFSSBs) or a "zero lithium excess" manufacturing process [38]. Here, the battery is manufactured in the discharged state with a lithium-containing cathode and a bare anode-side current collector (CC) [205–208]. This concept not only increases the energy density by reducing the battery volume and weight but also reduces the handling and manufacturing complexity. The lithium metal anode is then formed electrochemically during the first charge cycle by electroplating the lithium present in the cathode. Therefore, mechanisms that control the nucleation and growth of lithium metal are crucial to the success of AFSSBs [209].

Figure 4.1a presents the fundamentals of lithium nucleation and growth based on classical nucleation theory. This theory states that solid phase

nucleation involves a free energy barrier due to the formation of a critical cluster of atoms. In electrodeposition, this nucleation barrier can be adjusted by changing the electrochemical supersaturation at the working electrode by modulating the overpotential. This can be achieved either by changing the current or by using seed layers to reduce the surface energy.

The driving forces in lithium plating are categorized into reaction, charge transfer, diffusion, and crystallization overpotentials. However, only two characteristic overpotentials are typically observed: (1) the nucleation over-potential (η_n), which is characterized by a voltage spike at the onset of Li plating, and (2) the overpotential plateau (η_p), which is observed after nucleation as Li growth continues, as shown in Figure 4.1b. Due to the nature of galvanostatic Li deposition, which occurs under variable conditions, η_n and η_p are selected for analysis because of their ease of extraction from experimental data and their importance in describing nucleation and growth. [210]

At the onset of galvanostatic Li plating, the working electrode potential drops to -η_n, which is sufficient to initiate Li nucleation. After initial nucleation, the overpotential increases to -η_p, which is still negative relative to Li/Li$^+$. This allows Li nuclei to continue to grow, since the energy barrier for adding a Li adatom to existing nuclei is lower than that for forming a stable cluster of Li atoms. [210]

Figure 4.1c illustrates the impact of solubility and alloying on the overpotential required for Li nucleation on different materials. Materials like Au or Ag require no overpotential, while those with low solubility, such as Al and Pt, show slight overpotential. Materials with negligible solubility like Cu,
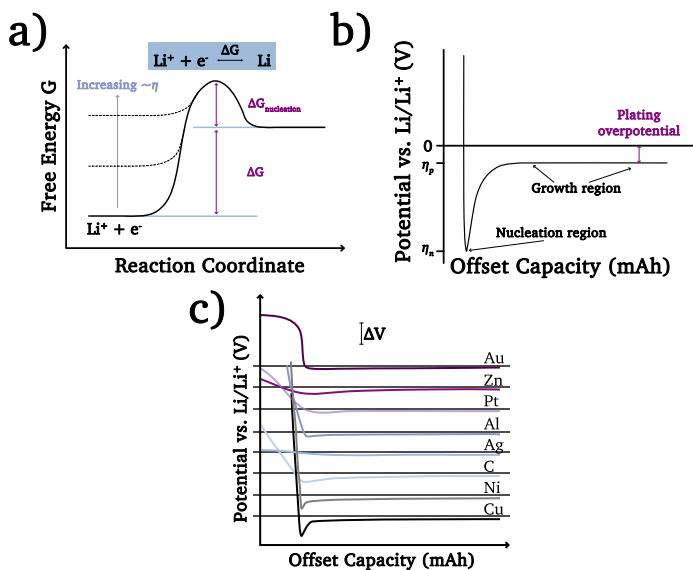
Figure 4.1. Fundamentals of lithium nucleation and early growth. a) Free energy scheme showing the effects of increasing overpotential on the nucleation energy barrier. b) Schematic representation of a typical voltage profile of galvanostatic Li plating with nucleation and growth region. c) Voltage profiles of various materials with some solubility and with negligible solubility in Li during Li deposition. The horizontal gray lines show 0 V vs. Li/Li$^+$. Adapted from Pei et al. [210] and Yan et al. [211].

Ni, C, and Si exhibit considerable overpotential. The distinct overpotential values for insoluble materials are due to their thermodynamic interactions with Li metal. [211]

While the concept of anode-free batteries had been previously demonstrated in traditional liquid systems [208, 210–213], its implementation in solid-state systems lagged behind. Early research on AFSSBs began with a study by Neudecker et al. [77] in 2000. This work involved the fabrication

of an anode-free thin film battery with a copper current collector, a lithium phosphorus oxynitride (LiPON) electrolyte, and a lithium cobalt oxide cathode using magnetron sputtering. The battery retained 80 % of its original capacity after 1000 cycles.

Later, research shifted the focus to an anode-free battery with a seed layer. A seed layer is a comparable thin layer deposited between the anodic current collector and the solid electrolyte. It provides nucleation sites for lithium metal growth and can improve battery performance and stability [38]. This direction was notably advanced by Lee et al. [100] at Samsung in 2020. Their research demonstrated an AFSSB with a silver-carbon nanocomposite layer and a sulfide electrolyte, achieving more than 1000 cycles and an energy density of more than 900 Wh l^{-1}. The study of Feng et al. [214] demonstrated the effectiveness of carbon seed layers in improving the air stability of LLZO when deposited on a garnet-based electrolyte, thereby reducing the area-specific resistance of the Li/LLZO interface. Building on this, Futscher et al. [215] explored the use of amorphous carbon seed layers. These layers facilitated uniform lithium plating, effectively prevented dendrite formation, and increased the critical current density to 8 mA cm^{-2} (Figure 4.2).

Besides carbon interlayers and mixtures of carbon composites, noble metals such as platinum and gold seed layers have also been explored. Studies on platinum [216, 217] revealed the effects of lithium plating and stripping reactions with platinum current collectors on LiPON, increasing the lithium nucleation number density compared to copper CC. Microscopic observations provided insights into the interactions between platinum and
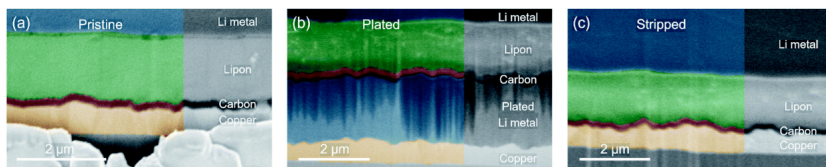
Figure 4.2. Cross-sectional SEM micrographs of a carbon interlayer at the current collector-solid electrolyte interface. a) After fabrication, b) after plating an equivalent Li thickness of 1 µm, and c) after subsequent stripping the plated Li. The thickness of the amorphous carbon layer is 100 nm deposited at 250 °C. Plating and stripping of Li was performed at a current density of 0.2 mA cm^{-2} [215].

lithium. Recent studies of gold seed layers [98, 218–222] have shown their role in improving the efficiency and lifetime of AFSSBs. The work of Krauskopf et al. [221] has investigated the effects of morphological instability of lithium metal anodes in the presence of gold seed layers. They have shown that the use of a lithium-alloying gold layer delays the penetration of lithium metal into the garnet electrolyte, and penetration occurs only after the alloy phases are fully formed. This line of research was further explored by Kim et al. [222], who demonstrated effective regulation of lithium distribution on LLZO by modifying the surface with an interlayer. It was proposed that the seed interlayer serves two main functions during battery operation: it acts as a dynamic buffer for the redistribution of lithium and as a matrix layer for facile lithium precipitation.

4.2 Influence of seed layers for anode-free solid-state batteries

4.2.1 Results and discussion

Thin-film stacks were fabricated to study different seed layer materials in the following architecture: Cu/seed layer/LiPON/Li/Cu, as shown in Figure 4.3a, and compared to the reference architecture: Cu/LiPON/Li/Cu. The evaporation of individual areas (1 mm diameter dots) of the lithium reservoir as separate cells was enabled through the use of shadow masks (Figure 4.3b). Alternative stacking such as Cu/Li/LiPON/In:Li were investigated but found to be ineffective. The lack of success in these reverse stacks was attributed to their rough surface textures, which prevented LiPON from forming a uniform, defect-free coating. Without a defect-free coverage the cells short. The LiPON solid electrolyte was chosen due to its successful track record in facilitating reversible cycling of lithium in AFSSBs, especially when combined with copper as a current collector [77]. The amorphous nature of LiPON isolates the surface morphology and chemistry from other potential obstacles, such as the presence of grain boundaries – a notable advantage over crystalline electrolytes such as LLZO [223]. In addition, LiPON's ability to form a thin yet stable passivation layer with the lithium metal helps reduce lithium loss during subsequent cycling [119, 224].

Gold, platinum, and amorphous carbon were chosen as seed layer materials. A 10 nm thick layer of gold was deposited by thermal evaporation.
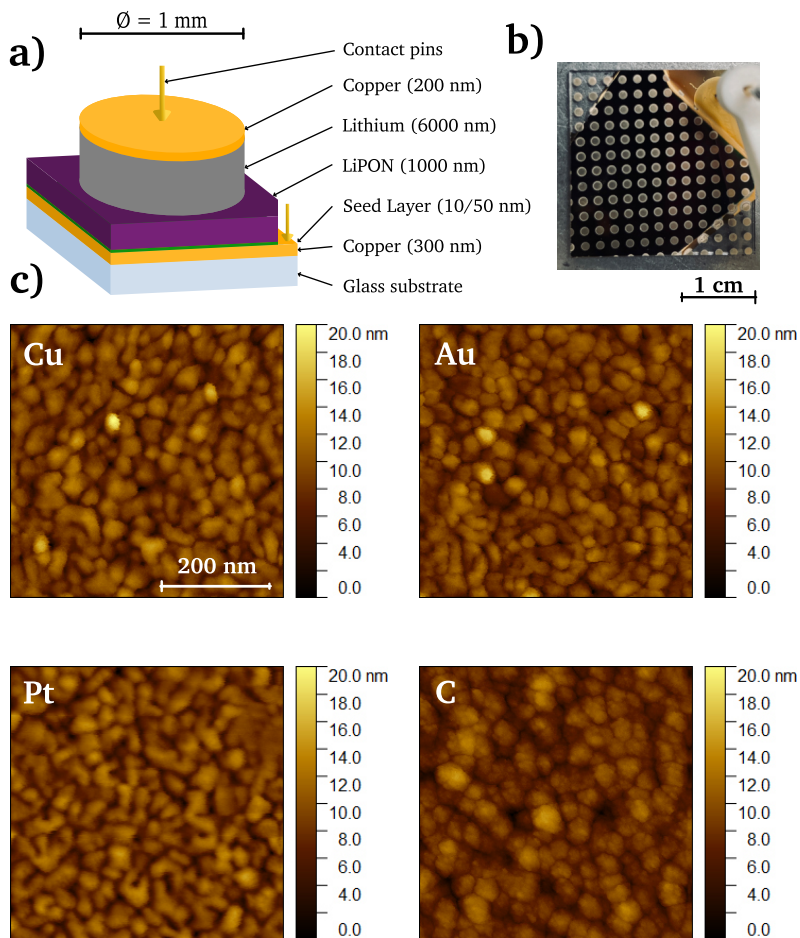
Figure 4.3. (a) Schematic illustration of the device configuration: Cu/Seed layer/LiPON/Li/Cu. (b) Photograph showing separate lithium reservoirs (1 mm diameter) for distinct cells. (c) AFM micrographs of bare copper CC, gold, platinum, and amorphous carbon seed layers. The scale bar is the same for all micrographs.

Platinum and carbon layers were deposited by RF magnetron sputtering to achieve thicknesses of 10 nm for platinum and 50 nm for carbon. Initial tests showed that the 10 nm gold layer in the thin film battery showed superior cycling performance compared to thicker layers (100 nm gold layer. The comparatively poor performance of thicker films compared to thinner films is due to the longer lithium diffusion length. This results in greater internal stress during lithium insertion/extraction [32]. Amorphous carbon, on the other hand, was previously shown to perform best at a thickness of 50 nm [215].

The AFM images shown in Figure 4.3c reveal comparable surface morphologies for all seed layers. All materials exhibit a smooth texture with an RMS roughness of 2.2 nm ± 0.1 nm. There are no significant morphological differences between the different seed layers. All deposited films are considered to be polycrystalline. For a complete overview, see Table A.4. Therefore, it is unlikely that the morphological characteristics of the seed layers, have an influence on the lithium plating and stripping processes. As a result, observed disparities can be attributed to differences in electrochemical processes and physicochemical properties such as interfacial energies, alloying energies, etc.

Experiments involving plating and stripping of a dense lithium metal layer were conducted. In the study, the terms „plating and stripping" in the context of thin film anode-free half cells refer to the process of galvanostatic charging and discharging. This involves the application of a constant current, which is essential to manage plating and stripping of lithium. Constant current conditions were set for a certain duration to obtain a lithium layer of

250 nm or 1 µm, depending on the experiment. Furthermore, the potential limits were set to 1.5 V vs. Li/Li$^+$ to prevent excessive degradation of the LiPON solid-electrolyte layer.

Figure 4.4a presents the representative voltage profiles for a bare copper CC and different seed materials (Figure 4.4b-d). Lithium metal of 0.2 mAh cm^{-2} was plated, corresponding to a thickness of 1 µm of dense lithium, using a current density of 0.2 mA cm^{-2}. Upon application of current to the bare copper CC, the voltage exhibited a sharp decrease below 0 V vs. Li/Li$^+$, reaching a nucleation potential at -225 mV. This pattern, characterized by a rapid voltage drop followed by a flat voltage plateau at -20 mV, aligns with predictions from the nucleation and growth theory [210].

Unlike copper, gold and platinum have unique interaction mechanisms with lithium. The gold layer interacts with lithium to form Li$_x$-Au alloy phases and has a specific solubility range in lithium metal [211]. Thus, lithium alloys with gold, forming a saturated phase prior to the formation of pure lithium metal. Similarly, the platinum layer, with its distinct solubility properties, provides a range of potential nucleation sites [225]. The lithium metal plating process on gold and platinum nucleation layers is characterized by two separate potential plateaus, followed by a potential drop that signals the start of lithium plating. The plating potential for these processes reaches its minimum at approximately -30 mV. This reduced nucleation potential is attributed to the identical crystal structures of pure lithium metal (βLi) and the solid solution surface layer, which effectively reduce nucleation barriers [211].

Lithium plating in the presence of amorphous carbon seed layers shows

Figure 4.4. Effect of seed layers on lithium metal plating and stripping during the first cycle at a current density of 0.2 mA cm^{-2} and an offset capacity of 0.2 mAh cm^{-2}. Distinct voltage profiles were observed during lithium plating and stripping for a bare copper current collector (a) and different seed layer materials of gold, platinum, and amorphous carbon (b)-(d). Au and Pt show alloying behavior, and C shows lithium intercalation behavior. Areas highlighted in yellow indicate lithium loss in the first cycle. The inset shows zoomed data highlighting different lithiation behaviors.

a markedly different voltage profile – it shows a slower decrease in potential. Amorphous carbon films sputtered at room temperature show a low sp2/sp3 ratio compared to depositions by high temperature sputtering derived from the G and D band. The high ratio of the G band corresponds to the stretching vibration of adjacent sp2-bound carbon atoms in both rings and chains and can be accounted for the electrochemical behaviour. The observed voltage decline corresponds to the initial lithiation of the carbon seed layer, indicating an intercalation behavior similar to graphite due to the sp2 hybridisation. In fact, amorphous carbon seed layers can host up to 200 mAh g^{-1} between 5 mV and 1 V vs. Li/Li$^+$ [226]. The drop is followed by a potential minimum at -55 mV before cells with carbon seed layer also reach a constant voltage plateau. Despite these differences, a consistent observation at low current densities across the materials is the emergence of a flat voltage plateau at about -20 mV.

Irreversible capacity loss in the first cycle also varies between seed materials and is highlighted by the yellow areas (Figure 4.4). While almost no loss ($\approx$ 1 µAh cm^{-2}) is observed for the bare copper CC reference, alloying materials such as gold and platinum show the greatest losses. Gold has the highest lithium loss with a peak value of 13 µAh cm^{-2}, corresponding to 65 nm of dense lithium metal, while platinum has a loss of about 6 µAh cm^{-2}. The greater lithium loss observed in gold during the first cycle could be attributed to the different reactivity of gold and platinum with lithium. Carbon shows the lowest irreversible lithium loss of the seed layers of about 4.5 µAh cm^{-2} in the first cycle. The coulombic efficiency reaches values close to 100 % in the subsequent cycles, which indicates passivation of the
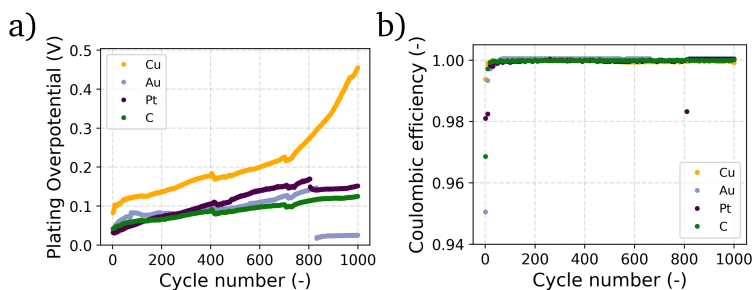
Figure 4.5. Long-term cycling. a) Plating overpotential and respective b) coulombic efficiency of tested cells over 1000 cycles at a current density of 2 mA cm^{-2} and a capacity of 0.1 mAh cm^{-2}.

Li loss source. This is further confirmed by long term cycling over 1000 cycles where the coulombic efficiency is close to 100 % over 1000 cycles (see Figure 4.5).

Figure 4.6 illustrates the dynamics of Li metal plating and stripping for a 100 nm gold seed layer during its first cycle. Similar to a thin gold layer, the lithiation plateaus are visible during (de)lithiation. The plating potential for this process also reaches a minimum at about -30 mV and a stable voltage plateau at about -20 mV. However, a pronounced 50 % loss of the initial Li deposition is evident, indicating inferior performance to thinner seed layers. We speculate that this nonlinear lithium loss is likely due to the formation of larger Li-Au clusters, with a greater area/volume ratio contributing to increased lithium loss.

To better understand the plated lithium morphology, the influence of various seed layers, and irreversible lithium loss, FIB-SEM analysis was conducted under cryogenic conditions. Figure 4.7 shows cross-sectional micrographs of the reference cell with bare copper CC and cells with gold,
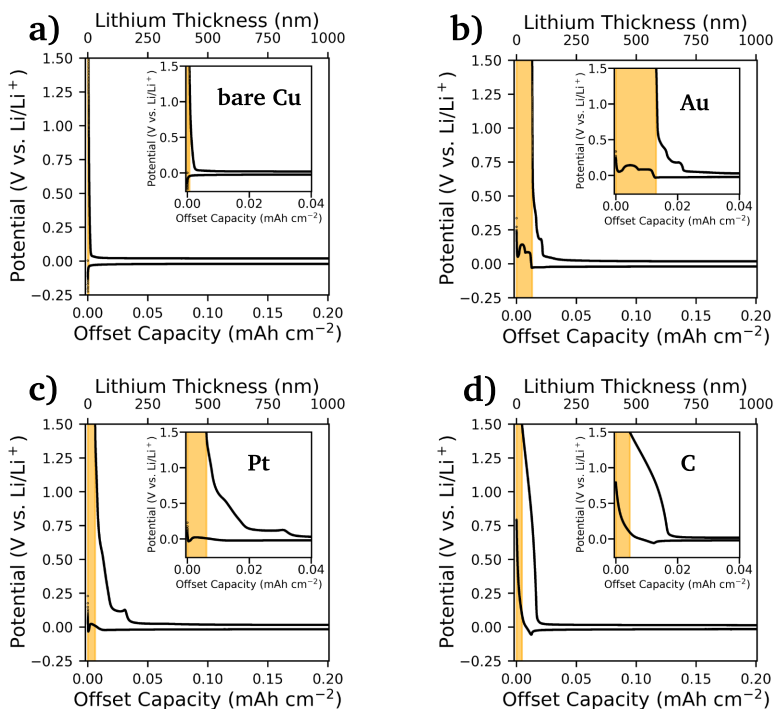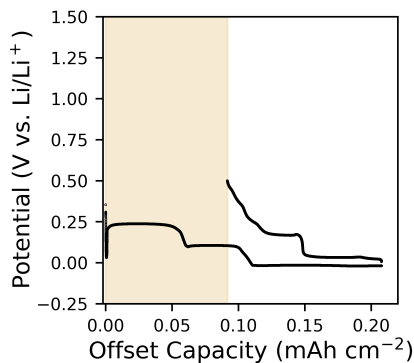
Figure 4.6. Effect on Li metal plating and stripping during first cycle at a current density of 0.2 mA cm^{-2} and a capacity of 0.2 mAh cm^{-2} for 100 nm Au seed layer.

platinum, and amorphous carbon seed layers. Each cell has 0.2 mAh cm^{-2} of lithium metal electrochemically plated during the first cycle, which equals 1 µm of dense lithium metal.

In the copper reference cell (see Figure 4.7a), two large cracks are observed in the CC. These cracks can be attributed to the non-uniform deposition of lithium, which exerts mechanical forces on the copper CC, ultimately leading to its failure. This failure mechanism is a common problem in thin-film batteries, as investigated in the study of Motoyama et al. [227]. The formation of cracks in the copper CC creates energetically favorable sites for lithium nucleation. This phenomenon may also explain the observed penetration and deposition of lithium beneath the copper CC, leading to the development of gaps between the substrate and the CC. Similar cracks were detected on several other cells with bare copper CC, both from the same substrate and from different batches. Additional cross-sectional SEM images
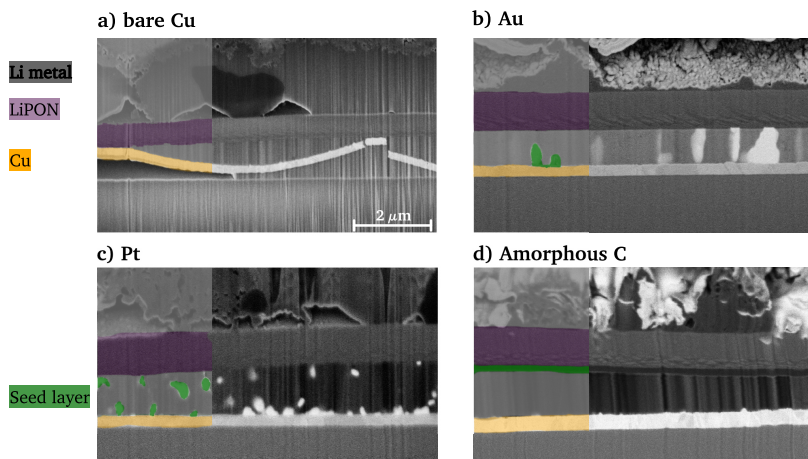
Figure 4.7. Cross-sectional SEM micrographs of the current collector-solid electrolyte interface with 0.2 mAh cm^{-2} (1 µm) plated lithium for (a) bare copper current collector and with (b)-(d) gold, platinum, and amorphous carbon seed layers after the first cycle. The scale bar is the same for all micrographs. All micrographs were taken in backscattered electron mode.

of these cracks and various cells are provided in the Appendix A.3.

Figure 4.7b-d shows cross-sectional micrographs for cells with seed layer. The introduction of seeding layers appears to facilitate more uniform lithium deposition, which in turn reduces the mechanical stress on the CC as no cracks are observed. The gold seed layer cell contains brighter particles with sizes on the order of 1 µm within the plated lithium layer, which are likely Li-Au alloy clusters. Interestingly, the 10 nm thin gold seed layer agglomerates and forms such clusters instead of remaining in the form of a uniformly thin alloy layer. Inaoka et al. [228] reported similar behavior at the Li/Li$_3$PS$_4$ interface, where the gold agglomerates into clusters. The platinum seed layer, which also forms an alloy with lithium, shows a more

uniform distribution of similar but smaller clusters in the lithium metal layer. In contrast, the amorphous carbon seed layer maintains its integrity. The lithium passes through the carbon layer similarly as in the previous work [215] and facilitates the formation of a dense and uniform lithium metal layer between the current collector and carbon interlayer.

High irreversible lithium losses in the first cycle for alloying materials, particularly gold and platinum, were observed, which may be related to the cluster structures. Initially, gold and platinum seed layers spread uniformly over the bare copper CC (Figure 4.3). However, during plating, these seed layers agglomerate and form alloy clusters within the lithium layer. It is speculated that only surface lithium is removed, with the remainder being "trapped" inside, possibly explaining the reduced lithium loss in platinum due to its smaller area/volume ratio. In addition, carbon cells show higher irreversible capacity loss than for the reference copper CC, possibly related to the formation of a Li-containing interphase (lighter contrast) seen in FIB-SEM micrographs at the lithium-carbon interface (see Figure 4.8) [229].

To investigate the effect of varying current densities for lithium plating and stripping, cells were cycled at current densities ranging from 0.2 to 8 mA cm^{-2} in increments of 0.2 mA cm^{-2}, as shown in Figure 4.9. Each current density increment was repeated five times and maintained for a time corresponding to an offset capacity of 0.05 mAh cm^{-2}, equivalent to plating 250 nm of dense lithium metal.

Figure 4.9a shows the behavior of the reference sample with a bare CC. As the current density increases, there is a corresponding increase in potential. It is noteworthy that the half-cells do not exhibit a critical current density
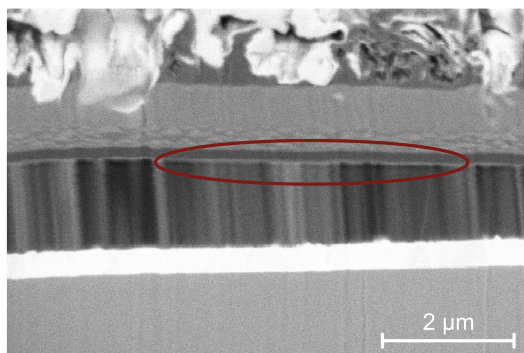
Figure 4.8. Cross-sectional FIB-SEM micrographs depicting the interface between the plated lithium and the carbon layer in magnified view.

even at the upper limit of 8 mA cm^{-2}. The critical current density is the maximum current that a cell can sustain before it shorts out. This behavior indicates inherent stability even at high current densities [230–232] and demonstrates the robustness of the thin-film system. The voltage profiles at 1 and 7 mA cm^{-2} are shown in the second and third columns of Figure 4.9. In the copper reference cell at 7 mA cm^{-2}, a stable plating plateau is observed at -750 mV. This plateau is consistent with the growth region identified in previous research by Pei et al. [210], and this stability is maintained at high current densities. In particular, the 250 nm lithium plating remains consistent, avoiding the exponential potential drops typically associated with void formation.

Figure 4.9b-d show the voltage profiles for cells with gold, platinum, and amorphous carbon seed layers. These cells, like the bare copper CC cells, do not reach a short circuit at the applied current density of 8 mA cm^{-2}
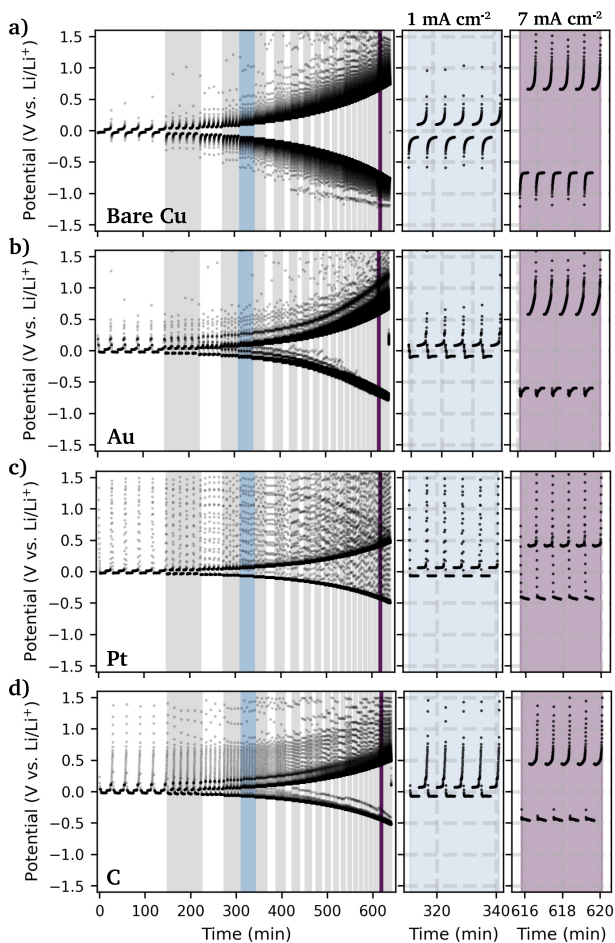
Figure 4.9. Effects of current density on lithium plating and stripping in thin-film cells for (a) bare copper CC, (b) gold, (c) platinum, and (d) amorphous carbon seed layer cells. Full data set in the first column cycled at current densities from 0.2 to 8 mA cm^{-2}. The regions differentiated by varying current densities are highlighted with gray shading. Each step represents an increment of 0.2 mA cm^{-2}. The second and third columns show the potential behavior at 1 mA cm^{-2} (blue) and 7 mA cm^{-2} (purple), respectively. Each density was repeated five times at an offset capacity of 0.05 mAh cm^{-2}, corresponding to 250 nm densely plated lithium.

during the plating of 250 nm dense lithium. For all seed materials tested, the lithiation plateaus are consistently observed during both the plating and stripping processes, even at higher current densities such as 1 and 7 mA cm^{-2}. A comparison of the bare copper CC with other seed layers reveals differences in their plating and stripping dynamics. The introduction of a thin gold seed layer improves stability, with its plateau stabilizing at -680 mV. This represents a reduction in overpotential of up to 10 % at the highest current density tested of 8 mA cm^{-2}. In contrast, the platinum and carbon seed layers establish their voltage plateaus at -520 mV and -490 mV, respectively.

In Figure 4.10, a current density evaluation of the 100 nm gold seed layer is shown. Persistent Li losses at every repeat are observed, peaking in an early short-circuit at approximately 4 mA cm^{-2} - a threshold significantly lower than that observed for 10 nm layers. We speculate that the early short circuit for cells with a 100 nm gold layer is correlated with the formation of bigger micro-sized clusters. Thicker layers start to agglomerate even more, leading to mechanical stress in the thin film stack. As a result, the LiPON electrolyte can crack or extensive current focusing can cause the formation of dendrite-like growth.

This study aimed to evaluate the overpotential development in the growth region across various materials. The overpotential for the tested seed layer materials and the reference was determined as follows:

First, electrochemical tests were performed on the discussed materials. The overpotential for each material was determined by averaging the growth region potential referenced in [210] and adjusting for ohmic losses. The plating potential was derived by averaging the growth region potentials of all
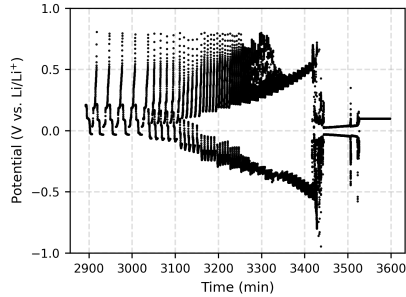
Figure 4.10. Effects of current density on Li plating and stripping in thin-film cells with 100 nm Au seed layer.

repeats and subtracting ohmic losses, calculated from the product of current density and system impedance.

The ohmic losses, primarily due to the electrical resistance of the solid electrolyte, were corrected with an impedance-based factor. This adjustment was applied to the potential calculation for each material. All cell electrolytes were sputtered simultaneously to ensure consistency.

The adjusted plating potential is expressed mathematically as

$$V_{plating} = |\overline{V_{plateau}}| - Z_{real}Aj \tag{4.1}$$

In this equation, $|V_{plateau}|$ [V] is the average potential in the growth region, Z_{real} [Ω] is the impedance of the system, A [cm^2] is the surface area, and j [A cm^{-2}] is the current density.

The nucleation region precedes the growth region and is characterized by the initial formation of lithium metal nuclei on the electrode. In this region, clusters of lithium atoms coalesce into larger particles. Factors such
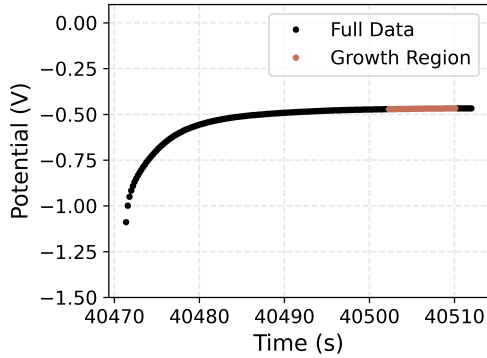
Figure 4.11. Plot of potential versus elapsed time. The entire data set is represented by black dots, while the specific subset representing the growth region of the data is highlighted by colored dots.

as voltage, current density and electrode structure affect these processes. The goal in this region is to achieve uniform, compact lithium deposition to prevent dendritic growth, which poses a risk of shorting the battery. The growth region is dynamic and changes during charging and discharging due to the continuous deposition and stripping of lithium metal.

Figure 4.12 provides the comparison of the evolution of the plating overpotential as a function of current density for all the seeds. The standard deviation between individual cells per seed layer does not exceed 10 %. To account for polarization effects due to electrolyte resistance, the potentials shown here have been adjusted accordingly.

A consistent linear trend of the increase in plating overpotential with increasing current density is observed for all seeds. The bare copper CC cell shows the steepest increase, reaching a peak overpotential of 325 mV at a current density of 8 mA cm^{-2}. The gold seed layer cell has a slightly lower
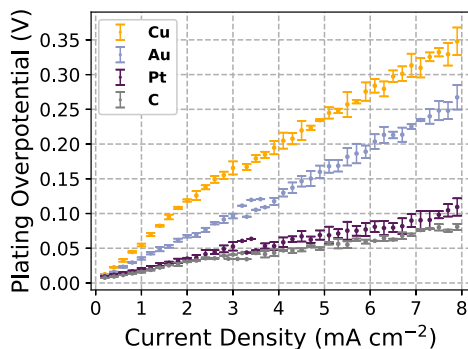
Figure 4.12. Plating overpotential response to current density for seed layers. The potentials presented here have been adjusted to account for polarization effects due to electrolyte resistance. The error bars show the standard deviation of the data from three individual cells.

rise in overpotential, reaching a maximum of 250 mV, while platinum and carbon have the lowest overpotentials of less than 100 mV at the highest current density measured.

The performance of carbon as a seed layer is characterized by a minimal increase in plating overpotential at higher current densities, reflecting stable electrochemical plating and hence less overpotential evolution. This stability is due to the intact amorphous carbon seed layer between the current collector and the solid electrolyte – as seen in Figure 4.7 – which ensures homogeneous plating, optimal current distribution, and minimized overpotential. It ensures uniform Li-ion diffusion, enhances surface reaction rates, inhibits lithium filament growth, and improves the reversibility of lithium plating. The results show that carbon and lithium-platinum alloys provide better performance in lithium plating/stripping and overall battery efficiency through overpotential

reduction compared to lithium-gold alloys. In addition, the promising results of two-component interlayers, namely silver/carbon [100] and gold/carbon [211], confirm these findings.

4.2.2 Conclusions

Anode-free half cells with seed layers composed of gold, platinum, or amorphous carbon being placed between the LiPON solid-state electrolyte and the bare copper CC were investigated. The formation of a dense lithium metal layer between the copper CC and LiPON, which could be repeatedly plated and stripped, was demonstrated. All cells withstood current densities up to 8 mA cm^{-2} without short-circuiting, demonstrating the reliability of the thin-film configuration. Gold and platinum seed layers alloyed with lithium early in the plating process facilitating uniform lithium metal plating on the current collector. As these layers agglomerate, they form alloy clusters distributed within the deposited lithium layer, preventing mechanical failure of the current collector. The amorphous carbon seed layer maintains its integrity and is characterized by a uniform, dense lithium metal layer between the current collector and the seed layer. Platinum and amorphous carbon cells exhibit the lowest overpotential evolution. Amorphous carbon has been found to be a viable and cost-effective alternative to noble metals as a seed layer material.

4.3 Optical microscopy visualization of lithium plating

A common problem in anode-free batteries, whether using liquid or solid electrolytes, is heterogeneous nucleation at the solid-electrolyte|current collector interface. This often results in the formation of isolated Li islands. Although initially small, these islands tend to grow in size and can adversely affect battery performance. These islands can reduce reversibility and potentially damage the current collectors and cell encapsulation. Achieving uniform coating and deposition of the Li metal electrode is critical and can be achieved by introducing seed layers.

Building on the previous section's investigation of seed layers in a 2D thin film model with ideally smooth interfaces, where amorphous carbon emerged as a promising seed layer, this study extends the investigation to rougher substrates such as LLZO pellets. A 3D microscopy setup was developed to visualize early Li nucleation between the solid electrolyte and the current collector during operation.

To address these challenges, recent studies have focused on understanding the evolution of Li island shapes in anode-free SSBs. Motoyama et al. [227] used a spherical pressure vessel model to relate the evolution of overpotential to the mechanical stresses in lithium as the islands impact thin-film metal current collectors on LiPON electrolytes. Wang et al. [185] studied a complete cell with an in-situ formed anode and modeled the adhesion work at the interfaces between Li, the electrolyte, and the current collector,

relating the overpotential to the minimum size of Li deposits and islands.

Synchrotron tomography techniques, increasingly used to study the morphological evolution of buried interfaces in SSBs, are complex and not feasible for routine application. The development of an *operando* platform by Kazyak et al. [233] using focus variation microscopy for 3D measurements of electrode morphology during formation presents a more practical approach. This platform allows a direct correlation between electrode morphology, electrochemical signatures, and mechanical stresses. However, there is no study visualizing the effect of seed layer *operando* on lithium nucleation.

In this study, the *operando* platform of Kazyak et al. [233] was adapted to investigate the effect of a seed layer on the in-situ formation of a lithium metal anode in LLZO electrolytes. Initial observations confirm the ability to monitor nucleation processes. It was found that a seed layer influences lithium plating and leads to a smoother plating behavior of the tested stacks.

4.3.1 Results and discussion

A similar setup was developed based on the shown *operando* platform for 3D visualization proposed by Kazyak et al. [233]. Figure 4.13 shows the schematic structure of such a platform, which was 3D printed in PLA as a prototype for testing purposes. The design was hermetically sealing the stack with O-rings. One promising configuration is the use of an LLZO pellet with a copper current collector on one side and a compressed lithium foil on the other. This arrangement has successfully facilitated the observation of the early stages of lithium deposition. As the current collector, a 5 µm thick copper current collector was sputtered on the LLZO substrate. Lithium

was pressed at 1000 kN onto the back side of the substrate. The bottom of the tested stack, a lithium reservoir with no other current collector, was contacted via a button cell spring. The applied pressure to the stacks was minimal yet adequate to maintain consistent contact during measurements. The top copper current collector of the *in-situ* formed anode was contacted using an ITO-coated glass substrate. By applying a current between the two contacts, the anode was formed *in-situ* using the lithium reservoir. Based on the previous results on the optimal performance of carbon as a seed layer, a 100 nm thin layer is deposited between the LLZO pellet and the copper CC.
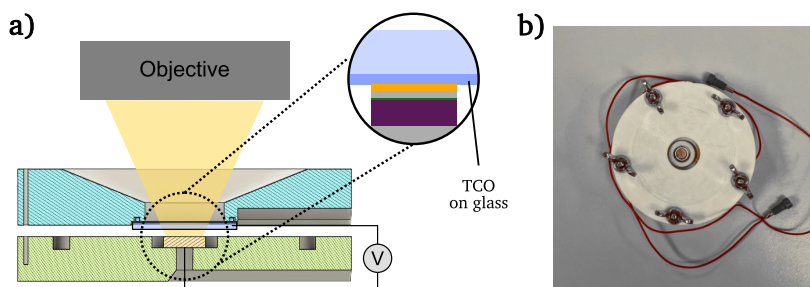
Figure 4.13. Schematic of optical visualization platform. a) Overview of the optical visualization platform and schematic of the cell setup, including the connection of the potentiostat, represented by "V". The top current collector is contacted with a TCO-coated glass. b) Photo of 3D printed prototype.

The voltage profiles of Li metal deposition on bare copper CC and battery stacks with a carbon seed layer are shown in 4.14. A dense lithium layer was deposited without subsequent stripping. Plating experiments were performed at room temperature without external pressure. A conservative current density of 0.2 mA cm^{-2} was used to avoid the early shorts commonly observed in LLZO-based systems.

It is evident that there is no distinct voltage dip observed at the onset of lithium metal deposition. However, there is a noticeable discrepancy in the voltage behavior between the bare copper battery stacks and those with a carbon seed layer. Specifically, the voltage drop for lithium plating in the presence of amorphous carbon seed layers mirrors the intercalation behavior identified in the previous chapter.

The voltage profile typically undergoes an initial rapid decline followed by a sustained voltage plateau, indicative of lithium layer growth. It is noteworthy that for the bare copper sample, the potential begins to show instability at approximately 0.8 mAh cm^{-2}, triggering a rapid decline. It eventually reaches the minimum potential (-8 V) achievable with the test equipment before reaching a plating capacity of 1 mAh cm^{-2}.

In comparison, the introduction of a carbon seed layer seems to improve the stability by maintaining a constant potential for a longer period of time. Only when the charge density reaches 0.9 mAh cm^{-2}, corresponding to a lithium layer thickness of 4.5 µm, a rapid potential drop is observed. Both drops can be attributed to the formation of voids in the lithium reservoir layer, resulting in a loss of electrical contact. Interestingly, the formation of voids occurs at an earlier stage in the pure copper reference sample, which can be attributed to inhomogeneous plating behavior. This irregularity in plating leads to an uneven distribution of current or ion flux, causing Li ions to be preferentially stripped from the counter electrode at specific points, ultimately resulting in void formation.

Figure 4.15 shows the EIS spectra obtained in the pristine state and after each 0.2 mAh cm^{-2} plating step for both bare copper CC and those coated
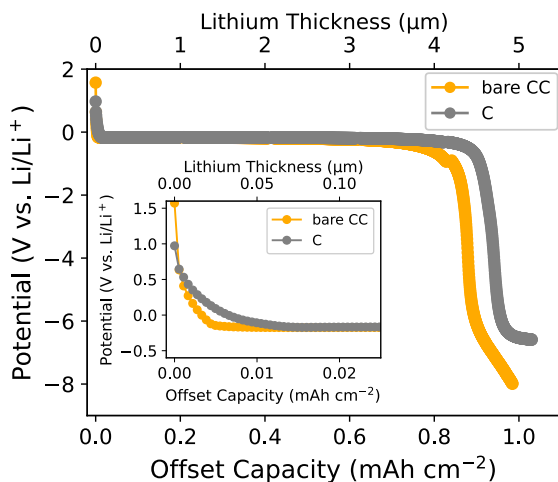
Figure 4.14. Lithium metal plating at a current density of 0.2 mA cm^{-2} and a total offset capacity of 1 mAh cm^{-2} at rough LLZO interface. Different voltage profiles were observed during lithium plating for a bare copper current collector and amorphous carbon. The inset shows zoomed data highlighting the different lithiation behaviors.

with a carbon layer.

In the pristine state, both stacks exhibit similar EIS spectra. A semicircular feature in the high-frequency region is attributed to the presence of the LLZO pellet. The ionic conductivity determined from the fitted data is approximately 10^{-5} S cm^{-1}. In the modified stack, an additional contribution appears in the mid-frequency range (1 kHz - 50 kHz). The low-frequency polarization is due to the ion-blocking behavior of the copper electrode [234].

Examination of the EIS measurement after the initial 0.2 mAh cm^{-2} plating step shows a clear shift in behavior. The low-frequency polarization

decreases, resulting in a new contribution in the mid-frequency range, a non-blocking behavior with a small low-frequency tail. This development is attributed to the presence of the plated lithium layer. The origin of the small low-frequency tail remains elusive. It is regularly observed at (alkali) metal-SSE interfaces and is probably due to diffusion processes of the metal at the interface [157, 233, 234]. As the plating process continues in increments of 0.2 mAh cm^{-2}, the impedance steadily increases, eventually exceeding an order of magnitude.

Comparing the performance of the bare copper CC stack with its carbon-modified counterpart, it is clear that the presence of the carbon seed layer has a moderating effect on the impedance rise. This is consistent with the previous cycling observations indicating that void formation begins prematurely in pure copper, driven by uneven flux distribution. Void formation ultimately leads to contact loss, as evidenced by increased impedance and potential drop.

To support electrochemical characterization techniques, the tested stacks were imaged from the top with an optical microscope after deposition of approximately 1 mAh cm^{-2}, which corresponds to a theoretical 5 µm thick homogeneous deposition over the entire current collector. Figure 4.16 shows top-view images taken with an optical microscope. In the case of the bare copper current collector (CC) stack, it is evident that the lithium plating results in the formation of two distinct hotspots. The occurrence of these hotspots can be attributed to irregular morphology, with lithium nucleation initiating at these localized sites due to the defect regions exhibiting faster Li deposition kinetics and higher nucleation tendency [235]. In contrast,
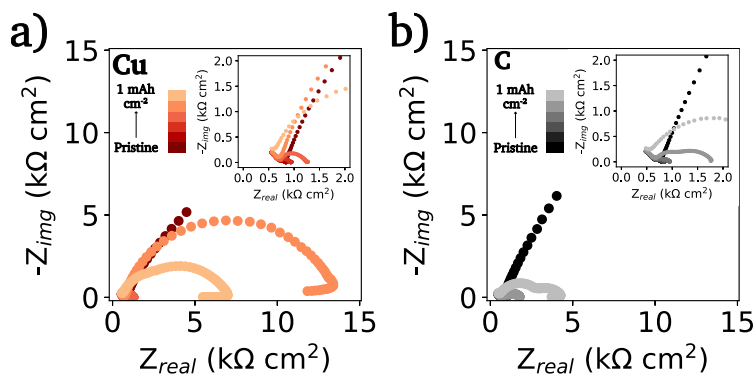
Figure 4.15. Electrochemical impedance spectroscopy spectra of the tested battery stacks during lithium plating. Spectra were acquired in the pristine state and after 0.2 mAh cm^{-2} plating steps between 1 MHz and 0.1 Hz.

when these observations are compared to the carbon-coated pellet, a more uniform distribution of lithium nuclei is observed. This is a clear indication of improved plating performance and more uniform current distribution.

4.3.2 Conclusions

Optical microscopy was used to investigate how seed layers affect the in-situ formation of a lithium metal anode in LLZO electrolytes, focusing on early lithium nucleation at the solid-electrolyte-current collector interface. This modified microscopy technique enabled lithium plating up to 1 mAh cm^{-2} and allowed direct observation of lithium nuclei through TCO-coated glass.

A carbon seed layer positively affects lithium plating. Unlike the bare current collector (CC) stack, which showed two distinct lithium clusters, the carbon seed layer allowed for more uniform lithium plating across the
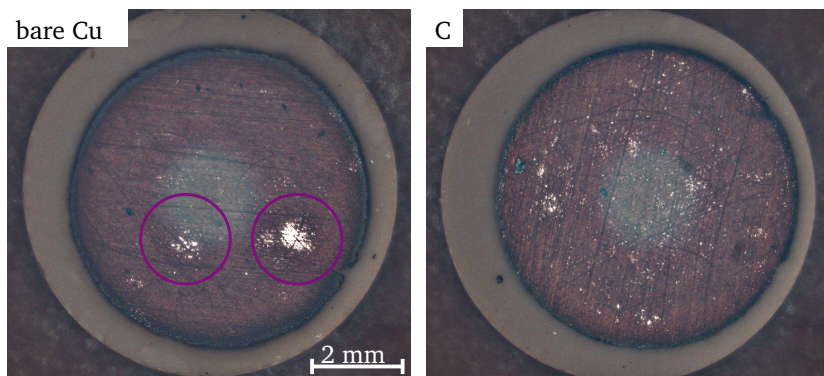
Figure 4.16. Influence of the seed layer on the morphology of the lithium layer. Optical RGB images of (a) bare copper current collector stack and (b) carbon-coated stack.

collector area.

Voltage profiles during lithium deposition indicated that the carbon seed layer resulted in more uniform plating and stability compared to bare copper, which showed early instability and void formation as early as 0.9 mAh cm^{-1}. Electrochemical impedance spectroscopy measurements corroborated these observations, indicating moderated impedance growth with the seed layer. Optical microscopy images revealed uneven lithium nucleation on bare copper, resulting in hotspots, while the carbon seed layer promoted a more uniform distribution of lithium nuclei, suggesting improved plating efficiency. These results highlight the importance of seed layers in improving lithium anode formation and addressing non-ideal interfaces.

5 CONCLUSIONS AND OUTLOOK

5.1 Conclusions

The aim of this Thesis was to enhance the interfacial stability of all-solid-state batteries by applying diffusion barriers and seed layers at the respective interfaces.

The investigation of various sputtered Li-Me-O (Me = Al, Nb, and Ti) interlayers revealed that metal selection plays an important role in mitigating cation interdiffusion at the interface, thereby improving the overall performance of solid-state batteries. The incorporation of lithiated niobium, aluminum, and titanium metal oxide interlayers as diffusion barriers reduced the Co/La cation mixing at the cathode|electrolyte interface, especially for cobalt diffusion. The presence of these interlayers improved the integrity of the cathode-electrolyte interface during high-temperature processes, thus promoting efficient Li-ion transfer. The study demonstrated a substantial reduction in interfacial impedance with the introduction of lithiated metal oxide interlayers. Specifically, the impedance was reduced from 8 kΩ cm^2 to 1 kΩ cm^2, indicating improved interfacial charge transfer efficiency. Full cells

with interlayers exhibited superior electrochemical performance compared to cells without interlayers. In particular, the Li-Nb-O interlayer proved to be the most effective, demonstrating a discharge capacity of 125 mAh g^{-1}. This high performance is attributed to its ability to suppress Co/La diffusion at the interface. As a result, the charge transfer resistance is reduced by avoiding the formation of detrimental interphases during sintering. Continuous degradation was observed during cycling, which was attributed to volume expansion and contraction of the cathode active materials, inducing stress at the interface. This study highlights the importance of interlayers in improving the performance and stability of battery interfaces, especially in the context of all-solid-state batteries.

A particularly interesting finding was the asymmetric voltage drop during discharging, also spotted in literature and the observed discharge-to-charge transition. This phenomenon, characterized by a sharp impedance drop, was consistently reproducible across different experimental setups. Despite extensive discussion within the battery community and numerous hypotheses, the exact reason for this phenomenon remains elusive.

The second part of the Thesis focused on the influence of different seed layers (Au, Pt, and C) on lithium plating and stripping in an anode-free thin-film battery setup. The introduction of seed layers was found to be effective in reducing overpotential and providing vital protection to the current collector. The collectors of thin-film cells without seed layers were prone to cracking during the first plating step. The cracking was actively suppressed by the introduction of seed layers, thus reducing the stress during nucleation while showing higher first cycle lithium losses of up to 13 µAh cm^{-2} (first cycle

efficiency of 93 %). Interestingly, the noble metal seed layers agglomerated during plating, forming micro-sized clusters in the lithium metal layer, while the carbon interlayer maintained its integrity. Among the materials tested, the carbon seed layer demonstrated remarkable effectiveness, reducing the plating potential from 300 mV for the bare copper current collector to 100 mV at 8 mA cm^{-2}. This result positions amorphous carbon as a viable, low-cost alternative to the more expensive precious metals traditionally used as seed layers. In addition, the use of a thin carbon seed layer not only benefits the anode-free thin-film concept but also appears to improve the performance of bulk batteries. With the introduction of a seed layer, the offset capacity was increased from 0.9 mAh cm^{-2} to 1 mAh cm^{-2}. This finding opens new avenues for the application of carbon-based materials in advanced battery designs.

In conclusion, this study makes contributions to the field of solid-state batteries, particularly in the area of interfacial stability. The results highlight the critical role of material selection and optimization in battery technology, with the Li-Nb-O interlayer demonstrating its effectiveness in mitigating cation diffusion and carbon seed layers showing promise in reducing overpotential. These results underscore the importance of interfacial engineering in improving the performance and durability of solid-state batteries.

5.2   Outlook

The key advantage of a thin-film model system is the simplified 2D arrangement of interfaces without the use of additives. Hence, the results of

this work can be applied to more complex systems since similar materials and combinations were used compared to bulk studies. However, it is important to note that bulk systems have significantly different layer thicknesses compared to the scope of our study. This, along with the presence of binders and electrode additives in bulk systems, may affect battery performance.

Despite their potential, thin-film batteries have not seen widespread adoption, primarily due to integration challenges and high cost. As of 2024, vacuum-processed thin-film batteries have achieved limited market success, primarily in niche applications. A notable limitation of these batteries is their modest capacity, which results from the limited charging of thin cathode layers. These layers, typically only a few micrometers thick, suffer from limited charging kinetics due to the lack of conductive additives.

A promising solution lies in a novel architectural concept of monolithic stacking of thin films, which allows the use of bipolar electrodes. This design minimizes substrate impact by stacking multiple cells and increases cathode surface loading by using multiple cathode layers. A thermoelectric model predicts that such stacked thin-film batteries could achieve specific energies greater than 250 Wh kg^{-1} at C-rates greater than 60. A simple proof-of-concept demonstrator with two stacks has been built, leading to a patent application (EP2218068.2, dated June 24, 2022, **co-inventor**) [81].

Scaling up production and, more importantly, electrode integration remain to be demonstrated. The 1 x 3 mm demonstrator uses a low-capacity amorphous LiCoO$_2$ cathode and a disproportionately large Si anode. Addressing these issues may be feasible through insights from this dissertation. The typical amorphous structure of sputtered metal oxide cathodes requires

crystallization at high temperatures, which necessitates the use of diffusion barriers. Li-Me-O interlayers are recommended to serve as diffusion barriers while facilitating Li^+ ion transport.

To achieve the projected power and energy densities, an anode-free structure is essential. The investigations suggest that pure carbon films provide an optimal basis for this purpose, not only due to the minimized overpotential increase but also by mitigating structural instabilities. In particular, the agglomeration of noble metals in stacked thin-film batteries could lead to catastrophic failures.

Beyond manufacturing and integration issues, current research trends point to a significant impact of anode-free batteries in future applications. The last part of this Thesis developed the basis for an optical microscope setup for *operando* investigation of Li nucleation in solid-state batteries. It is a simple, adaptable platform to directly correlate the chemo-mechanical pheonemena at the solid-electrolyte|anode-less interface. It is recommended that the microscope setup demonstrated in this study be further improved. Optical studies of the effects of seed layers on lithium nucleation may lead to new manufacturing concepts. These investigations could be complemented by cryo-FIB SEM or TEM studies to provide deeper insights into this promising field.

Figure 5.1. (a) Schematic illustration of the fabricated series-stacked thin-film battery. The two cells are marked by red dashed boxes. (b) FIB-SEM cross-section of a monolithically stacked thin-film battery connected in series. The two cells are separated only by thin current collectors, with the cathode current collector of cell 2 directly deposited on the anode current collector of cell 1. (c) Picture of four series-stacked thin-film batteries. The battery area (1×3) mm is marked by a red dashed box. (d) Charge–discharge curves of a series-stacked thin-film battery measured at C/10 (1 μA cm^{-2}). The voltage of the series-stacked battery is the combined voltage of the two individual cells, which were cycled simultaneously. (e) The discharge energy of the series-stacked thin-film battery was measured at C-rates ranging from C/10 (1 μA cm^{-2}) to 2C (20 μA cm^{-2}). From Futscher et al. [81]

BIBLIOGRAPHY

1. Letcher, T. M. Climate Change, 3–17 (2021).

2. Höök, M. & Tang, X. Depletion of fossil fuels and anthropogenic climate change—A review. *Energy Policy* **52,** 797–809. ISSN: 0301-4215 (2013).

3. Lewis, N. S. & Nocera, D. G. Powering the planet: Chemical challenges in solar energy utilization. *Proceedings of the National Academy of Sciences* **103,** 15729–15735. ISSN: 0027-8424 (2006).

4. Network, T. L. What's Going On in This Graph? | Global Temperature Change. https://www.nytimes.com/2023/01/26/learning/whats-going-on-in-this-graph-feb-1-2023.html (Jan. 2023).

5. Lenssen, N. J. L., Schmidt, G. A., Hansen, J. E., Menne, M. J., Persin, A., Ruedy, R. & Zyss, D. Improvements in the GISTEMP Uncertainty Model. *Journal of Geophysical Research: Atmospheres* **124,** 6307–6326. ISSN: 2169-897X (2019).

6. NASA. *GISS Surface Temperature Analysis (GISTEMP), version 4* https://data.giss.nasa.gov/gistemp/ (2023).

7. Administration, E. I. *Projected electricity generation worldwide in 2020 with a forecast to 2050, by energy source* tech. rep. (Statista). https://www.statista.com/statistics/238610/projected-world-electricity-generation-by-energy-source/ (2023).

8. Notton, G., Nivet, M.-L., Voyant, C., Paoli, C., Darras, C., Motte, F. & Fouilloy, A. Intermittent and stochastic character of renewable energy sources: Consequences, cost of intermittence and benefit of forecasting. *Renewable and Sustainable Energy Reviews* **87,** 96–105. ISSN: 1364-0321 (2018).

9. Castelvecchi, D. & Stoye, E. Chemistry Nobel honours world-changing batteries. *Nature* **574,** 308–308. ISSN: 0028-0836 (2019).

10. Leuthner, S. Lithium-Ion Batteries: Basics and Applications, 13–19 (2018).

11. Amrouche, S. O., Rekioua, D., Rekioua, T. & Bacha, S. Overview of energy storage in renewable energy systems. *International Journal of Hydrogen Energy* **41,** 20914–20927. ISSN: 0360-3199 (2016).

12. Group, A. *Prognostizierter Absatz von Personenkraftwagen weltweit nach Antrieb von 2021 bis 2040 (in 1.000 Fahrzeuge)* tech. rep. (Statista). https://de.statista.com/statistik/daten/studie/1244924/umfrage/pkw-absatz-weltweit-nach-antrieb/ (2023).

13. Tarascon, J.-M. & Armand, M. Issues and challenges facing rechargeable lithium batteries. *Nature* **414,** 359–367. ISSN: 0028-0836 (2001).

14. Palacín, M. R. Recent advances in rechargeable battery materials: a chemist's perspective. *Chemical Society Reviews* **38,** 2565–2575. ISSN: 0306-0012 (2009).

15. Lim, H.-D., Park, J.-H., Shin, H.-J., Jeong, J., Kim, J. T., Nam, K.-W., Jung, H.-G. & Chung, K. Y. A review of challenges and issues concerning interfaces for all-solid-state batteries. *Energy Storage Materials* **25,** 224–250. ISSN: 2405-8297 (2020).

16. Whittingham, M. Chemistry of intercalation compounds: Metal guests in chalcogenide hosts. *Progress in Solid State Chemistry* **12,** 41–99. ISSN: 0079-6786 (1978).

17. Mizushima, K., Jones, P., Wiseman, P. & Goodenough, J. Li_xCoO_2 (0<x<-1): A new cathode material for batteries of high energy density. *Materials Research Bulletin* **15,** 783–789. ISSN: 0025-5408 (1980).

18. Yazami, R. & Touzain, P. A reversible graphite-lithium negative electrode for electrochemical generators. *Journal of Power Sources* **9,** 365–371. ISSN: 0378-7753 (1983).

19. BloombergNEF. *Lithium-ion battery price worldwide from 2013 to 2023 (in 2023 U.S. dollars per kilowatt-hour)* tech. rep. (Statista, Nov. 2023). https://www.statista.com/statistics/883118/global-lithium-ion-battery-pack-costs/ (2024).

20. Janek, J. & Zeier, W. G. A solid future for battery development. *Nature Energy* **1,** 16141 (2016).

21. Lyu, Y., Wu, X., Wang, K., Feng, Z., Cheng, T., Liu, Y., Wang, M., Chen, R., Xu, L., Zhou, J., Lu, Y. & Guo, B. An Overview on the Advances of $LiCoO_2$ Cathodes for Lithium-Ion Batteries. *Advanced Energy Materials* **11.** ISSN: 1614-6832 (2021).

22. Johnston, W., Heikes, R. & Sestrich, D. The preparation, crystallography, and magnetic properties of the $Li_xCo_{(1-x)}O$ system. *Journal of Physics and Chemistry of Solids* **7,** 1–13. ISSN: 0022-3697 (1958).

23. Molenda, J., Stoklosa, A. & Bak, T. Modification in the electronic structure of cobalt bronze Li_xCoO_2 and the resulting electrochemical properties. *Solid State Ionics* **36,** 53–58. ISSN: 0167-2738 (1989).

24. Freitas, B., Jr, J. S., Costa, L. d., Ferreira, G. & Resende, J. Synthesis and Characterization of $LiCoO_2$ from Different Precursors by Sol-Gel Method. *Journal of the Brazilian Chemical Society.* ISSN: 0103-5053 (2017).

25. Liu, J., Bao, Z., Cui, Y., Dufek, E. J., Goodenough, J. B., Khalifah, P, Li, Q., Liaw, B. Y., Liu, P, Manthiram, A., Meng, Y. S., Subramanian, V. R., Toney, M. F., Viswanathan, V. V., Whittingham, M. S., Xiao, J., Xu, W., Yang, J., Yang, X.-Q. & Zhang, J.-G. Pathways for practical high-energy long-cycling lithium metal batteries. *Nature Energy* **4,** 180–186 (2019).

26. Zhang, W.-J. Structure and performance of $LiFePO_4$ cathode materials: A review. *Journal of Power Sources* **196,** 2962–2970. ISSN: 0378-7753 (2011).

27. Patoux, S., Daniel, L., Bourbon, C., Lignier, H., Pagano, C., LeCras, F., Jouanneau, S. & Martinet, S. High voltage spinel oxides for Li-ion batteries: From the material research to the application. *Journal of Power Sources* **189,** 344–352. ISSN: 0378-7753 (2009).

28. Zhou, H., Xin, F, Pei, B. & Whittingham, M. S. What Limits the Capacity of Layered Oxide Cathodes in Lithium Batteries? *ACS Energy Letters* **4,** 1902–1906. ISSN: 2380-8195 (2019).

29. Wu, F. & Yushin, G. Conversion cathodes for rechargeable lithium and lithium-ion batteries. *Energy & Environmental Science* **10,** 435–459. ISSN: 1754-5692 (2016).

30. Kaiser, M. R., Han, Z., Liang, J., Dou, S.-X. & Wang, J. Lithium sulfide-based cathode for lithium-ion/sulfur battery: Recent progress and challenges. *Energy Storage Materials* **19,** 1–15. ISSN: 2405-8297 (2019).

31. Nitta, N., Wu, F., Lee, J. T. & Yushin, G. Li-ion battery materials: present and future. *Materials Today* **18,** 252–264. ISSN: 1369-7021 (2015).

32. Zhang, W.-J. A review of the electrochemical performance of alloy anodes for lithium-ion batteries. *Journal of Power Sources* **196,** 13–24. ISSN: 0378-7753 (2011).

33. Zhu, G.-N., Wang, Y.-G. & Xia, Y.-Y. Ti-based compounds as anode materials for Li-ion batteries. *Energy & Environmental Science* **5,** 6652–6667. ISSN: 1754-5692 (2012).

34. Cabana, J., Monconduit, L., Larcher, D. & Palacín, M. R. Beyond Intercalation-Based Li-Ion Batteries: The State of the Art and Challenges of Electrode Materials Reacting Through Conversion Reactions. *Advanced Materials* **22,** E170–E192. ISSN: 0935-9648 (2010).

35. McDowell, M. T., Lee, S. W., Wang, C. & Cui, Y. The effect of metallic coatings and crystallinity on the volume expansion of silicon during electrochemical lithiation/delithiation. *Nano Energy* **1,** 401–410. ISSN: 2211-2855 (2012).

36. Shimotake, H., Rogers, G. L. & Cairns, E. J. Secondary Cells with Lithium Anodes and Immobilized Fused-Salt Electrolytes. *Industrial & Engineering Chemistry Process Design and Development* **8,** 51–56. ISSN: 0196-4305 (1969).

37. Zhang, Y., Zuo, T.-T., Popovic, J., Lim, K., Yin, Y.-X., Maier, J. & Guo, Y.-G. Towards better Li metal anodes: Challenges and strategies. *Materials Today* **33,** 56–74. ISSN: 1369-7021 (2020).

38. Zor, C., Turrell, S. J., Uyanik, M. S. & Afyon, S. Lithium Plating and Stripping: Toward Anode-Free Solid-State Batteries. *Advanced Energy and Sustainability Research,* 2300001. ISSN: 2699-9412 (2023).

39. Frith, J. T., Lacey, M. J. & Ulissi, U. A non-academic perspective on the future of lithium-based batteries. *Nature Communications* **14,** 420 (2023).

40. Guo, Y., Wu, S., He, Y.-B., Kang, F., Chen, L., Li, H. & Yang, Q.-H. Solid-state lithium batteries: Safety and prospects. *eScience* **2,** 138–163. ISSN: 2667-1417 (2022).

41. Jaumaux, P., Wu, J., Shanmukaraj, D., Wang, Y., Zhou, D., Sun, B., Kang, F., Li, B., Armand, M. & Wang, G. Non-Flammable Liquid and Quasi-Solid Electrolytes toward Highly-Safe Alkali Metal-Based Batteries. *Advanced Functional Materials* **31.** ISSN: 1616-301X (2021).

42. Manthiram, A., Yu, X. & Wang, S. Lithium battery chemistries enabled by solid-state electrolytes. *Nature Reviews Materials* **2,** 16103 (2017).

43. Yang, H. & Wu, N. Ionic conductivity and ion transport mechanisms of solid-state lithium-ion battery electrolytes: A review. *Energy Science & Engineering* **10,** 1643–1671. ISSN: 2050-0505 (2022).

44. Zhu, Y., He, X. & Mo, Y. Origin of Outstanding Stability in the Lithium Solid Electrolyte Materials: Insights from Thermodynamic Analyses Based on First-Principles Calculations. *ACS Applied Materials & Interfaces* **7,** 23685–23693. ISSN: 1944-8244 (2015).

45. Wei, R., Chen, S., Gao, T. & Liu, W. Challenges, fabrications and horizons of oxide solid electrolytes for solid-state lithium batteries. *Nano Select* **2,** 2256–2274. ISSN: 2688-4011 (2021).

46. Chen, R., Li, Q., Yu, X., Chen, L. & Li, H. Approaching Practically Accessible Solid-State Batteries: Stability Issues Related to Solid Electrolytes and Interfaces. *Chemical Reviews* **120,** 6820–6877. ISSN: 0009-2665 (2019).

47. Wu, Y., Wang, S., Li, H., Chen, L. & Wu, F. Progress in thermal stability of all-solid-state-Li-ion-batteries. *InfoMat* **3,** 827–853. ISSN: 2567-3165 (2021).

48. Ke, X., Wang, Y., Ren, G. & Yuan, C. Towards rational mechanical design of inorganic solid electrolytes for all-solid-state lithium ion batteries. *Energy Storage Materials* **26,** 313–324. ISSN: 2405-8297 (2020).

49. Henze, V. *Battery Pack Prices Fall to an Average of $132/kWh, But Rising Commodity Prices Start to Bite* Nov. 2021. https://about.bnef.com/blog/battery-pack-prices-fall-to-an-average-of-132-kwh-but-rising-commodity-prices-start-to-bite/ (2023).

50. Jiang, P., Du, G., Cao, J., Zhang, X., Zou, C., Liu, Y. & Lu, X. Solid-State Li Ion Batteries with Oxide Solid Electrolytes: Progress and Perspective. *Energy Technology* **11.** ISSN: 2194-4288 (2023).

51. Bachman, J. C., Muy, S., Grimaud, A., Chang, H.-H., Pour, N., Lux, S. F., Paschos, O., Maglia, F., Lupart, S., Lamp, P., Giordano, L. & Shao-Horn, Y. Inorganic Solid-State Electrolytes for Lithium Batteries: Mechanisms and Properties Governing Ion Conduction. *Chemical Reviews* **116,** 140–162. ISSN: 0009-2665 (2016).

52. Ramakumar, S., Deviannapoorani, C., Dhivya, L., Shankar, L. S. & Murugan, R. Lithium garnets: Synthesis, structure, Li^+ conductivity, Li^+ dynamics and applications. *Progress in Materials Science* **88,** 325–411. ISSN: 0079-6425 (2017).

53. Wu, J.-F., Pang, W. K., Peterson, V. K., Wei, L. & Guo, X. Garnet-Type Fast Li-Ion Conductors with High Ionic Conductivities for All-Solid-State Batteries. *ACS Applied Materials & Interfaces* **9,** 12461–12468. ISSN: 1944-8244 (2017).

54. Murugan, R., Thangadurai, V. & Weppner, W. Fast Lithium Ion Conduction in Garnet-Type $Li_7La_3Zr_2O_{12}$. *Angewandte Chemie International Edition* **46,** 7778–7781. ISSN: 1433-7851 (2007).

55. Awaka, J., Kijima, N., Hayakawa, H. & Akimoto, J. Synthesis and structure analysis of tetragonal $Li_7La_3Zr_2O_{12}$ with the garnet-related type structure. *Journal of Solid State Chemistry* **182,** 2046–2052. ISSN: 0022-4596 (2009).

56. Wang, C., Fu, K., Kammampata, S. P., McOwen, D. W., Samson, A. J., Zhang, L., Hitz, G. T., Nolan, A. M., Wachsman, E. D., Mo, Y., Thangadurai, V. & Hu, L. Garnet-Type Solid-State Electrolytes: Materials, Interfaces, and Batteries. *Chemical Reviews* **120,** 4257–4300. ISSN: 0009-2665 (2020).

57. Xie, H., Li, Y. & Goodenough, J. B. Low-temperature synthesis of $Li_7La_3Zr_2O_{12}$ with cubic garnet-type structure. *Materials Research Bulletin* **47,** 1229–1232. ISSN: 0025-5408 (2012).

58. Xie, H., Alonso, J. A., Li, Y., Fernández-Díaz, M. T. & Goodenough, J. B. Lithium Distribution in Aluminum-Free Cubic $Li_7La_3Zr_2O_{12}$. *Chemistry of Materials* **23,** 3587–3589. ISSN: 0897-4756 (2011).

59. O'Callaghan, M. P., Lynham, D. R., Cussen, E. J. & Chen, G. Z. Structure and Ionic-Transport Properties of Lithium-Containing Garnets $Li_3Ln_3Te_2O_{12}$ (Ln = Y, Pr, Nd, Sm-Lu). *Chemistry of Materials* **18,** 4681–4689. ISSN: 0897-4756 (2006).

60. Thangadurai, V. & Weppner, W. $Li_6ALa_2Ta_2O_{12}$ (A = Sr, Ba): Novel Garnet-Like Oxides for Fast Lithium Ion Conduction. *Advanced Functional Materials* **15,** 107–112. ISSN: 1616-301X (2005).

61. Kanehori, K., Ito, Y., Kirino, F., Miyauchi, K. & Kudo, T. Titanium disulfide films fabricated by plasma CVD. *Solid State Ionics* **18,** 818–822. ISSN: 0167-2738 (1986).

62. Akridge, J. R. & Vourlis, H. Solid state batteries using vitreous solid electrolytes. *Solid State Ionics* **18,** 1082–1087. ISSN: 0167-2738 (1986).

63. Bates, J., Dudney, N., Gruzalski, G., Zuhr, R., Choudhury, A., Luck, C. & Robertson, J. Fabrication and characterization of amorphous lithium electrolyte thin films and rechargeable thin-film batteries. *Journal of Power Sources* **43,** 103–110. ISSN: 0378-7753 (1993).

64. Bates, J., Dudney, N., Gruzalski, G., Zuhr, R., Choudhury, A., Luck, C. & Robertson, J. Electrical properties of amorphous lithium electrolyte thin films. *Solid State Ionics* **53,** 647–654. ISSN: 0167-2738 (1992).

65. Fleutot, B., Pecquenard, B., Martinez, H., Letellier, M. & Levasseur, A. Investigation of the local structure of LiPON thin films to better understand the role of nitrogen on their performance. *Solid State Ionics* **186,** 29–36. ISSN: 0167-2738 (2011).

66. Van-Jodin, L. L., Ducroquet, F., Sabary, F. & Chevalier, I. Dielectric properties, conductivity and Li^+ ion motion in LiPON thin films. *Solid State Ionics* **253,** 151–156. ISSN: 0167-2738 (2013).

67. Hamon, Y., Douard, A., Sabary, F., Marcel, C., Vinatier, P, Pecquenard, B. & Levasseur, A. Influence of sputtering conditions on ionic conductivity of LiPON thin films. *Solid State Ionics* **177,** 257–261. ISSN: 0167-2738 (2006).

68. Kim, H. T., Mun, T., Park, C., Jin, S. W. & Park, H. Y. Characteristics of lithium phosphorous oxynitride thin films deposited by metal-organic chemical vapor deposition technique. *Journal of Power Sources* **244,** 641–645. ISSN: 0378-7753 (2013).

69. Kozen, A. C., Pearse, A. J., Lin, C.-F., Noked, M. & Rubloff, G. W. Atomic Layer Deposition of the Solid Electrolyte LiPON. *Chemistry of Materials* **27,** 5324–5331. ISSN: 0897-4756 (2015).

70. Lacivita, V., Artrith, N. & Ceder, G. Structural and Compositional Factors That Control the Li-Ion Conductivity in LiPON Electrolytes. *Chemistry of Materials* **30,** 7077–7090. ISSN: 0897-4756 (2018).

71. Suzuki, A., Sasaki, S., Murayama, T., Kimura, I., Morikawa, Y., Jimbo, T. & Suu, K. Manufacturing Technology of All-Solid-State Thin-Film Battery for Stand-Alone MEMS/Sensor Application. *2017 19th International Conference on Solid-State Sensors, Actuators and Microsystems (TRANSDUCERS),* 1871–1874 (2017).

72. Siller, V, Morata, A., Eroles, M. N., Arenal, R., Gonzalez-Rosillo, J. C., Amo, J. M. L. d. & Tarancón, A. High performance LATP thin film electrolytes for all-solid-state microbattery applications. *Journal of Materials Chemistry A* **9,** 17760–17769. ISSN: 2050-7488 (2021).

73. Kim, S., Hirayama, M., Taminato, S. & Kanno, R. Epitaxial growth and lithium ion conductivity of lithium- oxide garnet for an all solid-state battery electrolyte. *Dalton Transactions* **42,** 13112–13117. ISSN: 1477-9226 (2013).

74. Mousavi, T., Chen, X., Doerrer, C., Jagger, B., Speller, S. & Grovenor, C. Fabrication of $Li_{1+x}Al_xGe_{2-x}(PO_4)_3$ thin films by sputtering for solid electrolytes. *Solid State Ionics* **354,** 115397. ISSN: 0167-2738 (2020).

75. Zhu, M. & Schmidt, O. G. Tiny robots and sensors need tiny batteries — here's how to do it. *Nature* **589,** 195–197. ISSN: 0028-0836 (2021).

76. Oudenhoven, J. F. M., Baggetto, L. & Notten, P. H. L. All-Solid-State Lithium-Ion Microbatteries: A Review of Various Three-Dimensional Concepts. *Advanced Energy Materials* **1,** 10–33. ISSN: 1614-6832 (2011).

77. Neudecker, B. J., Dudney, N. J. & Bates, J. B. "Lithium-Free" Thin-Film Battery with In Situ Plated Li Anode. *Journal of The Electrochemical Society* **147,** 517–523. ISSN: 0013-4651 (2000).

78. Bates, J., Dudney, N., Neudecker, B., Ueda, A. & Evans, C. Thin-film lithium and lithium-ion batteries. *Solid State Ionics* **135,** 33–45. ISSN: 0167-2738 (2000).

79. Pikul, J. H., Zhang, H. G., Cho, J., Braun, P. V. & King, W. P. High-power lithium ion microbatteries from interdigitated three-dimensional bicontinuous nanoporous electrodes. *Nature Communications* **4,** 1732 (2013).

80. Ferrari, S., Loveridge, M., Beattie, S. D., Jahn, M., Dashwood, R. J. & Bhagat, R. Latest advances in the manufacturing of 3D rechargeable lithium microbatteries. *Journal of Power Sources* **286,** 25–46. ISSN: 0378-7753 (2015).

81. Futscher, M. H., Brinkman, L., Müller, A., Casella, J., Aribia, A. & Romanyuk, Y. E. Monolithically-stacked thin-film solid-state batteries. *Communications Chemistry* **6,** 110 (2023).

82. Nolan, A. M., Zhu, Y., He, X., Bai, Q. & Mo, Y. Computation-Accelerated Design of Materials and Interfaces for All-Solid-State Lithium-Ion Batteries. *Joule* **2,** 2016–2046. ISSN: 2542-4351 (2018).

83. Pfenninger, R., Struzik, M., Garbayo, I., Stilp, E. & Rupp, J. L. M. A low ride on processing temperature for fast lithium conduction in garnet solid-state battery films. *Nature Energy* **4,** 475–483 (2019).

84. Kim, Y., Kim, D., Bliem, R., Vardar, G., Waluyo, I., Hunt, A., Wright, J. T., Katsoudas, J. P. & Yildiz, B. Thermally Driven Interfacial Degradation between $Li_7La_3Zr_2O_{12}$ Electrolyte and $LiNi_{0.6}Mn_{0.2}Co_{0.2}O_2$ Cathode. *Chemistry of Materials* **32,** 9531–9541. ISSN: 0897-4756 (2020).

85. Chandra, S., Kim, Y., Vivona, D., Waluyo, I., Hunt, A., Schlueter, C., Lee, J. B., Shao-Horn, Y. & Yildiz, B. Thermally-driven reactivity of $Li_{0.35}La_{0.55}TiO_3$ solid electrolyte with $LiCoO_2$ cathode. *Journal of Materials Chemistry A* **10,** 3485–3494. ISSN: 2050-7488 (2022).

86. Nolan, A. M., Wachsman, E. D. & Mo, Y. Computation-guided discovery of coating materials to stabilize the interface between lithium garnet solid electrolyte and high-energy cathodes for all-solid-state lithium batteries. *Energy Storage Materials* **41,** 571–580. ISSN: 2405-8297 (2021).

87. Myung, S.-T., Amine, K. & Sun, Y.-K. Surface modification of cathode materials from nano- to microscale for rechargeable lithium-ion batteries. *Journal of Materials Chemistry* **20,** 7074–7095. ISSN: 0959-9428 (2010).

88. Chen, Z., Qin, Y., Amine, K. & Sun, Y.-K. Role of surface coating on cathode materials for lithium -ion batteries. *Journal of Materials Chemistry* **20,** 7606–7612. ISSN: 0959-9428 (2010).

89. Kim, K. J., Balaish, M., Wadaguchi, M., Kong, L. & Rupp, J. L. M. Solid-State Li–Metal Batteries: Challenges and Horizons of Oxide and Sulfide Solid Electrolytes and Their Interfaces. *Advanced Energy Materials* **11,** 2002689. ISSN: 1614-6832 (2021).

90. Han, F., Zhu, Y., He, X., Mo, Y. & Wang, C. Electrochemical Stability of $Li_{10}GeP_2S_{12}$ and $Li_7La_3Zr_2O_{12}$ Solid Electrolytes. *Advanced Energy Materials* **6.** ISSN: 1614-6832 (2016).

91. Zhu, Y., He, X. & Mo, Y. First principles study on electrochemical and chemical stability of solid electrolyte–electrode interfaces in all-solid-state Li-ion batteries. *Journal of Materials Chemistry A* **4,** 3253–3266. ISSN: 2050-7488 (2015).

92. Shi, T., Zhang, Y.-Q., Tu, Q., Wang, Y., Scott, M. C. & Ceder, G. Characterization of mechanical degradation in an all-solid-state battery cathode. *Journal of Materials Chemistry A* **8,** 17399–17404. ISSN: 2050-7488 (2020).

93. Salvatierra, R. V., Chen, W. & Tour, J. M. What Can be Expected from "Anode-Free" Lithium Metal Batteries? *Advanced Energy and Sustainability Research* **2.** ISSN: 2699-9412 (2021).

94. Krauskopf, T., Richter, F. H., Zeier, W. G. & Janek, J. Physicochemical Concepts of the Lithium Metal Anode in Solid-State Batteries. *Chemical Reviews* **120,** 7745–7794. ISSN: 0009-2665 (2020).

95. Cao, D., Sun, X., Li, Q., Natan, A., Xiang, P. & Zhu, H. Lithium Dendrite in All-Solid-State Batteries: Growth Mechanisms, Suppression Strategies, and Characterizations. *Matter* **3,** 57–94. ISSN: 2590-2385 (2020).

96. Wang, S., Xu, H., Li, W., Dolocan, A. & Manthiram, A. Interfacial Chemistry in Solid-State Batteries: Formation of Interphase and Its Consequences. *Journal of the American Chemical Society* **140,** 250–257. ISSN: 0002-7863 (2018).

97. Wu, B., Wang, S., Lochala, J., Desrochers, D., Liu, B., Zhang, W., Yang, J. & Xiao, J. The role of the solid electrolyte interphase layer in preventing Li dendrite growth in solid-state batteries. *Energy & Environmental Science* **11,** 1803–1810. ISSN: 1754-5692 (2018).

98. Haslam, C. & Sakamoto, J. Stable Lithium Plating in "Lithium Metal-Free" Solid-State Batteries Enabled by Seeded Lithium Nucleation. *Journal of The Electrochemical Society* **170,** 040524. ISSN: 0013-4651 (2023).

99. Zheng, G., Lee, S. W., Liang, Z., Lee, H.-W., Yan, K., Yao, H., Wang, H., Li, W., Chu, S. & Cui, Y. Interconnected hollow carbon nanospheres for stable lithium metal anodes. *Nature Nanotechnology* **9,** 618–623. ISSN: 1748-3387 (2014).

100. Lee, Y.-G., Fujiki, S., Jung, C., Suzuki, N., Yashiro, N., Omoda, R., Ko, D.-S., Shiratsuchi, T., Sugimoto, T., Ryu, S., Ku, J. H., Watanabe, T., Park, Y., Aihara, Y., Im, D. & Han, I. T. High-energy long-cycling all-solid-state lithium metal batteries enabled by silver–carbon composite anodes. *Nature Energy* **5,** 299–308 (2020).

101. Dubey, R., Sastre, J., Cancellieri, C., Okur, F., Forster, A., Pompizii, L., Priebe, A., Romanyuk, Y. E., Jeurgens, L. P. H., Kovalenko, M. V. & Kravchyk, K. V. Building a Better Li-Garnet Solid Electrolyte/Metallic Li Interface with Antimony. *Advanced Energy Materials* **11,** 2102086. ISSN: 1614-6832 (2021).

102. Ji, X., Hou, S., Wang, P., He, X., Piao, N., Chen, J., Fan, X. & Wang, C. Solid-State Electrolyte Design for Lithium Dendrite Suppression. *Advanced Materials* **32,** e2002741. ISSN: 0935-9648 (2020).

103. Mattox, D. M. Handbook of Physical Vapor Deposition (PVD) Processing (Second Edition), 237–286 (2010).

104. Wang, B., Bates, J. B., Hart, F. X., Sales, B. C., Zuhr, R. A. & Robertson, J. D. Characterization of Thin-Film Rechargeable Lithium Batteries with Lithium Cobalt Oxide Cathodes. *Journal of The Electrochemical Society* **143,** 3203–3213. ISSN: 0013-4651 (1996).

105. Qi, Z., Jian, J., Huang, J., Tang, J., Wang, H., Pol, V. G. & Wang, H. $LiNi_{0.5}Mn_{0.3}Co_{0.2}O_2$/Au nanocomposite thin film cathode with enhanced electrochemical properties. *Nano Energy* **46,** 290–296. ISSN: 2211-2855 (2018).

106. Teng, S., Tan, J. & Tiwari, A. Recent developments in garnet based solid state electrolytes for thin film batteries. *Current Opinion in Solid State and Materials Science* **18,** 29–38. ISSN: 1359-0286 (2014).

107. Filippin, A. N., Lin, T.-Y., Rawlence, M., Zünd, T., Kravchyk, K., Sastre-Pellicer, J., Haass, S. G., Wäckerlin, A., Kovalenko, M. V. & Buecheler, S. Ni–Al–Cr superalloy as high temperature cathode current collector for advanced thin film Li batteries. *RSC Advances* **8,** 20304–20313. ISSN: 2046-2069 (2018).

108. Mattox, D. M. Handbook of Physical Vapor Deposition (PVD) Processing (Second Edition), 195–235 (2010).

109. Wang, S., Zhang, J., Gharbi, O., Vivier, V., Gao, M. & Orazem, M. E. Electrochemical impedance spectroscopy. *Nature Reviews Methods Primers* **1,** 41 (2021).

110. Vadhva, P., Hu, J., Johnson, M. J., Stocker, R., Braglia, M., Brett, D. J. L. & Rettie, A. J. E. Electrochemical Impedance Spectroscopy for All-Solid-State Batteries: Theory, Methods and Future Outlook. *ChemElectroChem* **8,** 1930–1947. ISSN: 2196-0216 (2021).

111. Orazem, M. E. & Tribollet, B. Electrochemical Impedance Spectroscopy (2023).

112. Orazem, M. E. & Tribollet, B. Electrochemical Impedance Spectroscopy, 1–21 (2010).

113. Orazem, M. E. & Tribollet, B. Electrochemical Impedance Spectroscopy, 61–72 (2010).

114. López, I., Morey, J., Ledeuil, J. B., Madec, L. & Martinez, H. A critical discussion on the analysis of buried interfaces in Li solid-state batteries. Ex situ and in situ / operando studies. *Journal of Materials Chemistry A* **9,** 25341–25368. ISSN: 2050-7488 (2021).

115. Wang, X., Zhang, M., Alvarado, J., Wang, S., Sina, M., Lu, B., Bouwer, J., Xu, W., Xiao, J., Zhang, J.-G., Liu, J. & Meng, Y. S. New Insights on the Structure of Electrochemically Deposited Lithium Metal and Its Solid Electrolyte Interphases via Cryogenic TEM. *Nano Letters* **17,** 7606–7612. ISSN: 1530-6984 (2017).

116. Li, Y., Li, Y., Pei, A., Yan, K., Sun, Y., Wu, C.-L., Joubert, L.-M., Chin, R., Koh, A. L., Yu, Y., Perrino, J., Butz, B., Chu, S. & Cui, Y. Atomic structure of sensitive battery materials and interfaces revealed by cryo–electron microscopy. *Science* **358,** 506–510. ISSN: 0036-8075 (2017).

117. Huang, W., Wang, J., Braun, M. R., Zhang, Z., Li, Y., Boyle, D. T., McIntyre, P. C. & Cui, Y. Dynamic Structure and Chemistry of the Silicon Solid-Electrolyte Interphase Visualized by Cryogenic Electron Microscopy. *Matter* **1,** 1232–1245. ISSN: 2590-2385 (2019).

118. Zachman, M. J., Tu, Z., Choudhury, S., Archer, L. A. & Kourkoutis, L. F. Cryo-STEM mapping of solid–liquid interfaces and dendrites in lithium-metal batteries. *Nature* **560,** 345–349. ISSN: 0028-0836 (2018).

119. Cheng, D., Wynn, T. A., Wang, X., Wang, S., Zhang, M., Shimizu, R., Bai, S., Nguyen, H., Fang, C., Kim, M.-c., Li, W., Lu, B., Kim, S. J. & Meng, Y. S. Unveiling the Stable Nature of the Solid Electrolyte Interphase between Lithium Metal and LiPON via Cryogenic Electron Microscopy. *Joule* **4,** 2484–2500. ISSN: 2542-4351. eprint: 2006.12764 (2020).

120. Müller, A., Okur, F., Aribia, A., Osenciat, N., Vaz, C. A. F., Siller, V., Kazzi, M. E., Gilshtein, E., Futscher, M. H., Kravchyk, K. V., Kovalenko, M. V. & Romanyuk, Y. E. Benchmarking the performance of lithiated metal oxide interlayers at the $LiCoO_2$ |LLZO interface. *Materials Advances* **4,** 2138–2146 (2023).

121. Liu, Q., Geng, Z., Han, C., Fu, Y., Li, S., He, Y.-b., Kang, F. & Li, B. Challenges and perspectives of garnet solid electrolytes for all solid-state lithium batteries. *Journal of Power Sources* **389,** 120–134. ISSN: 0378-7753 (2018).

122. Thompson, T., Yu, S., Williams, L., Schmidt, R. D., Garcia-Mendez, R., Wolfenstine, J., Allen, J. L., Kioupakis, E., Siegel, D. J. & Sakamoto, J. Electrochemical Window of the Li-Ion Solid Electrolyte $Li_7La_3Zr_2O_{12}$. *ACS Energy Letters* **2,** 462–468. ISSN: 2380-8195 (2017).

123. Lu, Y., Huang, X., Ruan, Y., Wang, Q., Kun, R., Yang, J. & Wen, Z. An in situ element permeation constructed high endurance Li–LLZO interface at high current densities. *Journal of Materials Chemistry A* **6,** 18853–18858. ISSN: 2050-7488 (2018).

124. Luntz, A. C., Voss, J. & Reuter, K. Interfacial Challenges in Solid-State Li Ion Batteries. *The Journal of Physical Chemistry Letters* **6,** 4599–4604. ISSN: 1948-7185 (2015).

125. Balaish, M., Gonzalez-Rosillo, J. C., Kim, K. J., Zhu, Y., Hood, Z. D. & Rupp, J. L. M. Processing thin but robust electrolytes for solid-state batteries. *Nature Energy* **6,** 227–239 (2021).

126. Barai, P, Rojas, T., Narayanan, B., Ngo, A. T., Curtiss, L. A. & Srinivasan, V. Investigation of Delamination-Induced Performance Decay at the Cathode/LLZO Interface. *Chemistry of Materials* **33,** 5527–5541. ISSN: 0897-4756 (2021).

127. Nie, K., Hong, Y., Qiu, J., Li, Q., Yu, X., Li, H. & Chen, L. Interfaces Between Cathode and Electrolyte in Solid State Lithium Batteries: Challenges and Perspectives. *Frontiers in Chemistry* **6,** 616. ISSN: 2296-2646 (2018).

128. Haruyama, J., Sodeyama, K. & Tateyama, Y. Cation Mixing Properties toward Co Diffusion at the $LiCoO_2$ Cathode/Sulfide Electrolyte Interface in a Solid-State Battery. *ACS Applied Materials & Interfaces* **9,** 286–292. ISSN: 1944-8244 (2017).

129. Xu, J., Hu, E., Nordlund, D., Mehta, A., Ehrlich, S. N., Yang, X.-Q. & Tong, W. Understanding the Degradation Mechanism of Lithium Nickel Oxide Cathodes for Li-Ion Batteries. *ACS Applied Materials & Interfaces* **8,** 31677–31683. ISSN: 1944-8244 (2016).

130. Yu, X. & Manthiram, A. Electrode–electrolyte interfaces in lithium-based batteries. *Energy & Environmental Science* **11,** 527–543. ISSN: 1754-5692 (2018).

131. Vardar, G., Bowman, W. J., Lu, Q., Wang, J., Chater, R. J., Aguadero, A., Seibert, R., Terry, J., Hunt, A., Waluyo, I., Fong, D. D., Jarry, A., Crumlin, E. J., Hellstrom, S. L., Chiang, Y.-M. & Yildiz, B. Structure, Chemistry, and Charge Transfer Resistance of the Interface between $Li_7La_3Zr_2O_{12}$ Electrolyte and $LiCoO_2$ Cathode. *Chemistry of Materials* **30,** 6259–6276. ISSN: 0897-4756 (2018).

132. Liu, H., Yang, Y. & Zhang, J. Investigation and improvement on the storage property of $LiNi_{0.8}Co_{0.2}O_2$ as a cathode material for lithium-ion batteries. *Journal of Power Sources* **162,** 644–650. ISSN: 0378-7753 (2006).

133. Sharafi, A., Yu, S., Naguib, M., Lee, M., Ma, C., Meyer, H. M., Nanda, J., Chi, M., Siegel, D. J. & Sakamoto, J. Impact of air exposure and surface chemistry on Li–Li$_7$La$_3$Zr$_2$O$_{12}$ interfacial resistance. *Journal of Materials Chemistry A* **5,** 13475–13487. ISSN: 2050-7488 (2017).

134. Sari, H. M. K. & Li, X. Controllable Cathode–Electrolyte Interface of LiNi$_{0.8}$Co$_{0.1}$Mn$_{0.1}$O$_2$ for Lithium Ion Batteries: A Review. *Advanced Energy Materials* **9,** 1901597. ISSN: 1614-6832 (2019).

135. Aribia, A., Sastre, J., Chen, X., Gilshtein, E., Futscher, M. H., Tiwari, A. N. & Romanyuk, Y. E. In Situ Lithiated ALD Niobium Oxide for Improved Long Term Cycling of Layered Oxide Cathodes: A Thin-Film Model Study. *Journal of The Electrochemical Society* **168,** 040513. ISSN: 0013-4651 (2021).

136. Kato, T., Hamanaka, T., Yamamoto, K., Hirayama, T., Sagane, F., Motoyama, M. & Iriyama, Y. In-situ Li$_7$La$_3$Zr$_2$O$_{12}$/LiCoO$_2$ interface modification for advanced all-solid-state battery. *Journal of Power Sources* **260,** 292–298. ISSN: 0378-7753 (2014).

137. Müller, M., Schmieg, J., Dierickx, S., Joos, J., Weber, A., Gerthsen, D. & Ivers-Tiffee, E. Reducing Impedance at a Li-Metal Anode/Garnet-Type Electrolyte Interface Implementing Chemically Resolvable In Layers. *ACS Applied Materials & Interfaces* **14,** 14739–14752. ISSN: 1944-8244 (2022).

138. Kaufherr, N., Eichorst, D. J. & Payne, D. A. X-ray photoelectron spectroscopy studies of alkoxide-derived lithium niobate. *Journal of Vacuum Science & Technology A: Vacuum, Surfaces, and Films* **14,** 299–305. ISSN: 0734-2101 (1996).

139. Shank, J. C., Tellekamp, M. B. & Doolittle, W. A. The crystallization and properties of sputter deposited lithium niobite. *Thin Solid Films* **609,** 6–11. ISSN: 0040-6090 (2016).

140. Tago, T., Kataoka, N., Tanaka, H., Kinoshita, K. & Kishida, S. XPS study from a clean surface of Al$_2$O$_3$ single crystals. *Procedia Engineering* **216.** For Al 2p, 175–181. ISSN: 1877-7058 (2017).

141. Wei, T., Yan, F. & Tian, J. Characterization and wear- and corrosion-resistance of microarc oxidation ceramic coatings on aluminum alloy. *Journal of Alloys and Compounds* **389,** 169–176. ISSN: 0925-8388 (2005).

142. Heo, S. J., Hu, B., Manthina, V., Hilmi, A., Yuh, C.-Y., Surendranath, A. & Singh, P. Stability of lithium aluminate in reducing and oxidizing atmospheres at 700 °C. *International Journal of Hydrogen Energy* **41,** 18884–18892. ISSN: 0360-3199 (2016).

143. Parmigiani, F., Kay, E., Bagus, P. S. & Nelin, C. J. Core binding energies for clusters deposited on different insulating substrates: esca spectra and theoretical electronic structure studies. *Journal of Electron Spectroscopy and Related Phenomena* **36,** 257–267. ISSN: 0368-2048 (1985).

144. Mason, M. G. Electronic structure of supported small metal clusters. *Physical Review B* **27,** 748–762. ISSN: 1098-0121 (1983).

145. Xu, H., Chen, J., Li, Y., Guo, X., Shen, Y., Wang, D., Zhang, Y. & Wang, Z. Fabrication of $Li_4Ti_5O_{12}$-TiO_2 Nanosheets with Structural Defects as High-Rate and Long-Life Anodes for Lithium-Ion Batteries. *Scientific Reports* **7,** 2960 (2017).

146. Cai, Y., Huang, Y., Jia, W., Wang, X., Guo, Y., Jia, D., Sun, Z., Pang, W. & Guo, Z. Super high-rate, long cycle life of europium-modified, carbon-coated, hierarchical mesoporous lithium-titanate anode materials for lithium ion batteries. *Journal of Materials Chemistry A* **4,** 9949–9957. ISSN: 2050-7488 (2016).

147. Ren, Y. & Wachsman, E. D. All Solid-State Li/LLZO/LCO Battery Enabled by Alumina Interfacial Coating. *Journal of The Electrochemical Society* **169,** 040529. ISSN: 0013-4651 (2022).

148. Choi, H. C., Lee, S. Y., Kim, S. B., Kim, M. G., Lee, M. K., Shin, H. J. & Lee, J. S. Local Structural Characterization for Electrochemical Insertion-Extraction of Lithium into CoO with X-ray Absorption Spectroscopy. *The Journal of Physical Chemistry B* **106,** 9252–9260. ISSN: 1520-6106 (2002).

149. Wang, J., Ji, Y., Appathurai, N., Zhou, J. & Yang, Y. Nanoscale chemical imaging of the additive effects on the interfaces of high-voltage LiCoO 2 composite electrodes. *Chemical Communications* **53,** 8581–8584. ISSN: 1359-7345 (2017).

150. Cheng, L., Crumlin, E. J., Chen, W., Qiao, R., Hou, H., Lux, S. F., Zorba, V., Russo, R., Kostecki, R., Liu, Z., Persson, K., Yang, W., Cabana, J., Richardson, T., Chen, G. & Doeff, M. The origin of high electrolyte–electrode interfacial resistances in lithium cells containing garnet type solid electrolytes. *Physical Chemistry Chemical Physics* **16**, 18294–18300. ISSN: 1463-9076 (2014).

151. Park, K., Yu, B.-C., Jung, J.-W., Li, Y., Zhou, W., Gao, H., Son, S. & Goodenough, J. B. Electrochemical Nature of the Cathode Interface for a Solid-State Lithium-Ion Battery: Interface between $LiCoO_2$ and Garnet-$Li_7La_3Zr_2O_{12}$. *Chemistry of Materials* **28**, 8051–8059. ISSN: 0897-4756 (2016).

152. Tröltzsch, U., Kanoun, O. & Tränkler, H.-R. Characterizing aging effects of lithium ion batteries by impedance spectroscopy. *Electrochimica Acta* **51**, 1664–1672. ISSN: 0013-4686 (2006).

153. Zhang, W., Weber, D. A., Weigand, H., Arlt, T., Manke, I., Schroeder, D., Koerver, R., Leichtweiss, T., Hartmann, P., Zeier, W. G. & Janek, J. Interfacial Processes and Influence of Composite Cathode Microstructure Controlling the Performance of All-Solid-State Lithium Batteries. *ACS Applied Materials & Interfaces* **9**, 17835–17845. ISSN: 1944-8244 (2017).

154. Song, S., Wu, Y., Dong, Z., Deng, F., Tang, W., Yao, J., Wen, Z., Lu, L., Hu, N. & Molenda, J. Multi-substituted garnet-type electrolytes for solid-state lithium batteries. *Ceramics International* **46**, 5489–5494. ISSN: 0272-8842 (2020).

155. Xiao, Y., Wang, Y., Bo, S.-H., Kim, J. C., Miara, L. J. & Ceder, G. Understanding interface stability in solid-state batteries. *Nature Reviews Materials* **5**, 105–126 (2020).

156. Kim, Y., Yoo, A., Schmidt, R., Sharafi, A., Lee, H., Wolfenstine, J. & Sakamoto, J. Electrochemical Stability of $Li_{6.5}La_3Zr_{1.5}M_{0.5}O_{12}$ (M = Nb or Ta) against Metallic Lithium. *Frontiers in Energy Research* **4**, 20 (2016).

157. Irvine, J. T. S., Sinclair, D. C. & West, A. R. Electroceramics: Characterization by Impedance Spectroscopy. *Advanced Materials* **2**, 132–138. ISSN: 0935-9648 (1990).

158. Thompson, T., Wolfenstine, J., Allen, J. L., Johannes, M., Huq, A., David, I. N. & Sakamoto, J. Tetragonal vs. cubic phase stability in Al – free Ta doped $Li_7La_3Zr_2O_{12}$ (LLZO). *Journal of Materials Chemistry A* **2,** 13431–13436. ISSN: 2050-7488 (2014).

159. Sharafi, A., Meyer, H. M., Nanda, J., Wolfenstine, J. & Sakamoto, J. Characterizing the $Li–Li_7La_3Zr_2O_{12}$ interface stability and kinetics as a function of temperature and current density. *Journal of Power Sources* **302,** 135–139. ISSN: 0378-7753 (2016).

160. Ohta, S., Kobayashi, T., Seki, J. & Asaoka, T. Electrochemical performance of an all-solid-state lithium ion battery with garnet-type oxide electrolyte. *Journal of Power Sources* **202,** 332–335. ISSN: 0378-7753 (2012).

161. Sastre, J., Chen, X., Aribia, A., Tiwari, A. N. & Romanyuk, Y. E. Fast Charge Transfer across the $Li_7La_3Zr_2O_{12}$ Solid Electrolyte/$LiCoO_2$ Cathode Interface Enabled by an Interphase-Engineered All-Thin-Film Architecture. *ACS Applied Materials & Interfaces* **12,** 36196–36207. ISSN: 1944-8244 (2020).

162. Li, X., Jin, L., Song, D., Zhang, H., Shi, X., Wang, Z., Zhang, L. & Zhu, L. $LiNbO_3$-coated $LiNi_{0.8}Co_{0.1}Mn_{0.1}O_2$ cathode with high discharge capacity and rate performance for all-solid-state lithium battery. *Journal of Energy Chemistry* **40,** 39–45. ISSN: 2095-4956 (2020).

163. Ohta, N., Takada, K., Sakaguchi, I., Zhang, L., Ma, R., Fukuda, K., Osada, M. & Sasaki, T. $LiNbO_3$-coated $LiCoO_2$ as cathode material for all solid-state lithium secondary batteries. *Electrochemistry Communications* **9,** 1486–1490. ISSN: 1388-2481 (2007).

164. Guo, H., Shen, F., Guo, W., Zeng, D., Yin, Y. & Han, X. $LiCoO_2/Li_{6.75}La_3Zr_{1.75}Nb_{0.75}O_{12}$ interface modification enables all-solid-state battery. *Materials Letters* **301,** 130302. ISSN: 0167-577X (2021).

165. Aurbach, D., Markovsky, B., Rodkin, A., Levi, E., Cohen, Y., Kim, H.-J. & Schmidt, M. On the capacity fading of $LiCoO_2$ intercalation electrodes: the effect of cycling, storage, temperature, and surface film forming additives. *Electrochimica Acta* **47,** 4291–4306. ISSN: 0013-4686 (2002).

166. Liao, C.-L. & Fung, K.-Z. Lithium cobalt oxide cathode film prepared by rf sputtering. *Journal of Power Sources* **128,** 263–269. ISSN: 0378-7753 (2004).

167. Reddy, M., Pecquenard, B., Vinatier, P. & Levasseur, A. Cyclic voltammetry and galvanostatic cycling characteristics of LiNiVO4 thin films during lithium insertion and re/de-insertion. *Electrochemistry Communications* **9,** 409–415. ISSN: 1388-2481 (2007).

168. Kim, T., Choi, W., Shin, H.-C., Choi, J.-Y., Kim, J. M., Park, M.-S. & Yoon, W.-S. Applications of Voltammetry in Lithium Ion Battery Research. *Journal of Electrochemical Science and Technology* **11,** 14–25. ISSN: 2093-8551 (2020).

169. Nelson, K. J., Harlow, J. E. & Dahn, J. R. A Comparison of NMC/-Graphite Pouch Cells and Commercially Available $LiCoO_2$/Graphite Pouch Cells Tested to High Potential. *Journal of The Electrochemical Society* **165,** A456–A462. ISSN: 0013-4651 (2018).

170. Liu, T., Ren, Y., Shen, Y., Zhao, S.-X., Lin, Y. & Nan, C.-W. Achieving high capacity in bulk-type solid-state lithium ion battery based on $Li_{6.75}La_3Zr_{1.75}Ta_{0.75}O_{12}$ electrolyte: Interfacial resistance. *Journal of Power Sources* **324,** 349–357. ISSN: 0378-7753 (2016).

171. Luo, W., Gong, Y., Zhu, Y., Li, Y., Yao, Y., Zhang, Y., Fu, K. (, Pastel, G., Lin, C.-F., Mo, Y., Wachsman, E. D. & Hu, L. Reducing Interfacial Resistance between Garnet-Structured Solid-State Electrolyte and Li-Metal Anode by a Germanium Layer. *Advanced Materials* **29,** 1606042. ISSN: 0935-9648 (2017).

172. Kato, M., Hayashi, T., Hasegawa, G., Lu, X., Miyazaki, T., Matsuda, Y., Kuwata, N., Kurihara, K. & Kawamura, J. Electrochemical properties of $LiCoO_2$ thin film surface modified by lithium tantalate and lithium niobate coatings. *Solid State Ionics* **308,** 54–60. ISSN: 0167-2738 (2017).

173. Wang, D., Sun, Q., Luo, J., Liang, J., Sun, Y., Li, R., Adair, K., Zhang, L., Yang, R., Lu, S., Huang, H. & Sun, X. Mitigating the Interfacial Degradation in Cathodes for High-Performance Oxide-Based Solid-State Lithium Batteries. *ACS Applied Materials & Interfaces* **11,** 4954–4961. ISSN: 1944-8244 (2019).

174. Müller, M., Schneider, L., Bohn, N., Binder, J. R. & Bauer, W. Effect of Nanostructured and Open-Porous Particle Morphology on Electrode Processing and Electrochemical Performance of Li-Ion Batteries. *ACS Applied Energy Materials* **4,** 1993–2003. ISSN: 2574-0962 (2021).

175. Ihrig, M., Finsterbusch, M., Laptev, A. M., Tu, C.-h., Tran, N. T. T., Lin, C.-a., Kuo, L.-Y., Ye, R., Sohn, Y. J., Kaghazchi, P., Lin, S.-k., Fattakhova-Rohlfing, D. & Guillon, O. Study of $LiCoO_2/Li_7La_3Zr_2O_{12}$:Ta Interface Degradation in All-Solid-State Lithium Batteries. *ACS Applied Materials & Interfaces* **14,** 11288–11299. ISSN: 1944-8244 (2022).

176. Wang, Y., Yuan, P., Xu, Z., Liu, X.-X., Feng, S., Cao, M., Cao, C., Wang, X., Pan, L. & Sun, Z. Ti_3C_2T x MXene in-situ transformed Li_2TiO_3 interface layer enabling 4.5 V-$LiCoO_2$/sulfide all-solid-state lithium batteries with superior rate capability and cyclability. *Chinese Chemical Letters,* 108776. ISSN: 1001-8417 (2023).

177. Kim, K. J. & Rupp, J. L. M. All ceramic cathode composite design and manufacturing towards low interfacial resistance for garnet-based solid-state lithium batteries. *Energy & Environmental Science* **13,** 4930–4945. ISSN: 1754-5692 (2020).

178. Yamamoto, T., Iwasaki, H., Suzuki, Y., Sakakura, M., Fujii, Y., Motoyama, M. & Iriyama, Y. A Li-free inverted-stack all-solid-state thin film battery using crystalline cathode material. *Electrochemistry Communications* **105,** 106494. ISSN: 1388-2481 (2019).

179. Dubarry, M., Truchot, C. & Liaw, B. Y. Synthesize battery degradation modes via a diagnostic and prognostic model. *Journal of Power Sources* **219,** 204–216. ISSN: 0378-7753 (2012).

180. Dubarry, M., Qin, N. & Brooker, P. Calendar aging of commercial Li-ion cells of different chemistries – A review. *Current Opinion in Electrochemistry* **9,** 106–113. ISSN: 2451-9103 (2018).

181. Xia, H., Lu, L. & Ceder, G. Li diffusion in $LiCoO_2$ thin films prepared by pulsed laser deposition. *Journal of Power Sources* **159,** 1422–1427. ISSN: 0378-7753 (2006).

182. Müller, A. *LinkedIn Discussion on Kink* Apr. 2023. https://www.li nkedin.com/posts/muellerandre96_ssb-lco-llzo-activity-7055178457030225921-kBor?utm_source=share&utm_medium=m ember_desktop (2023).

183. Lu, Y., Zhao, C.-Z., Hu, J.-K., Sun, S., Yuan, H., Fu, Z.-H., Chen, X., Huang, J.-Q., Ouyang, M. & Zhang, Q. The void formation behaviors in working solid-state Li metal batteries. *Science Advances* **8,** eadd0510 (2022).

184. Krauskopf, T., Hartmann, H., Zeier, W. G. & Janek, J. Toward a Fundamental Understanding of the Lithium Metal Anode in Solid-State Batteries: An Electrochemo-Mechanical Study on the Garnet-Type Solid Electrolyte $Li_{6.25}Al_{0.25}La_3Zr_2O_{12}$. *ACS Applied Materials & Interfaces* **11,** 14463–14477. ISSN: 1944-8244 (2019).

185. Wang, M. J., Choudhury, R. & Sakamoto, J. Characterizing the Li-Solid-Electrolyte Interface Dynamics as a Function of Stack Pressure and Current Density. *Joule* **3,** 2165–2178. ISSN: 2542-4351 (2019).

186. Zhang, H., Dubey, R., Inniger, M., Okur, F., Wullich, R., Parrilli, A., Karabay, D. T., Neels, A., Kravchyk, K. V. & Kovalenko, M. V. Ultrafast-sintered self-standing LLZO membranes for high energy density lithium-garnet solid-state batteries. *Cell Reports Physical Science* **4,** 101473. ISSN: 2666-3864 (2023).

187. Zhang, H., Paggiaro, G., Okur, F., Huwiler, J., Cancellieri, C., Jeurgens, L. P. H., Chernyshov, D., Beek, W. v., Kovalenko, M. V. & Kravchyk, K. V. On High-Temperature Thermal Cleaning of $Li_7La_3Zr_2O_{12}$ Solid-State Electrolytes. *ACS Applied Energy Materials* **6,** 6972–6980. ISSN: 2574-0962 (2023).

188. Okur, F., Zhang, H., Karabay, D. T., Muench, K., Parrilli, A., Neels, A., Dachraoui, W., Rossell, M. D., Cancellieri, C., Jeurgens, L. P. H., Kravchyk, K. V. & Kovalenko, M. V. Intermediate-Stage Sintered LLZO Scaffolds for Li-Garnet Solid-State Batteries. *Advanced Energy Materials* **13.** ISSN: 1614-6832 (2023).

189. Hou, A.-Y., Huang, C.-Y., Tsai, C.-L., Huang, C.-W., Schierholz, R., Lo, H.-Y., Tempel, H., Kungl, H., Eichel, R.-A., Chang, J.-K. & Wu, W.-W. All-Solid-State Garnet-Based Lithium Batteries at Work–In Operando TEM Investigations of Delithiation/Lithiation Process and Capacity Degradation Mechanism. *Advanced Science* **10,** 2205012. ISSN: 2198-3844 (2023).

190. Hausbrand, R., Cherkashinin, G., Ehrenberg, H., Gröting, M., Albe, K., Hess, C. & Jaegermann, W. Fundamental degradation mechanisms of layered oxide Li-ion battery cathode materials: Methodology, insights and novel approaches. *Materials Science and Engineering: B* **192,** 3–25. ISSN: 0921-5107 (2015).

191. Kalluri, S., Yoon, M., Jo, M., Park, S., Myeong, S., Kim, J., Dou, S. X., Guo, Z. & Cho, J. Surface Engineering Strategies of Layered LiCoO$_2$ Cathode Material to Realize High-Energy and High-Voltage Li-Ion Cells. *Advanced Energy Materials* **7.** ISSN: 1614-6832 (2017).

192. Mukhopadhyay, A. & Sheldon, B. W. Deformation and stress in electrode materials for Li-ion batteries. *Progress in Materials Science* **63,** 58–116. ISSN: 0079-6425 (2014).

193. Yan, P., Zheng, J., Gu, M., Xiao, J., Zhang, J.-G. & Wang, C.-M. Intragranular cracking as a critical barrier for high-voltage usage of layer-structured cathode for lithium-ion batteries. *Nature Communications* **8,** 14101 (2017).

194. Jiang, Y., Yan, P., Yu, M., Li, J., Jiao, H., Zhou, B. & Sui, M. Atomistic mechanism of cracking degradation at twin boundary of LiCoO$_2$. *Nano Energy* **78,** 105364. ISSN: 2211-2855 (2020).

195. Zhang, Q. & White, R. E. Moving Boundary Model for the Discharge of a LiCoO$_2$ Electrode. *Journal of The Electrochemical Society* **154,** A587–A596. ISSN: 0013-4651 (2007).

196. Li, S., Sun, Y., Gao, A., Zhang, Q., Lu, X. & Lu, X. Sustainable LiCoO$_2$ by collective glide of CoO$_6$ slabs upon charge/discharge. *Proceedings of the National Academy of Sciences* **119,** e2120060119. ISSN: 0027-8424 (2022).

197. Hatzell, K. B. Anode-Less or Anode-Free? *ACS Energy Letters* **8,** 4775–4776. ISSN: 2380-8195 (2023).

198. Zhu, P., Gastol, D., Marshall, J., Sommerville, R., Goodship, V. & Kendrick, E. A review of current collectors for lithium-ion batteries. *Journal of Power Sources* **485,** 229321. ISSN: 0378-7753 (2021).

199. Müller, A., Paravicini, L., Morzy, J., Krause, M., Casella, J., Osenciat, N., Futscher, M. H. & Romanyuk, Y. E. Influence of Au, Pt, and C Seed Layers on Lithium Nucleation Dynamics for Anode-Free Solid-State Batteries. *ACS Applied Materials & Interfaces* **16,** 695–703. ISSN: 1944-8244 (2024).

200. Albertus, P., Babinec, S., Litzelman, S. & Newman, A. Status and challenges in enabling the lithium metal electrode for high-energy and low-cost rechargeable batteries. *Nature Energy* **3,** 16–21 (2018).

201. Zhang, Z., Shao, Y., Lotsch, B., Hu, Y.-S., Li, H., Janek, J., Nazar, L. F., Nan, C.-W., Maier, J., Armand, M. & Chen, L. New horizons for inorganic solid state ion conductors. *Energy & Environmental Science* **11,** 1945–1976. ISSN: 1754-5692 (2018).

202. Goodenough, J. B. & Kim, Y. Challenges for Rechargeable Li Batteries. *Chemistry of Materials* **22,** 587–603. ISSN: 0897-4756 (2010).

203. Wang, J., Ge, B., Li, H., Yang, M., Wang, J., Liu, D., Fernandez, C., Chen, X. & Peng, Q. Challenges and progresses of lithium-metal batteries. *Chemical Engineering Journal* **420,** 129739. ISSN: 1385-8947 (2021).

204. Becking, J., Gröbmeyer, A., Kolek, M., Rodehorst, U., Schulze, S., Winter, M., Bieker, P. & Stan, M. C. Lithium-Metal Foil Surface Modification: An Effective Method to Improve the Cycling Performance of Lithium-Metal Batteries. *Advanced Materials Interfaces* **4,** 1700166. ISSN: 2196-7350 (2017).

205. Weber, R., Genovese, M., Louli, A. J., Hames, S., Martin, C., Hill, I. G. & Dahn, J. R. Long cycle life and dendrite-free lithium morphology in anode-free lithium pouch cells enabled by a dual-salt liquid electrolyte. *Nature Energy* **4,** 683–689 (2019).

206. Assegie, A. A., Cheng, J.-H., Kuo, L.-M., Su, W.-N. & Hwang, B.-J. Polyethylene oxide film coating enhances lithium cycling efficiency of an anode-free lithium-metal battery. *Nanoscale* **10,** 6125–6138. ISSN: 2040-3364 (2018).

207. Cohn, A. P., Muralidharan, N., Carter, R., Share, K. & Pint, C. L. Anode-Free Sodium Battery through in Situ Plating of Sodium Metal. *Nano Letters* **17,** 1296–1301. ISSN: 1530-6984 (2017).

208. Qian, J., Adams, B. D., Zheng, J., Xu, W., Henderson, W. A., Wang, J., Bowden, M. E., Xu, S., Hu, J. & Zhang, J.-G. Anode-Free Rechargeable Lithium Metal Batteries. *Advanced Functional Materials* **26,** 7094–7102. ISSN: 1616-301X (2016).

209. Heubner, C., Maletti, S., Auer, H., Hüttl, J., Voigt, K., Lohrberg, O., Nikolowski, K., Partsch, M. & Michaelis, A. From Lithium-Metal toward Anode-Free Solid-State Batteries: Current Developments, Issues, and Challenges. *Advanced Functional Materials,* 2106608. ISSN: 1616-301X (2021).

210. Pei, A., Zheng, G., Shi, F., Li, Y. & Cui, Y. Nanoscale Nucleation and Growth of Electrodeposited Lithium Metal. *Nano Letters* **17,** 1132–1139. ISSN: 1530-6984 (2017).

211. Yan, K., Lu, Z., Lee, H.-W., Xiong, F., Hsu, P.-C., Li, Y., Zhao, J., Chu, S. & Cui, Y. Selective deposition and stable encapsulation of lithium through heterogeneous seeded growth. *Nature Energy* **1,** 16010 (2016).

212. Kwon, H., Lee, J.-H., Roh, Y., Baek, J., Shin, D. J., Yoon, J. K., Ha, H. J., Kim, J. Y. & Kim, H.-T. An electron-deficient carbon current collector for anode-free Li-metal batteries. *Nature Communications* **12,** 5537 (2021).

213. Zhang, S. S., Fan, X. & Wang, C. A tin-plated copper substrate for efficient cycling of lithium metal in an anode-free rechargeable lithium battery. *Electrochimica Acta* **258,** 1201–1207. ISSN: 0013-4686 (2017).

214. Feng, W., Dong, X., Zhang, X., Lai, Z., Li, P., Wang, C., Wang, Y. & Xia, Y. Li/Garnet Interface Stabilization by Thermal-Decomposition Vapor Deposition of an Amorphous Carbon Layer. *Angewandte Chemie International Edition* **59,** 5346–5349. ISSN: 1433-7851 (2020).

215. Futscher, M. H., Amelal, T., Sastre, J., Müller, A., Patidar, J., Aribia, A., Thorwarth, K., Siol, S. & Romanyuk, Y. E. Influence of amorphous carbon interlayers on nucleation and early growth of lithium metal at the current collector-solid electrolyte interface. *Journal of Materials Chemistry A* **10,** 15535–15542. ISSN: 2050-7488 (2022).

216. Yamamoto, T., Sugiura, Y., Iwasaki, H., Motoyama, M. & Iriyama, Y. Freestanding all-solid-state rechargeable lithium batteries with in-situ formed positive electrodes. *Solid State Ionics* **337,** 19–23. ISSN: 0167-2738 (2019).

217. Motoyama, M., Ejiri, M., Yamamoto, T. & Iriyama, Y. In Situ Scanning Electron Microscope Observations of Li Plating/Stripping Reactions with Pt Current Collectors on LiPON Electrolyte. *Journal of The Electrochemical Society* **165,** A1338–A1347. ISSN: 0013-4651 (2018).

218. Chen, W., Fu, M., Zhao, Q., Zhou, A., Huang, W. & Wang, J. Au-modified 3D carbon cloth as a dendrite-free framework for Li metal with excellent electrochemical stability. *Journal of Alloys and Compounds* **871,** 159491. ISSN: 0925-8388 (2021).

219. Huang, M., Yao, Z., Yang, Q. & Li, C. Consecutive Nucleation and Confinement Modulation towards Li Plating in Seeded Capsules for Durable Li-Metal Batteries. *Angewandte Chemie International Edition* **60,** 14040–14050. ISSN: 1433-7851 (2021).

220. Xu, T., Hou, L., Yan, C., Hou, J., Tian, B., Yuan, H., Kong, D., Wang, H., Li, X., Wang, Y. & Zhang, G. Uniform lithium deposition guided by Au nanoparticles in vertical-graphene/carbon-cloth skeleton for dendrite-free and stable lithium metal anode. *Scripta Materialia* **229,** 115352. ISSN: 1359-6462 (2023).

221. Krauskopf, T., Dippel, R., Hartmann, H., Peppler, K., Mogwitz, B., Richter, F. H., Zeier, W. G. & Janek, J. Lithium-Metal Growth Kinetics on LLZO Garnet-Type Solid Electrolytes. *Joule* **3,** 2030–2049. ISSN: 2542-4351 (2019).

222. Kim, S., Jung, C., Kim, H., Thomas-Alyea, K. E., Yoon, G., Kim, B., Badding, M. E., Song, Z., Chang, J., Kim, J., Im, D. & Kang, K. The Role of Interlayer Chemistry in Li-Metal Growth through a Garnet-Type Solid Electrolyte. *Advanced Energy Materials* **10,** 1903993. ISSN: 1614-6832 (2020).

223. Dussart, T., Rividi, N., Fialin, M., Toussaint, G., Stevens, P. & Laberty-Robert, C. Critical Current Density Limitation of LLZO Solid Electrolyte: Microstructure vs Interface. *Journal of The Electrochemical Society* **168,** 120550. ISSN: 0013-4651 (2021).

224. Sicolo, S., Fingerle, M., Hausbrand, R. & Albe, K. Interfacial instability of amorphous LiPON against lithium: A combined Density Functional Theory and spectroscopic study. *Journal of Power Sources* **354,** 124–133. ISSN: 0378-7753 (2017).

225. Sangster, J. & Pelton, A. The li-pt (lithium-platinum) system. *Journal of Phase Equilibria* **12,** 678–681. ISSN: 1054-9714 (1991).

226. Fathi, R., Sanderson, R., Lucas, L. & Dahn, J. The electrochemical reaction of lithium with high-capacity dense sputtered carbon. *Carbon* **74,** 249–254. ISSN: 0008-6223 (2014).

227. Motoyama, M., Ejiri, M., Nakajima, H. & Iriyama, Y. Mechanical Failure of Cu Current Collector Films Affecting Li Plating/Stripping Cycles at Cu/LiPON Interfaces. *Journal of The Electrochemical Society* **170,** 012503. ISSN: 0013-4651 (2023).

228. Inaoka, T., Asakura, T., Otoyama, M., Motohashi, K., Sakuda, A., Tatsumisago, M. & Hayashi, A. Tin Interlayer at the Li/Li_3PS_4 Interface for Improved Li Stripping/Plating Performance. *The Journal of Physical Chemistry C* **127,** 10453–10458. ISSN: 1932-7447 (2023).

229. Bloi, L. M., Hippauf, F., Boenke, T., Rauche, M., Paasch, S., Schutjajew, K., Pampel, J., Schwotzer, F., Dörfler, S., Althues, H., Oschatz, M., Brunner, E. & Kaskel, S. Mechanistic insights into the reversible lithium storage in an open porous carbon via metal cluster formation in all solid-state batteries. *Carbon* **188,** 325–335. ISSN: 0008-6223 (2022).

230. Sagane, F., Ikeda, K.-i., Okita, K., Sano, H., Sakaebe, H. & Iriyama, Y. Effects of current densities on the lithium plating morphology at a lithium phosphorus oxynitride glass electrolyte/copper thin film interface. *Journal of Power Sources* **233,** 34–42. ISSN: 0378-7753 (2013).

231. Motoyama, M., Ejiri, M. & Iriyama, Y. In-Situ Electron Microscope Observations of Electrochemical Li Deposition/Dissolution with a LiPON Electrolyte. *Electrochemistry* **82,** 364–368. ISSN: 1344-3542 (2014).

232. Lu, Y., Zhao, C.-Z., Yuan, H., Cheng, X.-B., Huang, J.-Q. & Zhang, Q. Critical Current Density in Solid-State Lithium Metal Batteries: Mechanism, Influences, and Strategies. *Advanced Functional Materials,* 2009925. ISSN: 1616-301X (2021).

233. Kazyak, E., Wang, M. J., Lee, K., Yadavalli, S., Sanchez, A. J., Thouless, M., Sakamoto, J. & Dasgupta, N. P. Understanding the electrochemo-mechanics of Li plating in anode-free solid-state batteries with

operando 3D microscopy. *Matter* **5,** 3912–3934. ISSN: 2590-2385 (2022).

234. Ortmann, T., Fuchs, T., Eckhardt, J. K., Ding, Z., Ma, Q., Tietz, F., Kübel, C., Rohnke, M. & Janek, J. Deposition of Sodium Metal at the Copper-NaSICON Interface for Reservoir-Free Solid-State Sodium Batteries. *Advanced Energy Materials.* ISSN: 1614-6832 (2023).

235. Wang, H., Gao, H., Chen, X., Zhu, J., Li, W., Gong, Z., Li, Y., Wang, M.-S. & Yang, Y. Linking the Defects to the Formation and Growth of Li Dendrite in All-Solid-State Batteries. *Advanced Energy Materials* **11.** ISSN: 1614-6832 (2021).

APPENDIX – SUPPORTING INFORMATION

A.1   Benchmarking Li-Me-O interlayer

The fit errors for the charge transfer resistance R_{int1} were 25 %, 4 %, 10 %, and 7 % for the unmodified stack and stacks with Li-Nb-O, Li-Al-O, and Li-Ti-O interlayers, respectively. The standard deviations calculated for these fits of less than 10 % underscore the robustness of the analysis and highlight the differential effect of Li-Me-O interlayers on charge transport.

Table A.1. Fitted equivalent circuit parameters from the complex impedance spectra for samples with interlayer

Interlayer	$R_{contact}$ (Ω)	R_{pellet} (Ω)	CPE-T$_{pellet}$ (F)	CPE-P$_{pellet}$ (a.u.)	R_{int1} (Ω)	CPE-T$_{int1}$ (F)	CPE-P$_{int1}$ (a.u.)	R_{int2} (Ω)	CPE-T$_{int2}$ (F)	CPE-P$_{int2}$ (a.u.)	CPE-T$_{pol}$ (F)	CPE-P$_{pol}$ (a.u.)
w/o	370.2	124.3	1.77×10^{-9}	0.90	15799	3.40×10^{-8}	1.2	9.04×10^{5}	3.92×10^{-8}	0.87	3.40×10^{-8}	1.15
Li-Nb-O	372	226	4.69×10^{-10}	0.89	1093	1.83×10^{-8}	0.94	5.93×10^{5}	1.77×10^{-8}	0.94	1.64×10^{-8}	0.98
Li-Al-O	370.2	162.9	1.67×10^{-9}	0.88	4098	2.65×10^{-8}	0.98	1.13×10^{6}	3.88×10^{-8}	0.89	3.05×10^{-8}	0.91
Li-Ti-O	410.9	160.6	8.45×10^{-10}	0.93	4817	1.62×10^{-8}	1	332970	1.06×10^{-7}	0.83	6.06×10^{-8}	0.859

Figure A.1 shows the EIS data for an LLZO pellet in non-blocking electrode configuration (Li/LLZO/Li) and in blocking electrode configuration (Au/LLZO/Au). The non-blocking measurement was conducted at room temperature from 35 MHz down to 10 Hz. The extracted ionic conductivity was calculated from this data given by:

$$\sigma_{ion} = \frac{l}{R_{total}A},$$ (A.1)

where R_{total} is the total resistance (bulk + grain) of the electrolyte, l is the sample thickness, and A is the area.
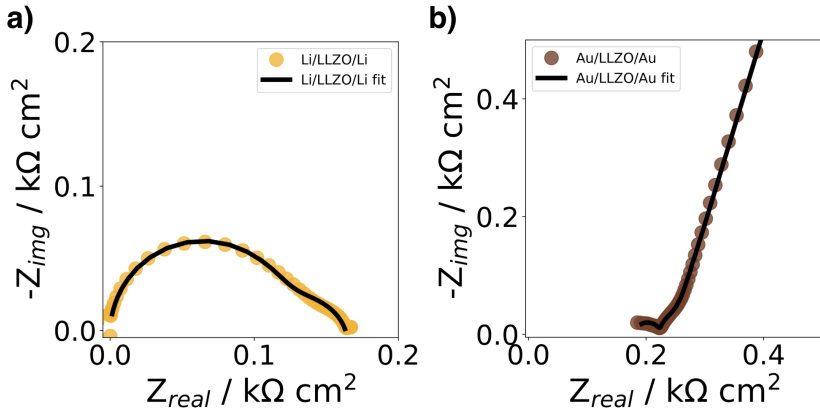

Figure A.1. Electrochemical impedance data of a) LLZO pellet in non-blocking electrode configuration (Li/LLZO/Li) , and b) LLZO pellet in blocking electrode configuration (Au/LLZO/Au).

Table A.2. Fitted equivalent circuit parameters from the complex impedance spectra for Li/LLZO/Li.

Parameter	Value
R_{bulk} / Ω	945.8
CPE-T_{bulk} / F	3.26×10^{-10}
CPE-P_{bulk} / a.u.	0.98371
R_{grain} / Ω	353.7
CPE-T_{grain} / F	1.75×10^{-7}
CPE-P_{grain} / a.u.	0.78594

Table A.3. Fitted equivalent circuit parameters from the complex impedance spectra for Au/LLZO/Au.

Parameter	Value
$R_{contact}$ / Ω	365.3
R_{pellet} / Ω	80.5
CPE-T_{pellet} / F	4.80×10^{-9}
R_{int1} / Ω	38.2
CPE-T_{int1} / F	5.30×10^{-8}
CPE-P_{int1} / a.u.	1.066
CPE-T_{pol} / F	9.91×10^{-7}
CPE-P_{pol} / a.u.	0.81184

Electrochemical impedance spectroscopy of full cells

Figure A.2 shows the impedance spectra for each cell in the pristine state at room temperature before the start of the CV measurement at 80 °C, and

after the CV scans at 80 °C. The impedance increases after the CV scan for the w/o, Li-Al-O and Li-Ti-O interlayers. For the Li-Nb-O cell, the impedance decreases with cycling, which is in contrast to the other cells. The decrease could be related to the voltage drop of the Li-Nb-O cell.
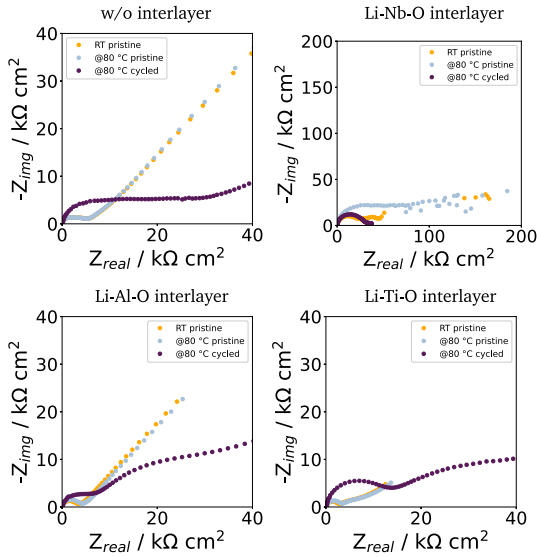

Figure A.2. Electrochemical impedance spectra of the cycled full cells for each interayer.

A.2   Voltage drop phenomenon

LinkedIn discussion on observed phaenomen

The compiled excerpts provided here are specifically relevant to the thesis. For a comprehensive overview of all comments and feedback of the post, please refer to the following link:

https://www.linkedin.com/posts/muellerandre96_ssb-lco-l lzo-activity-7055178457030225921-kBor?utm_source=share&utm _medium=member_desktop

Original Post

I've recently encountered a curious challenge while working on SSBs (LCO/LLZO), and I could really use your collective wisdom to figure it out. Here's the deal:

During the discharge cycles, I'm noticing a sudden voltage drop at around 3.9 V. What's strange is that there's no sign of it in the charge cycles. Even more intriguing, this phenomenon occurs over many cycles and remains quite consistent across multiple samples. After some digging, I've come across 2-3 similar cases in the literature, but with no explanations provided. So, I'm turning to my LinkedIn community to see if anyone has experienced this oddity before or has any insights into what could be causing it. If you've encountered something like this or have any ideas, please drop a comment or send me or my colleagues (Abdessalem Aribia, Moritz H. Futscher, Jędrzej Morzy, Joel Casella, Nicolas Osenciat) a message. I'm excited to hear your

thoughts and look forward to collaborating on solving this enigma together!

Let's join forces and crack this case!

Cheers, André

SSB #LCO #LLZO #voltagedrop #dischargecycle #batterytech #engineering #problemsolving #battchat #batterytechnology
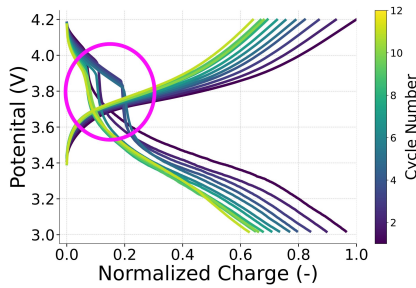

Figure A.3. Potential vs Normalized Charge with of LCO|LLZO|Li full cell.

Testing procedure EIS measurement

The entire process (charging, EIS during charging, discharging, EIS during discharging) is repeated three times.

A.3 Seed layers

AFM characterization

Table A.4. Summary of AFM-derived surface parameters for the investigated materials

		Au	C	Cu	Pt
Average value	nm	9,87	7,53	8,29	9,05
RMS roughness (Sq)	**nm**	**2,16**	**2,15**	**2,45**	**2,18**
RMS (grain-wise)	nm	2,16	2,15	2,45	2,18
Mean roughness (Sa)	nm	1,68	1,70	1,95	1,75
Skew (Ssk)		0,36	0,28	0,18	-23,31
Excess kurtosis		1,41	0,38	0,51	-0,18
Minimum	nm	0	0	0	0
Maximum	nm	21,1	16,6	21,54	15,68
Median	nm	9,84	7,47	8,29	9,06
Maximum peak height (Sp)	nm	11,23	9,07	13,25	6,63
Maximum pit depth (Sv)	nm	9,87	7,53	8,29	9,05
Maximum height (Sz)	**nm**	**21,11**	**16,60**	**21,54**	**15,68**
Projected area	**nm²**	**250000**	**250000**	**250000**	**250000**
Surface area	nm²	270238	262507	273273	266517
Surface slope (Sdq)		0,45	0,34	0,47	0,39
Volume	nm³	2468253	1881908	2071644	2262142
Variation	nm²	89922,3	72074,8	95299,1	81495,4
Inclination θ	deg	0,32	0,07	0,08	0,23
Inclination φ	deg	-170,59	-157,96	-148,21	-160,88
Scan line discrepancy		0,04	0,03	0,04	27,88

Cracking of bare copper CC

During the process of plating metal lithium onto the bare copper CC, it was observed that the copper layer began to exhibit cracks, as shown in Figure A.4. These cracks provided a pathway for the lithium metal not only to plate beneath the copper layer but also to diffuse into the soda-lime glass substrate, as depicted in Fig. 3a. The origin of these cracks can be traced back to the mechanical stress exerted on the copper CC films during the plating process.[41] This stress led to the deformation of the copper, resulting in the aforementioned cracks.

Detailed cycling procedure

The plating/stripping cycling protocol is outlined below and shown schematically in Figure A.5.

1. Initially, a constant current plating of 0.2 mAh cm^{-2} was carried out, utilizing a current density of 0.2 mA cm^{-2}.

2. Following this, the plated lithium was stripped using the same current density, continuing until a cut-off potential of 1.5 V was attained.

3. To ensure the complete removal of residual lithium, we employed constant voltage stripping.

4. Subsequently, we carried out repeated cycles of constant current plating and stripping:

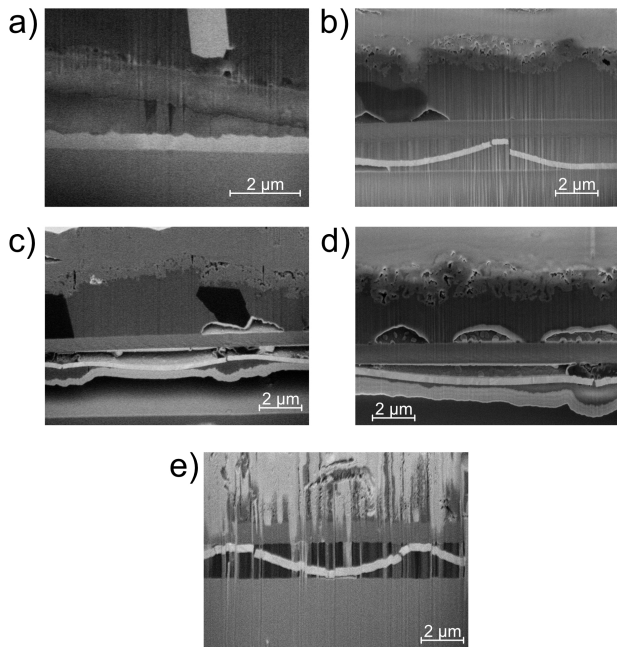- Each plating and stripping cycle was executed five times consecutively.

Figure A.4. Cross-sectional micrographs of the reference architecture Cu/LiPON/Li/Cu with 0.2 mAh cm^{-2} (1 µm) of lithium plated. a) shows non-uniform plating, while b)-e) show cracks in the copper CC.

- After completing these five cycles, the current density was incrementally increased by 0.2 mA cm^{-2}. This step-by-step increment was continued (i.e., 0.2, 0.4, 0.6, 0.8 mA cm^{-2} and so on) until a current density of 8 mA cm^{-2} was reached.

During the repeated cycles (as mentioned in step 4), we did not utilize constant voltage stripping, but the cut-off potential of 1.5 V was consistently maintained.
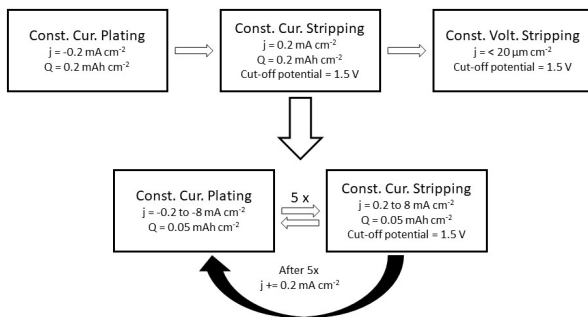
Figure A.5. Detailed cycling procedure for the plating/stripping experiment.

LIST OF PUBLICATIONS, PATENTS, CONFERENCES

Publications

- <u>André Müller</u>, Faruk Okur, Abdessalem Aribia, Nicolas Osenciat, Carlos AF Vaz, Valerie Siller, Mario El Kazzi, Evgeniia Gilshtein, Moritz H. Futscher, Kostiantyn V. Kravchyk, Maksym V. Kovalenko, Yaroslav E. Romanyuk. Benchmarking the performance of lithiated metal oxide interlayers at the $LiCoO_2$| LLZO interface. *Mater. Adv.* **4**, 2138–2146 (2023).
  This article is part of the themed collection: **Popular Advances**[1]

- <u>André Müller</u>, Luis Paravicini, Jędrzej Morzy, Maximilian Krause, Joel Casella, Nicolas Osenciat, Moritz H. Futscher, Yaroslav E. Romanyuk. Influence of Au, Pt, and C Seed Layers on Lithium Nucleation Dynamics For Anode-Free Solid-State Batteries. *ACS Appl. Mater. Interfaces* **16**, 695–703 (2024).

- Moritz H. Futscher, Thomas Amelal, Jordi Sastre, <u>André Müller</u>, Jyotish Patidar, Abdessalem Aribia, Kerstin Thorwarth, Sebastian Siol, Yaroslav E. Romanyuk. Influence of amorphous carbon interlayers on nucleation and early growth of lithium metal at the current collector-solid electrolyte interface. *J Mater Chem A* **10**, 15535–15542 (2022).

---

[1]This ongoing web collection brings together the most well received papers published in *Materials Advances* so far in 2023.

- Moritz H. Futscher, Luc Brinkman, <u>André Müller</u>, Joel Casella, Abdessalem Aribia, Yaroslav E. Romanyuk. Monolithically-stacked thin-film solid-state batteries. *Commun. Chem.* **6**, 110 (2023).

- Huagui Lai, Jincheng Luo, Yannick Zwirner, Selina Olthof, Alexander Wieczorek, Fangyuan Ye, Quentin Jeangros, Xinxing Yin, Fatima Akhundova, Tianshu Ma, Rui He, Radha K Kothandaraman, Xinyu Chin, Evgeniia Gilshtein, <u>André Müller</u>, Changlei Wang, Jarla Thiesbrummel, Sebastian Siol, José Márquez Prieto, Thomas Unold, Martin Stolterfoht, Cong Chen, Ayodhya N. Tiwari, Dewei Zhao, Fan Fu. High-Performance Flexible All-Perovskite Tandem Solar Cells with Reduced VOC-Deficit in Wide-Bandgap Subcell. *Adv. Energy Mater.* **12**, 2202438 (2022).

- Radha K. Kothandaraman, Severin Siegrist, Marion Dussouillez, Maximillian Krause, Huagui Lai, Johnpaul K. Pious, Shiro Nishiwaki, Evgeniia Gilshtein, <u>André Müller</u>, Antonio Cabas Vidani, Sandra Jenatsch, Beat Ruhstalle, Quentin Jeangros, Romain Carron, Ayodhya N. Tiwari, Fan Fu. Sputtered NiO interlayer for improved SAM coverage and pinhole free perovskite coating for scalable NIR-transparent perovskite and 4-terminal all-thin-film tandem modules. *Sol. RRL* **2400176**

Patents

- *Multi-cell monolithic thin-film battery and fabrication method thereof*, Europäische Patentanmeldung EP22181068.2.

Conferences

- 2022 Spring Meeting | EMRS, Oral presentation, *How ternary Li-oxide coatings affect the interfacial dynamics between $LiCoO_2$ (LCO) and $Li_7La_3Zr_2O_{12}$ (LLZO) in thin-film solid-state cells*

- 2022 Operando Battery Days, Grenoble, Poster presentation, *Shedding light on the influence of ternary Li-Me-oxide coatings on the interfacial dynamics of the LLZO/LCO interface*

- 2022 MAT-SUS nanoGe Fall Meeting, Barcelona, Poster presentation, *Understanding the influence of an artificial SEI at the LLZO/LCO electrolyte-cathode interface*

- 2022 Swiss Battery Days, Dübendorf, Poster presentation, *Understanding the influence of Li-Me-oxide coatings on the LLZO/LCO interface*

- 2023 Spring Meeting | EMRS, Poster presentation, *Understanding seed layers for lithium metal plating in all-solid-state batteries with 3D microscopy*,
  EMRS 2023 Spring „Best Poster Award - Symposium A: Solid state ionics"

- 2023 Swiss Battery Days, Villigen, Poster presentation, *Impact of Seed Layers at the Cu/LiPON Interface on Anode-Free Battery Performance*

- 2024 Gordon Research Conference Batteries, Ventura, Poster presentation, *Influence of Au, Pt, and C Seed Layers on Lithium Nucleation Dynamics For Anode-Free Solid-State Batteries*

XVIII

ACKNOWLEDGEMENTS

A Ph.D. journey is like a long, challenging bike ride with steep climbs, exhilarating descents, and unexpected twists and turns. It is a path of endurance and resilience. At some point, you wonder if it was a good decision to embark on the journey, but in the end, with mixed feelings, you are just excited to climb the next mountain.

I am deeply grateful to Dr. Yaroslav Romanyuk, who welcomed me into the battery group at Empa and accompanied me during my PhD years. His patience, invaluable support, and his appreciation of my technical skills have been a cornerstone of my journey. His mentorship has been instrumental in shaping me into the researcher I've become today.

Special thanks go to Professor Maksym Kovalenko for his scientific advice in challenging situations and for being my "Doktorvater". Thanks also to Professor Corsin Battaglia and Dr. Martin Finsterbusch for kindly accepting the role of co-examiners for this Thesis.

Thanks to the Lab207 team for the "Bier um Vier" (which was, in fact, always at 5 pm), the jokes, and the lighter moments that balanced our intense work. These breaks were a refreshing change from our sometimes monotonous academic routine. Above all, I would like to thank the battery team (Abi, Moritz, Jędrzej), who were always on hand when there were problems. I hope you haven't gone crazy with the endless discussions about the "Kink Enigma – The saga continues". Thanks also to Luis for always taking my mentoring with a sense of humor and for trying to get the best

out of his research despite countless difficulties.

A special shout-out goes to Nicolas, my "fellow doctoral student" and culinary guru - our moments together, from intensive research to chasing Michelin-starred restaurants, have added a unique flavor to this journey. Here's to more culinary adventures and discoveries!

Joel, my office "spouse" until our divorce, your humor, the shared responsibility for our "children" - the batteries - and the intense discussions made the time unforgettable. Stay just the way you are!

To my Züri crew (Aline, Celia & Maxime, Chiara, Dan, Franci, Frank, Jonny, Luca, Oskar, and Patty) and friends back home (Anna & JP, Jolle & Steffen, Maddi & Felix) – you are the psychiatrists who provide me with mental support, laughter, and memorable moments outside the lab. Our day trips, hikes, bike rides, drinks, dinners, and parties were the perfect balance for my research life.

Special thanks to my entire family. To my mom and dad, your belief in me was the base upon which I built myself. You've raised me with values that have shaped me into the man I am today - honest, faithful, and endlessly curious (the quintessence of a PhD). Thanks to your support, I was able to fully focus on my studies, whether I was in Spain, Switzerland, or anywhere else. Thank you for everything, for believing in me even when the road seemed daunting, and for raising me with the qualities that make a good human being.

To Maja, who was my rock. Your constant support, your open ear, your humorous nature, and your help were priceless. Your love and comfort have been a source of courage and support throughout this journey.

Last but not least, I would like to thank the entire AI team: ChatGPT 4, Grammarly, and DeepL. Thank you for helping me polish the linguistic and semantic aspects of my work.

And now, as I cross the finish line of this academic journey, I can't help but exclaim, "I did it!" Consider this my version of a "mic drop". With a heart full of gratitude and a mind looking forward to new challenges, I pedal on to the next adventure.

Here we go! 🚴🌐🎓

Curriculum Vitae

André Müller

Born in Fulda (Germany)

May 9th, 1996

Education

02/2021 - 04/2024	**ETH Zurich**, Zurich, Switzerland
	Doctoral studies at D-CHAB
10/2017 - 10/2019	**TU Braunschweig**, Braunschweig, Germany
	M. Sc. in Mechanical Engineering
04/2019 - 10/2019	**ETH Zurich**, Zurich, Switzerland
	Invited visiting student
09/2018 - 01/2019	**Universitat Politècnica de Catalunya**, Barcelona, Spain
	Exchange student in the ERASMUS+ framework
10/2014 - 09/2017	**DHBW Stuttgart**, Horb, Germany
	B.Eng. in Mechanical Engineering

Professional Experience

01/2021 - 04/2024	**Empa**, Dübendorf, Switzerland
	Doctoral researcher in the Laboratory for Thin Films and Photovoltaics
02/2020 - 12/2020	**Karlsruhe Institute of Technology IAM-ESS**, Karlsruhe, Germany, Research associate
10/2014 - 09/2017	**Strabag PFS GmbH**, Heusenstamm, Germany
	Dual student

"Success is not final, failure is not fatal: it is the courage to continue that counts."

– *Winston Churchill*